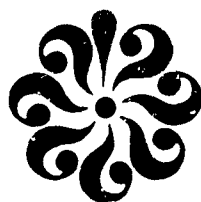


N O T I C E

THIS DOCUMENT HAS BEEN REPRODUCED FROM
MICROFICHE. ALTHOUGH IT IS RECOGNIZED THAT
CERTAIN PORTIONS ARE ILLEGIBLE, IT IS BEING RELEASED
IN THE INTEREST OF MAKING AVAILABLE AS MUCH
INFORMATION AS POSSIBLE



DEPARTMENT OF MECHANICAL ENGINEERING AND MECHANICS
SCHOOL OF ENGINEERING
OLD DOMINION UNIVERSITY
NORFOLK, VIRGINIA

SYNTHESIS OF A CONTROL MODEL FOR A LIQUID
NITROGEN COOLED, CLOSED CIRCUIT, CRYOGENIC
NITROGEN WIND TUNNEL AND ITS VALIDATION

(NASA-CR-162508) SYNTHESIS OF A CONTROL
MODEL FOR A LIQUID NITROGEN COOLED, CLOSED
CIRCUIT, CRYOGENIC NITROGEN WIND TUNNEL AND
ITS VALIDATION Progress Report, period
ending Sep. 1979 (Old Dominion Univ.,

N80-13058

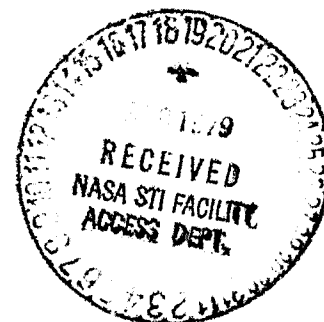
Unclas
G3/09 46261

By

S. Balakrishna

Principal Investigator: G.L. Goglia

Progress Report
For the period ending September 1979



Prepared for the
National Aeronautics and Space Administration
Langley Research Center
Hampton, Virginia

Under
Research Grant NSG 1503
Dr. Robert A. Kilgore, Technical Monitor
Subsonic Transonic Aerodynamics Division

November 1979

DEPARTMENT OF MECHANICAL ENGINEERING AND MECHANICS
SCHOOL OF ENGINEERING
OLD DOMINION UNIVERSITY
NORFOLK, VIRGINIA

SYNTHESIS OF A CONTROL MODEL FOR A LIQUID
NITROGEN COOLED, CLOSED CIRCUIT, CRYOGENIC,
NITROGEN WIND TUNNEL AND ITS VALIDATION

By

S. Balakrishna

Principal Investigator: G.L. Goglia

Progress Report
For the period ending September 1979

Prepared for the
National Aeronautics and Space Administration
Langley Research Center
Hampton, Virginia 23665

Under
Research Grant NSG 1503
Dr. Robert A. Kilgore, Technical Monitor
Subsonic Transonic Aerodynamics Division



Submitted by
Old Dominion University Research Foundation
P.O. Box 6369
Norfolk, Virginia 23508

November 1979

PREFACE

This report details the modeling phase of the project "Modeling and Control of Transonic Cryogenic Tunnel" sponsored by NASA/Langley Research Center under grant NSG 1503 which was performed during the period ending September 1979. The scope of this report is confined to model synthesis and its validation. Preliminary findings on this modeling activity were reported at the First International Symposium on Cryogenic Wind Tunnels which was held at University of Southampton, United Kingdom, in April 1979 (ref.2).

TABLE OF CONTENTS

| | <u>Page</u> |
|---|-------------|
| PREFACE | iii |
| INTRODUCTION | 1 |
| NOMENCLATURE | 3 |
| PRINCIPLE OF OPERATION OF SINGLE-RETURN, CLOSED CIRCUIT WIND TUNNELS | 6 |
| CLOSED CIRCUIT, LIQUID NITROGEN COOLED, GASEOUS NITROGEN OPERATED CRYOGENIC PRESSURE TUNNELS | 9 |
| TUNNEL AERODYNAMICS | 23 |
| FAN AND TUNNEL STEADY-STATE PERFORMANCE | 27 |
| TUNNEL TRANSIENT ANALYSIS | 33 |
| LUMPED MULTIVARIABLE MODEL OF A CRYOGENIC TUNNEL | 38 |
| DESCRIPTION OF THE 0.3-m TRANSONIC CRYOGENIC TUNNEL SYSTEMS | 40 |
| VALIDATION OF THE MODEL | 44 |
| SIMULATION OF THE 0.3-m TRANSONIC CRYOGENIC TUNNEL PROCESS | 45 |
| PERFORMANCE TESTS | 48 |
| QUASI-STEADY-STATE TESTS | 56 |
| CONCLUDING REMARKS | 59 |
| ACKNOWLEDGMENTS | 60 |
| APPENDIX | 61 |
| REFERENCES | 65 |

PRECEDING PAGE BLANK NOT REPRODUCED

THIS PAGE BLANK NOT REPRODUCED

LIST OF TABLES

| <u>Table</u> | | <u>Page</u> |
|--------------|--|-------------|
| 1 | 0.3-m TCT area distribution | 66 |
| 2 | 0.3-m TCT circuit loss pattern | 67 |
| 3 | Tunnel and simulator test conditions | 68 |

LIST OF FIGURES

| <u>Figure</u> | | |
|---------------|---|----|
| 1 | Density of nitrogen gas | 69 |
| 2 | Specific heat of nitrogen gas | 70 |
| 3 | Cooling capacity of liquid nitrogen | 71 |
| 4 | Cooling capacity of gaseous bleed | 72 |
| 5 | Energy state diagram | 73 |
| 6 | Thermodynamic model of a closed circuit cryogenic tunnel . . . | 74 |
| 7 | Tunnel state manipulation, equilibrium | 75 |
| 8 | Tunnel state manipulation, temperature rise at constant pressure | 76 |
| 9 | Tunnel state manipulation, temperature drop at constant pressure | 77 |
| 10 | Tunnel state manipulation, pressure rise at constant temperature | 78 |
| 11 | Tunnel state manipulation, pressure drop at constant temperature | 79 |
| 12 | Specific heat of aluminum alloy 6061-T6 | 80 |
| 13 | Enthalpy of aluminum alloy 6061-T6 | 81 |
| 14 | 0.3-m cryogenic tunnel energy state diagram, ideal internal insulation | 82 |

(continued)

LIST OF FIGURES - CONTINUED

| <u>Figure</u> | | <u>Page</u> |
|---------------|--|-------------|
| 15 | 0.3-m cryogenic tunnel energy state diagram, ideal external insulation | 83 |
| 16 | NTF energy state diagram, ideal internal insulation | 84 |
| 17 | NTF energy state diagram, ideal insulation with structural metal | 85 |
| 18 | Metal-to-gas heat transfer mechanism | 86 |
| 19 | Spatial profile of total temperature and pressure | 87 |
| 20 | Spatial profile of tunnel flow Mach number | 88 |
| 21 | Kinetic energy of moving gas, 0.3-m TCT | 89 |
| 22 | Tunnel circuit time, 0.3-m ICT | 90 |
| 23 | Spatial profile of local metal time constant | 91 |
| 24 | Average metal time constant | 92 |
| 25 | Average gas time constant | 93 |
| 26 | Lumped multivariable model of a cryogenic tunnel | 94 |
| 27 | Steady-state tunnel temperature gain for LN ₂ input | 95 |
| 28 | Transient tunnel temperature gain for LN ₂ input | 96 |
| 29 | Steady-state tunnel temperature gain for gas bleed | 97 |
| 30 | 0.3-m transonic cryogenic tunnel control configuration | 98 |
| 31 | Liquid nitrogen charge and gaseous bleed system schematic diagram | 99 |
| 32 | Operator display and control panel for hybrid simulation . . . | 100 |
| 33 | Hybrid simulation of a cryogenic tunnel | 101 |
| 34 | Analog scheme for temperature dynamics simulation | 102 |
| 35 | Analog scheme for pressure, fan and Mach number dynamics . . . | 103 |
| 36 | Simulator input function control | 104 |

(continued)

LIST OF FIGURES - CONTINUED

| <u>Figure</u> | | <u>Page</u> |
|---------------|--|-------------|
| 37 | Closed loop controllers | 105 |
| 38 | Tunnel and simulator responses; 0.3 M, 1.57 atm, 100 K | 106 |
| 39 | Tunnel and simulator responses; 0.6 M, 1.57 atm, 100 K | 107 |
| 40 | Tunnel and simulator responses; 0.9 M, 1.57 atm, 100 K | 108 |
| 41 | Tunnel and simulator responses; 0.3 M, 3 atm, 100 K | 109 |
| 42 | Tunnel and simulator responses; 0.6 M, 3 atm, 100 K | 110 |
| 43 | Tunnel and simulator responses; 0.95 M, 3.07 atm, 100 K | 111 |
| 44 | Tunnel and simulator responses; 0.3 M, 5.0 atm, 100 K | 112 |
| 45 | Tunnel and simulator responses; 0.6 M, 5.0 atm, 100 K | 113 |
| 46 | Tunnel and simulator responses; 0.9 M, 4.93 atm, 100 K | 114 |
| 47 | Tunnel and simulator responses; 0.3 M, 1.57 atm, 200 K | 115 |
| 48 | Tunnel and simulator responses; 0.6 M, 1.50 atm, 200 K | 116 |
| 49 | Tunnel and simulator responses; 0.9 M, 1.57 atm, 200 K | 117 |
| 50 | Tunnel and simulator responses; 0.3 M, 2.65 atm, 200 K | 118 |
| 51 | Tunnel and simulator responses; 0.6 M, 3 atm, 200 K | 119 |
| 52 | Tunnel and simulator responses; 0.9 M, 3 atm, 200 K | 120 |
| 53 | Tunnel and simulator responses; 0.3 M, 5 atm, 200 K | 121 |
| 54 | Tunnel and simulator responses; 0.6 M, 5 atm, 200 K | 122 |
| 55 | Tunnel and simulator responses; 0.9 M, 5 atm, 200 K | 123 |
| 56 | Tunnel and simulator responses; 0.3 M, 1.57 atm, 275 K | 124 |
| 57 | Tunnel and simulator responses; 0.6 M, 1.57 atm, 275 K | 125 |
| 58 | Tunnel and simulator responses; 0.75 M, 1.57 atm, 275 K | 126 |
| 59 | Tunnel and simulator responses; 0.3 M, 3 atm, 275 K | 127 |
| 60 | Tunnel and simulator responses; 0.6 M, 3 atm, 274 K | 128 |

(continued)

LIST OF FIGURES - CONCLUDED

| <u>Figure</u> | | <u>Page</u> |
|---------------|--|-------------|
| 61 | Tunnel and simulator responses; 0.75 M, 3 atm, 275 K | 129 |
| 62 | Tunnel and simulator responses; 0.3 M, 5 atm, 275 K | 130 |
| 63 | Tunnel and simulator responses; 0.6 M, 5 atm, 275 K | 131 |
| 64 | Tunnel and simulator responses; 0.8 M, 5 atm, 275 K | 132 |
| 65 | Cool down profile—tunnel and simulator | 133 |
| 66 | Warmup profile—tunnel and simulator | 134 |

SYNTHESIS OF A CONTROL MODEL FOR A LIQUID
NITROGEN COOLED, CLOSED CIRCUIT, CRYOGENIC, NITROGEN
WIND TUNNEL AND ITS VALIDATION

By

S. Balakrishna¹

INTRODUCTION

Demand for full-scale Reynolds number testing in modern transonic wind-tunnel test programs has resulted in considerable review of various methods of realizing such high Reynolds numbers without other serious penalties. The most promising amongst many techniques has been the concept of operating the test gas of a tunnel at cryogenic temperatures (ref. 1). Due to advances in the cryogenic engineering of economical production of cryogenics, materials compatible for cryogenic operation, and instrumentation, worldwide efforts at development of high Reynolds facilities using closed circuit cryogenic pressure tunnel development can be noted (ref. 2). All this activity was spearheaded by the proof of concept operation of the 0.3-m transonic cryogenic test facility at NASA/Langley Research Center (LaRC) (ref. 3). Operational experience with this facility has shown that cryogenic operation of its tunnel gases is a practical method for obtaining high Reynolds number flows without any dynamic pressure penalty and with savings in fan power (ref. 1).

Confidence in a wind tunnel is related to the flow quality and to the stability of the tunnel variables during the test period. Initial tunnel-running experience on the 0.3-m transonic cryogenic test facility has indicated that, though the tunnel process was basically stable, continuous drifting of the tunnel variables occurs because of mass and energy disturbances caused by unmatched control inputs. The instability is further compounded by a considerable degree of cross coupling between the tunnel variables and the controls. Manual regulation of the tunnel variables, though feasible, proves to be rather inefficient in terms of liquid nitrogen consumption. Further, transition of

¹ Research Assistant Professor, Old Dominion University Research Foundation, P.O. Box 6369, Norfolk, Virginia 23508. (On sabbatical leave from National Aeronautical Laboratory, Bangalore - 560 017, India.)

the tunnel conditions from one state to another has also proven to be uneconomical, due to long periods necessary to realize acceptable stability of tunnel conditions. Obviously closed-loop regulation and control of the cryogenic tunnel are the only solutions to the control problem.

For these reasons, studies have been undertaken to develop a control compatible mathematical model of a typical closed circuit cryogenic tunnel. No literature on such a model exists since the concept of cryogenic operation of tunnels is a recent one. In this document, the details of the efforts to synthesize a control-compatible multivariable model of a liquid nitrogen cooled, gaseous nitrogen operated, closed circuit, cryogenic pressure tunnel are presented. The synthesized model has been transformed into a real-time cryogenic tunnel simulator, and this model is validated by comparing the model responses to the actual tunnel responses of the 0.3-m transonic cryogenic tunnel, using the quasi-steady-state and the transient responses of the model and the tunnel. The global nature of the simple, explicit, lumped multivariable model of a closed circuit cryogenic tunnel is demonstrated.

NOMENCLATURE

| | |
|-----------------|--|
| A | area of cross section (m^2) |
| C | velocity of sound (m/sec) |
| C_v | specific heat at constant volume ($J/kg\ K$) |
| C_p | specific heat at constant pressure ($J/kg\ K$) |
| C_m | specific heat of tunnel metal ($J/kg\ K$) |
| C_d | valve coefficient |
| d | derivative operator |
| E | energy (J) |
| g | gravitational constant |
| H, h | enthalpy (J/kg) |
| i, I | integer indices |
| J | mechanical equivalent of heat |
| k, K | constants |
| l | length (m) |
| LN ₂ | liquid nitrogen |
| GN ₂ | gaseous nitrogen |
| \dot{m} | mass flow (kg/sec) |
| M | Mach number |
| N | fan speed |
| P | tunnel pressure (atm) |
| Q | heat (J) |
| q | dynamic pressure (kg/m^2) |
| r | fan pressure ratio |
| R | universal gas constant |
| Re | Reynolds number |

$R_{()}$ thermal resistance $[(J/m^2K \text{ sec})^{-1}]$
 S Laplace operator
 T gas temperature (K)
 t time, time constant (sec)
 U internal energy (J)
 u specific internal energy or velocity (J/kg or m/sec)
 V volume (m^3)
 W mass (kg)
 x distance (m)
 y, Y heat transfer coefficient ($J/m^2K \text{ sec}$)
 Z thermal impedance
 α cooling capacity of gas bleed (J/kg)
 β cooling capacity of liquid nitrogen (J/kg)
 γ ratio of specific heats
 ρ density of gas (kg/m^3)
 Δ increment
 Θ thermal mass (kg)
 μ viscosity
 τ transport delay (sec)
 η efficiency
 \cdot dot over a quantity refers to $\frac{d}{dt}$ of that quantity

Subscripts

F, f fan
 g gas
 k kinetic
 L liquid nitrogen

Subscripts (concluded)

| | |
|---|--------|
| m | metal |
| t | tunnel |
| s | static |

PRINCIPLE OF OPERATION OF SINGLE-RETURN, CLOSED CIRCUIT WIND TUNNELS

The wind tunnel is a device intended for studying the behavior of scaled models in fluid flow. A single-return, closed circuit wind tunnel is an efficient and aerodynamically designed endless duct made up of four straight segments which are joined by four corners. The wind-tunnel resident fluid, usually air, is moved axially by means of a fan to achieve desired flow velocities at a segment of the tunnel called the test section, wherein the test models are located. The geometrical design of a typical single-return, closed circuit tunnel is carried out such that the desired range of flow velocities is achieved at the test section with minimal fan power requirements and the flow possesses the desired flow qualities (ref. 4). Such tunnels typically consist of a settling chamber, a screen section with a heat exchanger to reduce turbulence and remove heat, a contraction which allows smooth and efficient acceleration of the test gas to desired flow velocities, a test section with a plenum to obtain adequate control of wall interference, a return leg diffuser, the first and the second leg corners with turning vanes, a fan and fan nacelle section with fan motor located either inside or outside the tunnel, a forward leg diffuser, and the third and fourth leg corners with turning vanes leading into the settling chamber. The closed circuit tunnels are either open to atmosphere or are totally enclosed, and these are called atmospheric or pressure tunnels respectively.

In order to accurately extrapolate the wind-tunnel generated, scale-model data to their full-scale counterparts, it is necessary to maintain flow similarity conditions in the wind-tunnel flow (ref. 4). The important flow similarity conditions for stationary test models are Reynolds number, the ratio of inertial and viscous forces, and Mach number, the ratio of inertial and elastic forces. Dynamic pressure is another flow parameter of model strength and structural significance. These flow parameters Re , M , q , are coupled non-linear functions of the measurable test section flow variables, viz static or stagnation pressure, static or stagnation temperature, and the mass flow rate. Under isentropic flow conditions, the tunnel test section flow parameters and the flow variables are related as

$$\left. \begin{aligned} M &= \frac{\dot{m}}{P_s A} \cdot \sqrt{\frac{RT_s}{\gamma}} \\ Re &= \frac{P_s M \ell}{\mu} \cdot \sqrt{\frac{\gamma}{RT_s}} \\ q &= \frac{1}{2} P_s M^2 \gamma \end{aligned} \right\} \quad (1)$$

$$\left. \begin{aligned} P_s &= \frac{P}{\left(1 + \frac{\gamma-1}{2} M^2\right)^{\frac{\gamma}{\gamma-1}}} \\ T_s &= \frac{T}{\left(1 + \frac{\gamma-1}{2} M^2\right)} \end{aligned} \right\} \quad (2)$$

The three flow parameters Re , M , and q are functions of three tunnel flow variables P_s , T_s and \dot{m} . To maintain flow similarity conditions in model study, a wind tunnel must allow independent control of the three flow parameters, which in turn can be achieved only if the three tunnel variables P_s , T_s and \dot{m} can be controlled independently.

Historically, in wind-tunnel testing, flow similarity has rarely been achieved in respect to Reynolds number. A study of the flow parameter controllability in various types of tunnels can now be reviewed. Ambient temperature atmospheric tunnels have an uncontrollable P and T which are always near atmospheric. In such tunnels only \dot{m} and hence Mach number can be independently controlled. Naturally, such tunnels are associated with uncontrollable Re and q . In the case of ambient temperature, closed circuit pressure tunnels, sometimes called the variable density tunnels, the test medium temperature is near atmospheric. However the tunnel pressure P can be controlled by adjusting the mass of fluid in the system, which is in addition to mass flow and Mach number control. Thus the variable density tunnels allow independent control of \dot{m} and P and hence M and q , but have a dependent Reynolds number. A high Re can be had, but is associated with considerable increase in flow dynamic pressure q and its accompanying structural problems. It is

in this context that the cryogenic operation of the test gas of a closed circuit pressure tunnel has become relevant. Such a tunnel allows independent control of all the variables \dot{m} , P and T and hence independent control of M , q and Re .

The test medium gas temperature control problem is general to all closed circuit, fan-driven tunnels, since operation of the fan to create desired flow is associated with fan compression and wall friction heating which tend to increase the gas temperature continuously. In the case of ambient temperature tunnels, this heat is removed by either a heat exchanger of the water tube type or by mixing atmospheric air. In either case the temperature control is crude and at best can provide cooling down to ambient. Further, the heat removal schemes are bulky and do not provide an adequate range of temperature control to influence Reynolds number.

CLOSED CIRCUIT, LIQUID NITROGEN COOLED, GASEOUS NITROGEN OPERATED, CRYOGENIC PRESSURE TUNNELS

The cryogenic wind-tunnel concept (ref. 1), though proposed many times, has become an engineering reality because of advances in cryogenic engineering and material. The concept allows efficient cooling down or regulation of the tunnel gas temperature at any fan power and involves injecting a liquified form of the test gas into the tunnel. Usually, gaseous nitrogen (GN_2) is the test medium and liquid nitrogen (LN_2) is the coolant. This cooling mechanism is fast and efficient, and cooling occurs down to near vapor phase temperature. In case of nitrogen, this temperature range is from about 78 K to 350 K at 1 atm. In contrast, the ambient temperature tunnels operate at a few degrees around the ambient 325 K. The wide range of temperature control in the cryogenic tunnel allows a large increase in Reynolds number without any dynamic pressure penalty. Since the viscosity of nitrogen gas varies as $T^{0.9}$, the Reynolds number increases as a function of $T^{-1.4}$. This is equivalent to a sixfold increase in Reynolds number when the gas is cooled from 300 K to 100 K.

Under steady-state operating conditions, the cooling induced by liquid nitrogen injection equals the fan power, thereby maintaining the temperature and keeping the tunnel pressure constant. Addition of liquid nitrogen into a tunnel not only results in cooling, but is also associated with tunnel gas mass increase. In order to maintain the tunnel resident gas mass, it is necessary to remove an equal amount of warm tunnel gases, which is associated with removal of enthalpy. This complex interaction of fan-induced heating, liquid nitrogen contributed mass increase and enthalpy decrease, and gaseous nitrogen bleed-induced mass decrease and enthalpy decrease is the cryogenic tunnel control problem. This can be analyzed by studying the thermodynamics of the cryogenic tunnel and its control inputs, which are intimately related to the thermophysical properties of liquid and gaseous nitrogen.

Thermophysical Properties of Nitrogen

The physical and thermal properties of element nitrogen have been a subject of exhaustive studies over wide ranges of temperature, pressure, and both liquid and gaseous phase. These properties have been well documented (ref. 5).

These studies indicate that under static conditions, nitrogen deviates considerably from perfect gas behavior in many respects. However, under isentropic expansion or contraction, nitrogen gas has been proven to behave near perfectly (ref. 6), both thermally and calorifically.

Real gas static properties, particularly density ρ and specific heat at constant volume C_v , are of special importance to control analysis. These real gas variables ρ and C_v are nonlinear functions of temperature and pressure, and the nonlinearities are dominant near the liquid-gas phase boundary. A simple function fit has been made for ρ and C_v using data from reference 5.

$$\left. \begin{array}{l} \rho = 12.18 \frac{P}{T} \left[1 + 250 \frac{P}{T^2} \right] \text{ mol/liter} \quad \text{Sat} \leq T \leq 400 \text{ K} \\ \text{or} \\ \rho = 338.9 \frac{P}{T} \left[1 + 250 \frac{P}{T^2} \right] \text{ kg/m}^3 \quad 1 \leq P \leq 8 \text{ atm} \end{array} \right\} \quad (3)$$

Similarly

$$\left. \begin{array}{l} C_v = 20.80 \left(1 + 250 \frac{P^{0.7}}{T^2} \right) \text{ J/mol K} \quad \text{Sat} \leq T \leq 400 \text{ K} \\ 1 \leq P \leq 8 \text{ atm} \end{array} \right\} \quad (4)$$

Figures 1 and 2 illustrate real gas properties ρ and C_v respectively, as functions of T and P . Nitrogen in its liquid form is associated with an enthalpy h_L which is a function of storage pressure and temperature. When a unit mass of liquid nitrogen stored at 1 atm pressure and saturation temperature is taken to a higher pressure P at temperature T , the heat absorbed by the unit mass of liquid nitrogen is the cooling capacity of liquid nitrogen. This enthalpy change has been estimated by Kilgore et al. (ref. 7) using the temperature entropy diagram. The route of this enthalpy change is a first isentropic compression of liquid nitrogen to the final pressure P , and subsequent warming and evaporation from colder saturation to higher T isobarically. From reference 7, we have

$$\begin{aligned} \beta &= \text{cooling capacity} \\ &= - \left[B_0 T + B_1 + \frac{B_2}{T} \right] \text{ kJ/kg} \end{aligned}$$

where

$$B_0 = 1.0379 - 3.917 \times 10^{-3} P$$

$$B_1 = 121.25 + 2.157 P$$

$$B_2 = 66.85 - 391.2 P$$

$$P = \text{Pressure in atm}$$

$$T = \text{Temperature in K}$$

This can be approximated to

$$\beta \approx h_L - C_p T \quad \text{kJ/kg} \quad (5)$$

Cooling capacity β is a negative number, where

$$h_L = \text{Latent heat of vaporization} - C_p T_{\text{sat}}$$

$$C_p = \text{Specific heat at constant pressure} \approx 1.04 \text{ kJ/kg}$$

A similar analysis of the cooling capacity of gaseous nitrogen taken from pressure P and temperature T to 1 atm and higher ambient temperature can be estimated on the temperature-entropy diagram. This can be approximated to

$$\alpha \approx (C_p - C_v) T \quad \text{kJ/kg} \quad (6)$$

where

$$\alpha = \text{cooling capacity of gaseous nitrogen}$$

$$C_p, C_v = \text{specific heats of nitrogen}$$

$$T = \text{Temperature, K}$$

the cooling capacity α is a positive number. Cooling capacities, β of liquid nitrogen and α of gas bleed are shown in figures 3 and 4, respectively, as functions of T and P .

Energy State Diagram

The internal energy associated with a finite volume of gas at a uniform pressure P , and temperature T is all energy associated with electrons at the molecular level and is a function of temperature as predicted by the third law of thermodynamics. At absolute zero, the internal energy and gas specific heat tend to zero. This can be expressed using the classical equation

$$U = \int_0^T C_V dT$$

where

$$C_V = \frac{dQ}{dt} \text{ at constant volume}$$

Density of nitrogen gas, as discussed previously, can be used to estimate mass of gas W_g , for a given volume of gas V at pressure P and temperature T

$$W_g = 338.90 \frac{P}{T} \left[1 + 250 \frac{P}{T^2} \right] \text{ kg/m}^3 \quad (7)$$

The internal energy associated with this volume of gas is

$$U = W_g \int_0^T C_V dT$$

Assuming $\int_0^T C_V dT = C_V T$ we have

$$U = 253.49 P \left(1 + 250 \frac{P}{T^2} \right) \left(1 + 250 \frac{P^{0.7}}{T^2} \right) \text{ kJ/m}^3 \quad (8)$$

A plot of gas internal energy U vs. its mass W_g is shown in figure 5, and it illustrates the mass-energy relationship for a unit volume of 1 m^3 . The loci of constant temperature on the diagram are the lines of slope $C_V T$ radiating from the origin, and these are the isothermal lines. The loci of constant pressure are lines which generally run parallel to x-axis and are the isobars. If the gas were truly perfect statically, the isobars would be truly

parallel to the mass axis. The real gas isobars have positive slope. The liquid-gas phase boundary runs near the 100 K isothermal line, and its true position has been ignored.

Consider a representative point A on the diagram, corresponding to a finite mass of gas at a known pressure and temperature in a 1-m³ volume. If any extra gas mass or energy is added to this system, the point A appropriately shifts graphically to account for the new mass and energy state. In the case of the cryogenic tunnel, the three control inputs and the thermal leakage, either from the ambient or the tunnel metal shell change the energy state of the system by moving it to new pressures and temperatures. Addition of liquid nitrogen constitutes a reduction of energy by negative enthalpy $m_L h_L$ and increase of mass by m_L . Bleeding of gas from the system similarly represents a reduction of energy by negative enthalpy $m_g h_g$, a mass decrease by m_g . Heat release from fan is a true energy input Q_F and wall released heat $-Q_t$. All these inputs can be represented as mass-energy vectors, and the sum of these control vectors provides the final state of system. This analysis can be carried out graphically by vector manipulation as shown in figure 5.

The same analysis can be carried out analytically, by studying the open thermodynamic system.

Thermodynamic Model of a Closed Circuit, Cryogenic Pressure Tunnel

The cryogenic pressure tunnel can be considered as a thermally autonomous pressure vessel of volume V containing nitrogen gas at a uniform pressure P and temperature T. The vessel is assumed to be ideally insulated, insulation being external to the metal wall. This vessel is assumed to be opened to a liquid nitrogen source and a gas bleed valve which allow transfer of mass and associated enthalpy. The vessel is also assumed to be opened to a fan shaft which creates necessary fluid flow and delivers the fan energy. Such a system is shown in schematic in figure 6. The liquid nitrogen flow rate is taken to be \dot{m}_L and occurs at a liquid pressure of P_L . The gas valve allows flow of \dot{m}_g out of the tunnel.

Assuming uniform mixing and ignoring work done, potential energy and kinetic energy and invoking first law of thermodynamics we have

$$h_L = U_L + P_L V_L$$

$$h_g = U_g + P_g V_g$$

then

$$-\dot{Q}_t + \dot{Q}_F + \dot{m}_L h_L = \dot{m}_g h_g + \frac{dU}{dt}$$

where

$-\dot{Q}_t$ = rate of heat release from tunnel wall to gas, J/sec

\dot{Q}_F = rate of heat release from fan, J/sec

U = internal energy = $W_g u$, J

u = specific internal energy

$$-\dot{Q}_t + \dot{Q}_F + \dot{m}_L h_L = \dot{m}_g h_g + \frac{d}{dt} (W_g u) = \dot{m}_g h_g + u \frac{dW_g}{dt} + W_g \frac{du}{dt}$$

$$-\dot{Q}_t + \dot{Q}_F + \dot{m}_L h_L - \dot{m}_g h_g = u(\dot{m}_L - \dot{m}_g) + W_g \frac{du}{dT} \cdot \frac{dT}{dt}$$

which can be simplified to

$$\dot{m}_L (h_L - u) - \dot{m}_g (h_g - u) - \dot{Q}_t + \dot{Q}_F = W_g C_v \frac{dT}{dt}$$

For a perfect gas we have $u = C_v T$ and $h_g = C_p T$; hence

$$\dot{m}_L (h_L - C_v T) - \dot{m}_g (C_p - C_v) T - \dot{Q}_t + \dot{Q}_F = W_g C_v \frac{dT}{dt} \quad (9)$$

The mass and energy crossing the boundary of the tunnel react with tunnel resident gas and change its state. This interaction, as detailed previously, of the control vectors can be shown on the energy state diagram as the charge, bleed and fan mass-energy rate vectors. In order to run the tunnel at a steady gas state, the Mach dependent \dot{Q}_F needs to be cancelled by sum of negative enthalpies

from charge and bleed, which in themselves should create no mass change. By manipulating the magnitudes of these control vectors, either a balance condition can be obtained or the tunnel state moved along any desired path.

The details of vector manipulation are shown in figures 7 to 11. Figure 7 shows conditions needed to maintain the steady tunnel state. The control input relations are

$$\dot{m}_L = \dot{m}_g \quad , \quad \dot{P} = \dot{T} = 0 \quad , \quad \dot{m}_L(h_L - C_p T) = -\dot{Q}_F$$

In figure 8, showing the technique of increasing gas temperature at constant pressure, the control input relationships are

$$\dot{m}_L = 0 \quad , \quad \dot{m}_g C_p T = \dot{Q}_F - \dot{Q}_t \quad , \quad \dot{P} = 0$$

and $\dot{T} = \frac{\dot{m}_g}{W_g} T$

In figure 9, the technique of gas temperature reduction at constant pressure is demonstrated.

$$\dot{m}_g = \dot{P} = 0 \quad , \quad \dot{m}_L h_L - \dot{Q}_F - \dot{Q}_t = 0 \quad , \quad \dot{T} = -\frac{\dot{m}_L}{W_g} T$$

In figures 8 and 9, \dot{Q}_t has been taken to be zero. In figure 10, the manipulation of control vectors to realize a pressure increase at constant temperature is illustrated. The control input relations are

$$\dot{T} = \dot{m}_g = \dot{Q}_t = 0 \quad , \quad \dot{m}_L(h_L - C_v T) + \dot{Q}_F = 0 \quad , \quad \dot{P} = \dot{m}_L C_v T$$

Similarly figure 11 illustrates control vector manipulation to achieve a pressure reduction at constant temperature.

$$\dot{T} = \dot{m}_L = \dot{Q}_t = 0 \quad , \quad \dot{m}_g(C_p - C_v)T - \dot{Q}_F = 0 \quad , \quad \dot{P} = -\dot{m}_g C_v T$$

Role of Metal-Stored Energy in Cryogenic Tunnels

Cryogenic tunnel engineering design demands insulation of the cold test gas from the ambient to prevent heat gains and the associated energy waste. Since these tunnels are required to operate over a considerable pressure range, typically one to eight atm, the insulator shell must possess the ability to withstand internal pressure without leakage of gases. Most insulators are poor structural material, and storage of high-pressure compressible fluids in the shell demands perfect safety and conformity to appropriate pressure vessel code. These requirements dictate use of cryogenic structural metals for the pressure vessel integrity. However the location of the insulation on this vessel can be either internal or external. When the insulation used is external to the tunnel shell, the structural metal is exposed to cold gases and thermally interacts with the gas by releasing heat. Alternately, the insulation can be internal to the tunnel, thereby isolating the metal from cold gases. In the latter case, the need for very good surface finish on the insulator to obviate problems of boundary layer growth demands use of thin, highly finished, metal panels. This is particularly true of the test section and contraction wherein good aerodynamic contouring is a must. Thus, engineering design of cryogenic tunnels dictates use of a considerable amount of metal within the insulation shell.

When the insulator behaves ideally, the cryogenic tunnel can be looked upon as an autonomous thermodynamic system. The metal-stored energy then becomes a part of the tunnel thermal inertia and tunnel internal energy. The tunnel energy is now in the form of gas molecule motion and lattice vibration of metal molecules. Any gross temperature difference between gas and metal results in heat transfer between the two at the gas-wall boundary, and under steady-state conditions the metal and gas are at the same temperature. The magnitude of metal-stored energy can be estimated by studying the enthalpy and specific heat of metals (ref. 8)

Specific Heat of Metals

The heat or energy stored in a molecule of solid metal at constant pressure is a function of temperature and can be defined as

$$U_{mp} = \int_0^T C_{mp} dt$$

where $C_{mp} = \frac{\Delta Q}{\Delta T}$ J/mol, and C_{mp} is the specific heat of metal at constant pressure P . The third law of thermodynamics predicts that for all phenomena which are in thermal equilibrium, the associated specific heat becomes zero at absolute zero temperature. For most engineering purposes, in the range of temperatures relevant to cryogenic tunnels, $C_{mp} = C_{mv} = C_m$. Specific heats for constant pressure and volume are almost equal.

It is well known that metals with a face-centered lattice crystal structure are the best-suited metals for cryogenic operation. Aluminum alloy 6061-T6 is a well-proven cryogenic aluminum alloy. In the rest of the analysis, use of this alloy has been assumed. Enthalpy of aluminum as a function of temperature has been well researched and reviewed by Corrucini (ref. 9). The specific heat data is also available in the same reference for the temperature range of cryogenic tunnel interest. Simple function fits have been made:

$$C_m = 5.5 T - 0.008 T^2 \quad \text{J/kg K} \quad T < 350 \text{ K} \quad (10)$$

$$H = \int_0^T C_m dT = 2.75 T^2 - 0.00266 T^3 \quad \text{J/kg} \quad T < 350 \text{ K} \quad (11)$$

These are illustrated in figures 12 and 13.

Cryogenic Tunnel Energy State Diagram

Consider a closed circuit, cryogenic pressure tunnel made of aluminum which is externally insulated. The total energy contained within this system is the sum of gas internal energy and metal enthalpy:

$$E = U + Q_t = W_g C_v T + W_t \int_0^T C_m dT \quad (12)$$

The energy state diagrams for two different, closed circuit, cryogenic, pressure tunnels, viz., the 0.3-m transonic cryogenic tunnel (TCT) and the proposed National Transonic Facility (NTF) are now analyzed. The 0.3-m TCT is an

externally insulated tunnel of total volume 14.1 m^3 and 3200 kg of aluminum alloy 6061-T6 within the insulation shell. The NTF has an estimated volume of 5600 m^3 , an internally insulated, stainless steel pressure vessel, and an estimated 280,000 kg of aluminum liners turning vanes, contraction cone, test section and other components. Two sets of the energy state diagram, for both the 0.3-m TCT and the NTF are presented in figures 14 to 17. Figures 14 and 15 correspond to U vs. W_g and E vs. W_g for the 0.3-m tunnel. Figures 16 and 17 are U vs. W_g and E vs. W_g for the NTF. In the case of the 0.3-m tunnel, the maximum U is only 3 percent of E and, in the case of NTF, U is about 12 percent of E . In either case, the dominant energy content of metal is evident; hence the metal thermal inertia is likely to be the dominant factor which affects the pressure and temperature dynamics of the tunnel. The figures 14 to 17 also illustrate the control vector directions. It can be noted that a simple charge input in figures 14 and 16 shifts the tunnel states such that both temperature and pressure drop. However, in figures 15 and 17, the same charge input generates a negative temperature shift and a positive pressure shift. Thus the energy state diagram U vs. W_g provides the instantaneous behavior of tunnel states and diagram E vs. W_g provides the final steady-state response. As will be demonstrated later, this shift of response from U initially to E provides the characteristic signature of cryogenic tunnels.

Metal to Gas Heat Transfer

The mechanism of heat transfer in a tunnel is a surface phenomenon and is a complex function of the metal and gas properties such as thermal conductivity, specific heat, gas density, and gas viscosity. Assuming the metal to gas heat transfer to be a forced convection heat transfer and ignoring other modes, the following dimensional analysis can be made:

| | | |
|----------------------|--------|--|
| Density of gas | ρ | ML^{-3} |
| Specific heat | C_p | $\text{L}^2\text{t}^{-2}\text{T}^{-1}$ |
| Thermal conductivity | $1/R$ | $\text{MLt}^{-3}\text{T}^{-1}$ |
| Viscosity | μ | $\text{ML}^{-1}\text{t}^{-1}$ |
| Velocity | u | Lt^{-1} |

| | | |
|-------------------------------|--------|-----------------|
| Distance | ℓ | L |
| Heat transfer coefficient y | | $Mt^{-3}T^{-1}$ |

The heat transfer coefficient y , is now assumed to be a function of the above listed variables. Matching the dimensions, we have

$$Mt^{-3}t^{-3} = \ell^{\frac{a}{}} \rho^{\frac{b}{}} C_p^{\frac{c}{}} \left(\frac{1}{R}\right)^{\frac{d}{}} \mu^{\frac{e}{}} u^{\frac{f}{}}$$

using arbitrary indicies \underline{a} , \underline{b} , \underline{c} , \underline{d} , \underline{e} , \underline{f} . For a dimensional match to be true

$$y = \frac{(\rho u)^{\underline{b}} (\mu C_p R)^{\underline{e}} (\ell C_p R)^{\underline{b}}}{DR}$$

For the following relations of the gas density, viscosity, and thermal conductivity

$$\rho \propto \frac{P}{T} \quad ; \quad \mu \propto m\sqrt{T} \quad ; \quad \mu \propto T^{0.9} \quad ; \quad R \propto T^{-0.98}$$

and Prandtl number $\mu C_p R$ is assumed to be constant. Then

$$y \propto \frac{P^{0.8} T^{-0.204} M^{0.8}}{D^{0.2}}$$

assuming b to be 0.8 (ref. 10). A numerical estimation of the heat transfer coefficient is now made based on constants validated by Bartz in reference 10. Using equation (6) of Bartz's work and using his notation,

$$h = \left[\frac{C}{D^{0.2}} \left(\frac{\mu^{0.2} C_p}{Pr^{0.5}} \right) \left(\frac{P_g}{C^*} \right)^{0.8} \right] \left(\frac{A^*}{A} \right)^{0.9} \sigma$$

$$\sigma = \frac{1}{\left[\frac{1}{2} \frac{T_w}{T_o} (1 + 0.2M^2) + \frac{1}{2} \right]^{0.632} (1 + 0.2M^2)^{0.167}}$$

using constants of $w = 0.6$ and $C = 0.026$. This heat transfer coefficient

has been validated at the nozzle of a rocket. A number of values of Y_g were estimated using $Pr = 0.73$ and $C^* = (T^{0.5}) \times 61.5$ for various pressures, temperatures and area ratios. This set of data was function fitted to obtain a simple heat transfer equation

$$Y_g = 71.27 p^{0.8} T^{-0.22} M(1 - 0.67M^{0.65}) J/m^2 K sec \quad (13)$$

This heat transfer coefficient Y_g provides the local forced convection heat transfer on a unit area of the tunnel metal-gas surface and is a function of local pressure, temperature, and Mach number. It can be used to establish the overall heat flow rate.

The heat flow from wall to gas is not only a function of surface convection based Y_g , but also a function of wall thermal conductivity, wall thermal capacity and wall leakage, if any. Consider a unit area of the tunnel wall thickness, starting from the gas boundary to the external tunnel face, as shown in figure 18. This cross section consists of the tunnel metal wall and the insulation. The heat flow occurring under transient conditions can be obtained from the simple electrical analog. Here $1/R_g$ corresponds to the heat transfer coefficient Y_g associated with the turbulent boundary layer of the tunnel flow discussed previously. Further, $1/R_m$ corresponds to the thermal conductivity of the metal wall thickness and C_m corresponds to thermal capacity of that layer. In view of the serial disposition of metal, R_m is divided into a number of layers each of resistance R , and C_m is divided into the same number of layers, each of capacity C . Similarly $1/R_I$ corresponds to thermal conductivity of the insulation, which tends to zero, and C_I is the enthalpy in the insulation. The heat-flow dynamics can be now analyzed by evaluating the thermal admittance of the ladder network.

$$Z = \text{Impedence} = R + \frac{1}{\frac{\frac{1}{\frac{R + 1}{\frac{CS + 1}{\frac{R + 1}{\frac{CS + 1}{R + \dots}}}}}}}$$

The above ladder network has been simplified for five serial elements of metal ignoring insulator:

$$Z = \frac{(RC)^5 S^5 + 9(RC)^4 S^4 + 28(RC)^3 S^3 + 35(RC)^2 S^2 + 15RC S + 1}{5CS \left[\frac{(RC)^4 S^4}{5} + \frac{8(RC)^3 S^3}{5} + \frac{21(RC)^2 S^2}{5} + \frac{20(RC)S}{5} + 1 \right]} \quad (14)$$

The time constant of one wall is $25RC = R_m C_m$. Using this a pole zero analysis of the impedance function was made. The poles are

$$\begin{aligned} \text{Poles} & \left\{ \begin{array}{l} (-0.8 + j 0.6) \frac{25}{R_m C_m}, \quad j = \sqrt{-1} \\ -\frac{59}{R_m C_m} \\ -\frac{100}{R_m C_m} \end{array} \right. \\ \text{Zeros} & \left\{ \begin{array}{l} -\frac{2}{R_m C_m} \\ -\frac{17.5}{R_m C_m} \\ -\frac{43}{R_m C_m} \\ -\frac{73}{R_m C_m} \\ -\frac{90}{R_m C_m} \end{array} \right. \end{aligned}$$

Ignoring the larger values of poles and zero, a simplification is made to estimate Z .

$$\frac{1}{Z} = \frac{C_m S \left(1 + \frac{R_m C_m S}{20} \right)}{\left(1 + \frac{R_m C_m S}{2} \right)} \quad (15)$$

Combining the wall and gas heat transfer equations, the heat flow in a unit area of tunnel wall on the basis of one-dimensional heat flow, and ideal insulation:

$$\dot{Q}_t = \frac{T}{Z} = \left[\frac{T C_m S \left(1 + \frac{R_m C_m S}{20} \right)}{1 + \left(\frac{R_m}{2} + R_g \right) C_m S} \right] \quad (16)$$

Equation (16) provides a simple, lumped model of heat flow in each unit area of the tunnel surface. The total heat flow can be estimated by integrating the individual heat flows. This is fairly complex in view of the fact that $Y_g = 1/R_g$, the dominant element of equation (16), varies throughout the tunnel surface as detailed by equation (13). It may be noted that lead time constant $\frac{R_m C_m}{20}$ is a small one compared to the denominator, and hence the heat flow is basically a first order dynamic.

The assumption of one-dimensional heat flow only across the wall, and not along the surface, can be justified on the basis that the 0.3-m TCT is flanged, and these flanges occur wherever area is changing rapidly. The flanges carry insulation in the form of a pressure seal gasket and hence prevent transverse heat flow. In any such flanged segment the tunnel states P , T and M are uniform to a first order approximation. All parameters of the heat flow equations, C_m , R_m and R_g , have been discussed previously.

TUNNEL AERODYNAMICS

The design of a closed circuit wind tunnel involves area-based, optimum circuit design of the endless tunnel duct so as to obtain desired flow velocity at the test section, assuring maximum flow quality at minimum power consumption. The steady-state flow through the tunnel duct assumes different velocities around the circuit as dictated by the compressibility flow laws of continuity, momentum, and energy. The power losses in a closed circuit wind tunnel are caused by wall friction and vary as a function of cube of the speed; hence it is desirable to maintain the lowest possible velocities in the return ducting other than in the test section, which results in large areas of cross section and optimum aerodynamic streamlining. Circuit losses occur in various segments of the tunnel duct, viz fan nacelle, the forward leg diffuser, the third and fourth corners with turning vanes, the settling chamber, the screen section, the contraction, the test section, return leg diffuser, and the first and the second corner. Estimation of the circuit loss has been well studied (refs. 4 and 11).

The cryogenic tunnel is an endless pressure duct of varying cross-sectional area which has, in addition to regular components of a closed circuit tunnel, a liquid nitrogen injection section and a gas bleed section, located downstream of the test section and in the settling chamber area, respectively. Fan operation sets the gas in motion, and this flow in the endless duct can be analyzed by forming the equations of flow continuity, momentum, and energy conservation for the tunnel. It is obvious that the flow process occurs both in space and time, and appropriate distributed system equations need to be set up and solved (ref. 12).

The cryogenic tunnel is assumed to be made up of a large number of small length cylindrical segments of uniform area. Consider an i th cylindrical segment which is bound by sections i and $i + 1$ which are $x(i)$ and $x(i + 1)$ distant along the centerline from the reference fan exit section. Let the cross-sectional area of the segment be $A(i)$, mass flows entering and exiting be $\dot{m}(i)$ and $\dot{m}(i + 1)$ respectively. The total pressures at entry and exit be $P(i)$ and $P(i + 1)$, $\rho(i)$ the average density, and $T_s(i)$ the average static temperature. The following discrete

equations set is valid for all $i = 1, \dots, I$ segments embracing the full length of the tunnel.

Continuity

The general equation of continuity for flow in a duct of cross sectional area A , fluid density ρ , mass flow rate \dot{m} over a length δx in a period δt , is

$$\frac{\partial}{\partial t} (A\rho) = - \frac{\partial}{\partial x} (\dot{m})$$

This equation of continuity for the i th segment of the tunnel can be written in the discrete form as

$$\frac{d}{dt} A(i) \rho(i) [x(i+1) - x(i)] = - \dot{m}(i+1) + \dot{m}(i)$$

or

$$\frac{d}{dt} W_g(i) = - \dot{m}(i+1) + \dot{m}(i) \quad (17)$$

In the cryogenic tunnel, under steady-state conditions, the mass flow difference $\dot{m}(i+1) - \dot{m}(i)$ is zero for all segments except for the ones having the liquid nitrogen flow inlet and gas bleed outlet. At these sections $\dot{m}(i+1) - \dot{m}(i) = \dot{m}_L$ or \dot{m}_g respectively. Further, it may be noted that at steady state:

$$\sum_{i=1}^I \dot{W}_g(i) = \sum_{i=1}^I \dot{m}(i+1) - \dot{m}(i) = \dot{m}_L - \dot{m}_g$$

Momentum Equation

The general equation of momentum associated with fluid flow in a cylindrical segment of cross-sectional area A with a mass flow \dot{m} , pressure P , velocity u over a length of δx over a period δt is

$$A \frac{\partial P}{\partial x} = \frac{\partial}{\partial t} \dot{m} - \frac{\partial}{\partial t} (\dot{m}u) - k_1 \dot{m}u$$

This represents the force balance across the segment in the form of inertial forces of flow, the momentum flux induced forces and the wall friction drop

across. Utilizing the identify $\dot{m}(i) = \rho(i) A(i) u(i)$, the discrete form of the momentum equation can be written as

$$A(i) \frac{P(i+1) - P(i)}{x(i+1) - x(i)} = - \ddot{m}(i) - \frac{k_1 \dot{m}^2(i)}{A(i) \rho(i)} - \frac{\dot{m}^2(i+1) - \dot{m}^2(i)}{A(i) \rho(i) [x(i+1) - x(i)]} \quad (18)$$

Further, under steady-state operation of the tunnel

$$\sum_{i=1}^I P(i+1) - P(i) = 0$$

for the full tunnel circuit. If the fan segment is excluded

$$\sum_{i=1} P(i+1) - P(i) = \text{tunnel circuit loss } \Delta P$$

Energy Equation

The general equations of energy associated with fluid flow in a cylindrical duct of length δx and cross-sectional area A , fluid density ρ , static temperature T_s , mass flow m , velocity u , and a metal wall that releases heat at rate of $-\dot{Q}_t$ can be written in a pair of equations

$$E = \left(A \rho C_v T_s + \frac{A \rho u^2}{Jg} \right) \delta x \quad (19)$$

$$\frac{\partial E}{\partial t} = - \frac{\partial}{\partial x} (C_p \dot{m} T_s) - \frac{\partial}{\partial t} Q_t - \frac{1}{2Jg} \frac{\partial}{\partial x} \left(\frac{\dot{m}^3}{\rho^2} \right) \quad (20)$$

These equations correspond to the fact that total energy in the segment is the sum of internal energy and flow kinetic energy, and the energy rate equation includes temperature-dependent adiabatic heat rate, flow velocity contributions, and metal wall released heat. In the case of cryogenic tunnels, energy rate inputs also occur at the liquid injection section, the fan section and the gas bleed section. The discrete forms of energy equation can now be written as

$$\begin{aligned}
& \frac{d}{dt} \left\{ A(i) \rho(i) C_v T_s(i) [x(i+1) - x(i)] + \frac{\dot{m}^2(i)}{J_g A(i) \rho(i)} [x(i+1) - x(i)] \right\} \\
& = [T_m(i) - T_s(i)] y(i) [x(i+1) - x(i)] \sqrt{4\pi A(i)} \\
& + \frac{C_p}{x(i+1) - x(i)} [\dot{m}(i+1) - \dot{m}(i)] T_s(i) + \dots \quad (21)
\end{aligned}$$

In the segments in which liquid injection, fan operation and gas bleed occur, additional energy rate terms of $\dot{m}_L h_L$, \dot{Q}_F and $-\dot{m}_g C_p T$ are to be appropriately added.

FAN AND TUNNEL STEADY-STATE PERFORMANCE

The steady state performance of a closed circuit tunnel and fan can now be analyzed (ref. 1), and values of mass flow, pressure ratio, fan temperature rise, and fan power at steady state determined.

Mass Flow

The test section mass flow in any tunnel is related to the settling chamber total pressure, total temperature and the flow velocity. Considering isentropic flow through contraction we have

$$\begin{aligned}
 \dot{m} &= \rho u A = P_s A M \sqrt{\frac{\gamma T_s}{R \text{ mole}}} \\
 &= 6965 \frac{P}{\sqrt{T}} A M \left[\frac{1}{1 + \frac{\gamma-1}{2} M^2} \right]^{-\frac{\gamma+1}{2(\gamma-1)}} \text{ kg/sec} \\
 &= 6965 \frac{P}{\sqrt{T}} A M \left[\frac{1}{1 + 0.2 M^2} \right]^{-3} \text{ kg/sec} \quad , \text{ for } \gamma = 1.4
 \end{aligned} \tag{22}$$

Pressure Ratio Across Fan

In any closed circuit tunnel, the steady-state flow fan pressure ratio is a function of the pressure losses occurring in various segments of the tunnel and can be expressed in a simple form, normalized to test section Mach number as

$$r = 1 + b M^2 \tag{23}$$

where b is the integrated loss factor coefficient, and is likely to be a function of flow Reynolds number

$$b = F(Re)$$

with this knowledge of pressure ratio, the fan temperature rise can be estimated.

Fan Temperature Rise

The total pressure rise ΔP and the temperature rise ΔT are related under isentropic flow conditions as

$$1 + \frac{\Delta P}{P_{\text{inlet}}} = r = \left(1 + \frac{\Delta T}{T_{\text{inlet}}}\right)^{\frac{\gamma}{\gamma-1}}$$

Since the fan inlet temperature at steady state is $T - \Delta T$, we have

$$r = \left(\frac{T}{T - \Delta T}\right)^{\frac{\gamma-1}{\gamma}}$$

Simplifying

$$\Delta T = \frac{T}{\eta} \left[\frac{\frac{\gamma-1}{r^\gamma} - 1}{\frac{\gamma-1}{r^\gamma}} \right] \quad (24)$$

where η is the fan efficiency factor.

Fan Power

The fan power can now be estimated as the heat released by

$$\dot{Q}_F = C_p \dot{m}_{\text{fan inlet}} \Delta T$$

Though mass flow at fan inlet is $\dot{m} + \dot{m}_L$, ignoring the contribution of this small flow \dot{m}_L ,

$$\dot{Q}_F = \frac{K_F P M^3 \sqrt{T}}{(1 + 0.2M^2)^3} \quad (25)$$

where

$$K_F = \frac{6965}{\eta} AC_p b \left(\frac{\gamma-1}{\gamma}\right)$$

Spatial Profile of Tunnel Variables

When the cryogenic tunnel is in equilibrium, the steady-state solutions to the energy, continuity and momentum flow equations provide the spatial profile of the tunnel variables. Since equations (17) and (20) are complex, the computations are simplified by describing the tunnel by 16 sections binding 15 segments as detailed in table 2.

Mass flow: when the tunnel is in equilibrium $\frac{dW_g}{dt} = 0$ and $\dot{m}_L = \dot{m}_g$ then

$$\left. \begin{aligned} \dot{m}(9) &= \text{test section mass flow} \\ &= 6965 \frac{P}{\sqrt{T}} A(9) M (1 + 0.2M^2)^{-3} \\ \dot{m}(i) &= \dot{m}(9) \quad \text{for } 6 \leq i \leq 10 \\ \dot{m}(i) &= \dot{m}(9) + \dot{m}_L \quad \text{for } 1 \leq i \leq 5 \\ &\quad 11 \leq i \leq 15 \end{aligned} \right\} \quad (26a)$$

Further, from the power point of view

$$\dot{m}_L = \dot{m}_g = \frac{\dot{Q}_F}{\beta} = \frac{K_F P \sqrt{T} M^3}{\beta (1 + 0.2M^2)} \quad (26b)$$

Tunnel Total Pressure

The steady-state solution to the momentum equation is

$$\sum_{i=1}^{15} (P(i+1) - P(i)) = P(15) (r - 1)$$

The pressure profile can now be found to be

$$\begin{aligned} P(9) &= p \\ P(i) &= P(9) - \sum_9^i \Delta P(i) \end{aligned}$$

The pressure drop ΔP in each segment is

$$\Delta P(i) = \frac{k_1 \dot{m}^2(i)}{A^2(i) \rho(i)} = \Delta k(i) M^2(i) P_s(i) \quad (27)$$

Values of estimated $\sum \frac{\Delta P}{P_s}$ for the 0.3-m transonic cryogenic tunnel are shown in table 2. These values were obtained by distributing known tunnel circuit loss, based on simple analysis of geometrical and other loss effects.

Total Temperature Profile

When the tunnel is in equilibrium, the energy rate of the system is zero. Based on this the tunnel total temperature profile can be determined based on equation (39) to be discussed later:

$$\begin{aligned} T(9) &= T & i &= 6 \text{ to } 10 \\ T(i) &= T - \Delta T \frac{\beta + \alpha}{\theta} & i &= 11 \text{ to } 15 \\ T(i) &= T - \Delta T \frac{\alpha}{\theta} & i &= 1 \text{ to } 5 \end{aligned} \quad (28)$$

Mach Number Profile

The local flow Mach number $M(i)$ at any segment i can be obtained by solving the sixth order polynomial in $M(i)$ and seeking the solution between $0 < M(i) < 1$.

$$[1 + 0.2M^2(i)]^3 - 6965 \frac{P(i) M(i) A(i)}{\dot{m}(i) \sqrt{T(i)}} = 0 \quad (29)$$

All quantities except $M(i)$ are known in equation (29).

Kinetic Energy

An estimation of the flow kinetic energy associated with the gas flow through the tunnel can be made as follows:

$$E_k(i) = \frac{W_g(i) M^2(i)}{2Jg} \cdot \frac{\gamma R T_s(i)}{\text{mole}}$$

$$E_k(i) = \frac{338.9 P(i) V(i) M^2(i)}{\text{mole} \cdot 2Jg} \gamma R \left[1 + 250 \frac{P}{T^2} \right] \quad (30)$$

Computer estimations of the various steady-state profiles and kinetic energy were made for various test section conditions of P , T and M , and these values are presented in the following text.

Mass of the Gas in the Tunnel

When the tunnel gas is stationary, the mass of gas in the tunnel is

$$W_g = 338.9 \frac{PV}{T} \left[1 + 250 \frac{P}{T^2} \right] \quad (31)$$

As the fan is accelerated, the density of the gas around the tunnel changes and density in the test section drops. As a result the total pressure goes up. Alternately, at a given pressure P , the mass of gas comes down. This change of mass has been function fitted as

$$W_g = 338.9 \frac{PV}{T} \left(1 + 250 \frac{P}{T^2} \right) \left(1 - 0.033 M^{1.5} \right) \quad (32)$$

Typical plots of spatial profiles of $P(i)$ and $P_s(i)$, $T(i)$ and $M(i)$ for $T = 100$ K and $P = 2$ atm at test section Mach numbers of 0.3 and 1.0 are shown in figures 19 and 20. These profiles are plotted against tunnel center-line in the developed form. The strong correlation of cross-sectional area on the tunnel variables at different Mach numbers is evident. It can be further inferred that total and static pressures are grossly different only in the test section. Further, the flow velocity is very low in most of the circuit except at the test section.

In figure 21, a plot of tunnel kinetic energy as a function of test section Mach number is presented. The kinetic energy is almost independent of the tunnel temperature and is of the type PM^2 as detailed in equation (30). At a tunnel pressure of 6 atm, the kinetic energy is maximum at about 190 kJ at $M = 1$. Comparison of the 0.3-m cryogenic tunnel kinetic energy E_k with gas internal energy U shows that E_k is only about 0.75 percent of U even at $M = 1$. Obviously, E_k is an insignificant fraction of metal enthalpy.

Tunnel Circuit Time

The tunnel resident gas is moved around the duct in a finite time, which is the tunnel circuit time. Hence

$$W_g = t_c \cdot \dot{m}$$

Ignoring the contributions of \dot{m}_L entering the tunnel at section 11 and exiting at section 6, we have

$$t_c = \frac{W_g}{\dot{m}(9)} = \frac{0.0045 V}{A(9) M \sqrt{T}} \left[1 + 250 \frac{P}{T^2} \right] \left[1 + 0.2 M^2 \right]^3 \left[1 - 0.033 M^{1.5} \right] \quad (33)$$

An estimate of t_c was made for various P , T and M and is presented in figure 22. The tunnel circuit time is largest at low Mach number and low temperatures and smallest at Mach 1 and ambient temperature.

Tunnel Fan Performance

The fan performance can be expressed in terms of either the fan map or in terms of speed and pressure ratio data for the tunnel. Since the 0.3-m tunnel has been operational for a considerable time, a large quantity of fan speed, Mach number, and pressure ratio data is available. This steady-state data has been analyzed and function fitted to obtain following explicit tunnel-fan interface performance.

The fan speed and the test section Mach number are related by this empirical expression, and the fit is good to ± 10 rpm for any given Mach number:

$$N = 597 M \sqrt{T} (1 - 0.3M) P^{-0.035} \quad (34)$$

Secondly the fan pressure ratio and the test section Mach number are empirically related as a function of flow Reynolds number,

$$r = 1 + M^2 \left[0.197 \left(1 - \frac{7PM}{T} \right) \right] \quad (35)$$

The Reynolds number effects on r has been expressed in a very simple functional relationship.

TUNNEL TRANSIENT ANALYSIS

The true transient response of the tunnel is the dynamical solution to the flow equations of continuity, energy and momentum both in space and time. In this analysis, a lumped model approach has been used in solving the flow equations by treating the tunnel as a single lumped volume. This can be justified by observing that flow kinetic energy which creates spatial variation of tunnel energy states is a very small fraction of the total internal energy and the metal-stored enthalpy. These latter dominant energy terms dictate the tunnel temperature and pressure dynamics. However Mach number is a spatial function of geometry. Hence the approach used in the transient analysis has been to determine the average transient behavior at a low velocity segment on a lumped volume basis and superimpose the steady-state values of the tunnel spatial profile on this average state. The inaccuracies caused by the lumped approach are suppression of acoustic adiabatic waves and some circuit modes if the mixing is not good.

Tunnel Dynamic Model

Consider the lumped energy equation of a cryogenic tunnel system, from equations (19, 20)

$$\frac{d}{dt} [W_g C_v T_s + k_3 P M^2] = \dot{Q}_F + \dot{m}_L h_L - \dot{m}_g C_p T - \int_{\text{Surface}} \dot{Q}_t$$

Ignoring the rate contribution of kinetic energy and taking C_v to be a constant

$$W_g C_v \frac{dT}{dt} + C_v T \frac{dW_g}{dt} = \dot{Q}_F + \dot{m}_L h_L - \dot{m}_g C_p T - \int_{\text{Surface}} \dot{Q}_t$$

$$\frac{dT}{dt} = \frac{1}{W_g C_v} \left[\dot{m}_L (h_L - C_v T) - \dot{m}_g (C_p - C_v) T + \dot{Q}_F - \int_{\text{Surface}} \dot{Q}_t \right]$$

In order to allow evaporation and transit time effects that are associated with each control input, three transport lag terms can be added. Since the tunnel conditions are measured at the settling chamber, transit times from the control input to the settling chamber are considered. However, the gas vent is located at the settling chamber and hence can be ignored; then

$$\frac{dT}{dt} = \frac{1}{W_g C_v} \left[\dot{m}_L (h_L - C_v T) e^{-\tau_L S} - \dot{m}_g (C_p - C_v) T + \dot{Q}_F e^{-\tau_F S} - \int_{\text{Surface}} \dot{Q}_t \right] \quad (36)$$

The heat transfer from the metal wall occurs throughout the internal surface as was detailed in a previous section. This can be expressed as

$$\int_{\text{Surface}} \dot{Q}_t = \sum_{i=1}^{15} \frac{W_t(i) C_m TS}{1 + t_m(i) S}$$

where $W_t(i)$ is the weight of metal in each segment of the tunnel and $t_m(i)$ is the local metal time constant. Further,

$$t_m(i) = \frac{W_t(i) C_m}{[x(i+1) - x(i)] \sqrt{4\pi A(i)}} \left[\frac{1}{Y_g(i)} + \frac{1}{2Y_m(i)} \right] \quad (37)$$

where $Y_g(i) = \frac{1}{R_g(i)}$ = gas to wall heat transfer coefficient

$$= 71.27 P(i)^{0.8} T(i)^{-0.22} M(i) [1 - 0.67 M(i)^{0.65}]$$

$$Y_m(i) = \frac{1}{R_m(i)} = (200 + 1.41 T) \text{ J/m}^2 \text{ K sec (ref. 13)}$$

A computer evaluation of $t_m(i)$ as a function of tunnel space has been made, and figure 23 provides the local metal time constant profile which indicates rapid response at the high-speed section and slow response at the settling chamber. Further, to lump the heat transfer effects, the following simplification is made:

$$\int \dot{Q}_t = \frac{W_t C_m TS}{1 + t_m S}$$

where t_m is an average metal time constant for the tunnel

$$t_m = \frac{W_t C_m}{\sum_{i=1}^{15} \left\{ [x(i+1) - x(i)] \sqrt{4\pi A(i)} \left[\frac{2Y_g(i) Y_m(i)}{2Y_g(i) + Y_m(i)} \right] \right\}} \quad (38)$$

The gross metal time constant has been estimated for the whole tunnel envelope as a function of P , T and M and is shown in figure 24. Large metal time constants occur at low Mach numbers such as $M = 0.2$, $P = 1.5$ atm and $T = 300$ K. The lowest time constant occurs at $M = 1$, $T = 100$ K and $P = 5$ atm. Further, a simple function fit was made for use in simulation studies as

$$t_m = 0.28 T^{1.2} P^{-0.7} M^{-0.7} \text{ sec}$$

The tunnel temperature dynamics can now be expressed as

$$\frac{dT}{dt} \left[W_g C_v + \frac{W_t C_m}{1 + t_m S} \right] = \dot{m}_L (h_L - C_v T) e^{-\tau_L S} - \dot{m}_g (C_p - C_v) T + \dot{Q}_F e^{-\tau_F S}$$

using the identities by definition

$$\alpha \triangleq (C_p - C_v) T$$

$$\beta \triangleq (h_L - C_p T)$$

$$\theta \triangleq W_g C_v + W_t C_m$$

$$t_g \triangleq \frac{W_g C_v}{\theta} t_m$$

$$\frac{dT}{dt} \left[\frac{1 + t_g S}{1 + t_m S} \right] = \dot{m}_L \left(\frac{\beta + \alpha}{\theta} \right) e^{-\tau_L S} - \dot{m}_g \frac{\alpha}{\theta} + \frac{\dot{Q}_F}{\theta} e^{-\tau_F S} \quad (39)$$

The equivalent tunnel gas time constant t_g is a function of the relative gas thermal capacity to total thermal capacity and the metal time constant. This time constant t_g has been estimated as a function of P , T and M and is shown in figure 25. When $\frac{dT}{dt} = 0$, equation (39) provides the solution to spatial distribution of total temperature discussed in equation (28). The total pressure dynamics of the cryogenic wind tunnel is contributed to by momentum equation and perfect gas properties

$$P = k_2 W_g T$$

$$\frac{dP}{dt} = k_2 W_g \frac{dT}{dt} + k_2 T \frac{dW_g}{dT} + \text{momentum effects}$$

A quasi-steady-state approach may now be taken, and the momentum effects are attributed to fan pressure ratio changes. In the fan

$$\frac{P(1)}{P(15)} = r = 1 + bM^2$$

Assuming b to be a constant, Mach number changes and pressure ratio changes can be related as

$$\frac{dP(1)}{dt} = \frac{dP(15)}{dt} (1 + bM^2) + P(15) \left[2b M \frac{dM}{dt} \right]$$

Thus the total pressure dynamics is related to Mach number dynamics through a function of the type

$$\frac{dP}{dt} = K_k + bMP \frac{dM}{dt}$$

For the cryogenic tunnel, the pressure dynamics can be expressed as

$$\frac{dP}{dt} = \frac{P}{T} \frac{dT}{dt} + \frac{P}{W_g} (\dot{m}_L - \dot{m}_g) + K_k + bMP \frac{dM}{dt} \quad (40)$$

No transport delay terms are manifest in the pressure dynamics since pressure space dynamics occur at acoustic velocity. This transit time around the circuit is less than 50 msec at its largest. The Mach number at the test section can be directly related to fan rpm to provide the quasi-steady-state dynamics of Mach number

$$M = \frac{N}{597 \sqrt{T} (1 - 0.3M) P^{-0.035}}$$

Because of the plenum volume, the Mach number dynamics is affected, and this change is of a first order type because of net flow into or out of the plenum. Then

$$M = \frac{e^{-\tau_a S}}{k_m \sqrt{T} (1 + t_p S)} N \quad (41)$$

where

$e^{-\tau_a S}$ = acoustic time delay

t_p = plenum time constant

k_m = $597 (1 - 0.3M) P^{-0.035}$

LUMPED MULTIVARIABLE MODEL OF A CRYOGENIC TUNNEL

The three equations (39), (40) and (41) derived previously provide explicit identities of average total pressure gradient \dot{P} , total temperature gradient \dot{T} and the test section Mach number as a function of the three control inputs, the liquid nitrogen mass flow, the gas bleed mass flow and fan speed. The three equations represent the nine elements of a transfer function matrix model of a cryogenic tunnel which is shown in figure 26.

This matrix model has linear dynamical terms with nonlinear coefficients. The parameters of this model are the tunnel geometrical constants, the thermophysical parameters of liquid and gaseous nitrogen, and the surface heat transfer parameters. Since the off-diagonal elements of the model are fairly dominant, the process is obviously strongly coupled.

The nine input-output type gain elements of the multivariable lumped model of the cryogenic tunnel describe the steady-state process change for a unit incremental input of the control. The three diagonal elements represent the direct gain terms from liquid nitrogen to temperature, fan rpm to Mach number, and gas bleed to pressure. The other off-diagonal terms are the interaction terms. The following study of the nine gain terms provides a knowledge of the dominance of inputs on the process and its coupling.

In figure 27, a plot of temperature gain term $(\beta + \alpha)/\theta$ for a unit liquid nitrogen input is shown. Typically 1 kg of liquid nitrogen induces a steady-state change of gas temperature of -0.13 K/kg. However, under transient conditions an approximate gain term of type $(\beta + \alpha)/W_g C_v$ describes the amplitude of response, which is shown in figure 28. The plot suggests a high temperature gain of -30 K/kg at $P = 1$ atm and $T = 300$ K. The gain reduces to -2 K/kg at $P = 5$ atm and $T = 100$ K.

The term α/θ represents the temperature gain of the tunnel due to unit bleed of tunnel resident gas, and is shown in figure 29. This sensitivity is a small fraction of liquid nitrogen response and suggests a weaker coupling from bleed to temperature. The transient response is relatively higher than the steady state, but still weaker.

The temperature gain term for fan speed is $\dot{Q}_F \Delta N / N \theta$ and is a very strong gain element. Obviously the gain is high at high power, and the gain term can be approximated to $P \sqrt{T} M^{1.2} \frac{\Delta N}{N \theta}$. At $P = 5$ atm, $T = 275$ K and $M = 1$ the gain is largest.

The tunnel test section Mach number is directly related to fan speed and the coupling terms from liquid nitrogen flow or gas flow are zero. However the cooling terms from liquid nitrogen do affect the Mach number through the pressure ratio, which varies as a function of $1/\sqrt{T}$. The Mach number gain for incremental fan speed is the constant k_m , which is nonlinear in Mach number.

The tunnel total pressure is influenced by all three control inputs and hence has corresponding gain terms. The liquid nitrogen affects the pressure by the terms $\dot{T}(P/T)$ and $(P/W_g) \Delta \dot{m}_L$. The gas bleed affects total pressure by the term $(P/W_g) \Delta \dot{m}_g$, and the weakest influence is from fan speed through a gain term k_k , $bPM \frac{dM}{dt}$.

Thus, in the cryogenic tunnel model, seven of the nine gain elements are fairly dominant. Only the effect of gas bleed on Mach number and the effect of gas bleed on temperature are low. Further, the direct effect of liquid charge on Mach number can also be ignored under regulated temperature conditions.

DESCRIPTION OF THE 0.3-m TRANSONIC CRYOGENIC TUNNEL SYSTEMS

In this section, the engineering description of the 0.3-m cryogenic tunnel test facility and the various control subsystems relevant to modeling and control studies are provided (ref. 14).

0.3-m Tunnel

The cryogenic tunnel is an endless duct made up of aluminum alloy 6061-T6, which is compatible for cryogenic operation. Tunnel area vs. centerline distance has already been detailed in table 1. The tunnel is made up of 10 flanged segments which are coupled. The tunnel is anchored at the fan segment to a firm foundation, and the rest of the structure is mounted on counterbalanced supports and floating supports. The circumference of tunnel is 21.7 m with a minimum cross-sectional area of 0.1235 m^2 at test section and a maximum cross-sectional area of 1.168 m^2 . The liquid nitrogen is introduced at a distance 15.85 m along the centerline from fan exit. The gaseous bleed occurs at a location 6.9 m from fan exit. the contraction cone is 2-m long and has a contraction ratio of about 10. The volume of the tunnel is 14.1 m^3 , and it weighs 3200 kg. The tunnel shell is externally insulated by four mats of chopped untreated fiberglass loosely sewn into mats of 7.6-cm thickness each and wrapped around with a fiberglass cloth which is purged with gas (fig. 30).

Fan

The tunnel shell is pierced by a fan shaft with an appropriate pressure seal and bearing, and the shaft is driven by a two-pole induction motor capable of delivering two MW of mechanical energy. This two-pole induction motor is driven by a rotary variable frequency generator with a frequency range of 5 to 120 Hz and thus has a continuous speed control from about 300 to 7200 rpm. The variable frequency generator can be remotely controlled from the control room. The fan shaft bearing is lubricated by a heated oil lubrication system to prevent freezing of the lubricant.

The fan motor system has been identified for its dynamics at optimum tuning, and the dynamics of the fan is

$$\frac{N}{N_{set}} = \frac{1}{1 + 0.5\omega S + 0.2S^2} \quad (42)$$

The response of the system has near-critical damping and a natural frequency of 2.2 rad/sec.

Liquid Nitrogen System

Injection of liquid nitrogen requires a source pressure in excess of the tunnel pressure. In order to achieve this positive pressure, a liquid nitrogen pumping system is used. The schematic of liquid nitrogen pumping is shown in figure 31. The system consists of twin vacuum-insulated, stainless steel tanks constituting a total capacity of 212,000 liters. The storage system has a number of safety systems to maintain the boil off gases at a desired pressure of less than 3.5 atm (50 psia) and backup blowoff rupture disks to prevent overpressurization.

The two tanks feed liquid nitrogen into a cryogenic, stainless steel, centrifugal pump driven by an AC motor. The pump capacity is 500 liter/min at 10 atm pressure. Since the pump is basically a positive displacement device, the system pressure can be controlled by a pressure relief valve. This relief system is located nearly 50 m away at the tunnel. The 5-cm line carries the high-pressure fluid to the relief valve. The relief valve is an air-to-open type pneumatic actuator driving a cryogenic flow valve. The pneumatic actuator is driven from a three-term controller with a pneumatic set point generator. The line pressure is sensed by a pressure transducer and is converted into a pressure signal to be fed to the controller. This relief system can regulate the liquid pressure, and the pressure system dynamics has a 6 rad/sec bandwidth and 0.8 damping. The output of the relief valve is returned to the top of the tank through a 50 m long 5 cm line. The tunnel is fed from the regulated section of the liquid nitrogen line through four digital valves.

Liquid Nitrogen Control Valves

The liquid nitrogen flow into the tunnel is controlled by four digital valves. The digital valve has a number of solenoid-operated elements which are pure binary weighted. The valve flow coefficient is 4. The smallest

element allows 1/1024 of full open, and subsequent elements progressively double their area. All the elements are solenoid operated and have a sonic nozzle. The flow equation is

$$\dot{m}_L = \frac{C_d}{56.805} \sqrt{\rho_L \Delta P} \cdot A_L, \quad 0 \leq A_L \leq 1$$

step size = 1/1024

or

$$\dot{m}_L = 3.47 \sqrt{P_{LN} - P} A_L \text{ kg/sec}, \quad k_L \leq 3.47 \sqrt{P_{LN} - P} \quad (43)$$

for a liquid nitrogen density of 0.804.

Gas-Bleed Valves

The cryogenic tunnel pressure shell is certified for six atm. To prevent the possibility of overpressurization, the settling chamber has three large bleed valves open to atmosphere, each controlled pneumatically. The valves are air-to-close type to allow fail safe shut down. Each valve can be separately controlled from the control room. One of these valves is cascaded with a 10-element digital valve meant for closed-loop operation. In view of the large areas necessary to control gas flow at low pressure differentials, the elements of the digital valve are air-piloted solenoid valves. The valve flow areas are binary weighted sonic nozzles.

Such a valve has a flow, which under choked conditions, is

$$\dot{m}_g = C^* \sqrt{\frac{gC}{RT}} \rho A^* C_d$$

Assuming a $C^* = 0.7$ and a valve coefficient of 8,

$$\dot{m}_g = 21.8 \frac{P}{\sqrt{T}} A_g \text{ kg/sec}, \quad 0 \leq A_g \leq 1, \text{ step size} = 1/256 \quad (44a)$$

when the pressure ratio across valve is very low unchoking occurs. Then

$$\dot{m}_g = 21.8 \frac{P}{\sqrt{T}} A_g \left[2 - \left(\frac{1.5}{P} \right)^{1.7} \right] \text{ kg/sec} = k_g \frac{P}{\sqrt{T}} A_g \text{ kg/sec}$$

for $1 \leq P \leq 1.5$ (44b)

Summary of Modeling Effort

Hitherto the synthesis of a lumped multivariable model of a closed-circuit, transonic, cryogenic pressure tunnel with specific reference to the 0.3-m cryogenic tunnel was discussed. The three input/three output model so generated describes the tunnel variables in terms of tunnel physical parameters, thermophysical properties of nitrogen, and the tunnel control input in an explicit manner. The tunnel model embraces the global envelope of operation and demonstrates the interactive nature of the process and its nonlinearities.

In deriving the lumped multivariable model of the cryogenic tunnel, obviously some of the faster dynamic modes of the tunnel have been suppressed. A heuristic study of the cryogenic tunnel flow phenomena indicates possible dynamic modes described by eigenvalues attributable to turbulence modes, acoustic adiabatic modes, two-phase flow induced modes, circuit modes, gas and metal thermal modes, and the slow mass-energy integration modes, in a descending order in frequency. In the lumped model synthesized here, the faster modes like circuit, acoustic, and turbulence modes have been ignored, because they constitute the uncontrollable modes for the degrees of freedom available at control inputs.

VALIDATION OF THE MODEL

A model of a physical process can be validated only by comparing it with the actual process. Such a comparison can be at parametric level or at a performance level. In the former, the actual process records can be analyzed using modern identification procedures to arrive at tunnel gain parameters and transient parameters. The parametric identification of process is an involved procedure which requires input disturbance design and experimental record analysis using identification procedures. Identification of nonlinear systems is difficult. In the case of comparison of performance, the model can be used to predict the process response for various types of inputs, and the actual tunnel responses and the predicted responses can be compared for quasi-steady-state and transient responses.

In the present research effort, the latter route of comparing time responses of the tunnel to the predicted time responses of the model was chosen. In order to generate the model responses, a real-time simulator was developed which is a true electrical analog of the process equations and model derived in the previous section. In the following sections, the details of the development of such a real-time cryogenic simulator are discussed.

SIMULATION OF THE 0.3-m TRANSONIC CRYOGENIC TUNNEL PROCESS

The methods available for simulating any process in real time are on analog, digital or hybrid computers. Analog computation is very fast, but its accuracy and its ability to perform accurate nonlinear computations are very limited. Digital computation is very accurate and its speed because of serial operation is limited by the quantity of computation. Hybrid analog-digital computers with dedicated digital processors provide an efficient means for combining speed and interactive features of the analog computer with the accuracy of digital computers. In the present effort, the simulator of the 0.3-m cryogenic tunnel process has been carried out on a hybrid computer.

Hybrid Computer

The hybrid computer system used to develop the 0.3-m transonic cryogenic tunnel simulator consists of (1) a 16-bit, 32-k memory digital processor with a cycle time of 1 usec and a floating point hardware for arithmetic, (2) a 10-V, 100 amplifier analog processor with logic and nonlinear units, (3) an interface hardware unit consisting of analog to digital converters and digitally controlled attenuators, and (4) an interface system between the processors for control, logic, and high-speed data interface.

The hybrid computer has I/O units in the form of a card reader, line printer, a CRT control unit, a cassette tape unit, and an analog recording system. The real-time operating system is through a real-time operating system and allows use of real-time FORTRAN and assembler.

Simulator Display and Control Unit

In order to achieve real-time interactive simulation of the 0.3-m cryogenic tunnel to allow man-in-the-loop operation, a control display unit similar to the actual tunnel control was made. The operator controls consist of a fan speed control, liquid nitrogen valve area control, and gaseous nitrogen bleed area control. The operator displays are gas and average metal temperature in Kelvin, test section Mach number to 0.001 resolution, and tunnel total pressure in psia (0.07 atm steps) with a resolution of 0.1 psia (0.007 atm). The operator display and control unit is shown in figure 32. The other displays

on this unit are the fan speed in rpm and the gas valve and liquid valve areas in percent of full opening.

The hybrid scheme used for simulation has been to compute nonlinear terms on the digital processor and the linear dynamical terms on the analog processor. The digital computer work load is shown in figure 33 along with the hybrid scheme. The 15 listed computations are the typical ones and are carried out in about 35 msec.

The numerical inputs to these computations are derived from the outputs of the ADCS appropriately scaled into engineering units compatible with the process equations (36) through (44). The computed outputs are rescaled into analog processor units and are fed to the analog processor through digitally controlled attenuators. This cycle of analog and digital computation update occurs at a rate of 25 Hz.

The analog processor handles the linear dynamic terms in real-time scale and amplitude scaling based on static quantities. Only the temperature derivative \dot{T} is rescaled in its amplitude. The analog processor runs continuously in real time and its coefficients are updated by the digital processor once every 40 msec. The appendix provides the typical digital processor program used. Figures 34 through 37 provide the detailed analog processor patching.

The temperature dynamics of the tunnel is patched as shown in figure 34. The gas temperature is obtained by integrating \dot{T} , which in turn is obtained from subtracting $\dot{Q}_t/W_g C_v$ from $\dot{T} + \dot{Q}_t/W_g C_v$. The temperature data is bootstrapped to generate metal temperature T_m using time constant t_m . Figure 34 details generation of gas temperature, metal temperature, and the thermocouple output.

The analog scheme for generating pressure, fan and Mach dynamics is shown in figure 35. The total pressure P is derived from integrating \dot{P} and accomodating the fan speed coupling. The second order fan dynamics is shown and uses two integrations with the \dot{N} integrator being limited to -600 rpm/sec acceleration. The test section Mach number dynamics is a simple first order filter.

In figure 36, the details of the liquid and gas valve drive are described and the provisions for manual control, transient pulsing with known amplitude

and period, and closed-loop control are shown. In figure 37, the closed-loop controllers for pressure and temperature loop are shown. These loops are the proportional-integral type and have loop gain scheduling built into them.

Thus figures 33 to 37 detail the analog segment of the hybrid computation. The analog segment has provisions for creating initial conditions for P, T and M: The analog processor has continuous performance, and 10 analog quantities, viz P, T, M, N, A_L , A_g , P_{LN} , $30 \dot{T}$, t and T_m , are AD-converted and fed to the digital processor. Thus, totally the system represents a hybrid scheme for simulating the 0.3-m cryogenic tunnel.

The digital processor program was written in REAL FORTRAN and assembler (Appendix), and the system was run continuously, updating being at 25 Hz. The bandwidth of the process is no more than 1 to 2 Hz, and hence the system is truly continuous.

The system response were recorded on a 40-sample/sec digital recording system for processing and further analysis.

PERFORMANCE TESTS

Three types of validation performance tests were performed, both on the cryogenic tunnel proper and its simulator: steady-state equilibrium tests, quasi-steady long-term warmup/cool down tests, and transient response tests. The tunnel and the simulator performances were then compared to check for validation of time responses. Further, the responses were correlated with the math model terms.

Transient Response Tests

It is well known that linear time-invariant systems yield characteristic responses to deterministic input disturbances. The cryogenic tunnel is time invariant but has a nonlinear, complex structure. However, by assuming local linearity the system can be made to yield transient responses which can be interpreted on the basis of linear system responses. The cryogenic tunnel model has integration type dynamics in pressure and temperature. Hence step inputs cannot be used because of resulting divergent responses. Sinusoidal inputs are difficult to realize in respect to liquid and gas flow. Hence impulse response testing has been resorted to.

During the impulse response tests, both the 0.3-m transonic cryogenic tunnel and its simulator were first balanced at specified equilibrium conditions by open-loop adjustment of the three control inputs. Then the tunnel and the simulator were subjected to impulse disturbances of liquid nitrogen flow, gaseous nitrogen bleed flow, and fan speed at successive intervals. In order to study the dynamic behavior of the tunnel and its simulator over the entire range of tunnel operational envelope, the tunnel variables P , T and M were scanned from $P = 1.5$ to 5 atm, $T = 100$ K to 275 K and $M = 0.3$ to $0.75/0.9$ in 27 different combinations as in table 3.

The amplitude and the period of the pulse were chosen so as to produce easily measurable changes in the tunnel variables. Thus a 6.25 percent of full area increment to the liquid nitrogen and gas bleed valves and a 100 rpm decrement to fan speed were chosen for the pulse amplitude. The period of pulse was uniformly 3 sec, which corresponds to 0.75 to 4 circuit periods. Typical responses to these pulses were 0.5 to 6 K in T , 0.016 to 0.1 atm in P

and 0.006 to 0.03 in M . A 30-sec settling time was allowed between pulses. Tests on the tunnel and the simulator were performed separately.

The tunnel and the simulator responses for identical tunnel conditions are presented in matched pairs in figure 38 to 64. These correspond to tunnel conditions in table 3. The tunnel responses were generated by a manual operator induced 3-sec pulse whose period was only approximate. The liquid nitrogen pressure also fluctuated between 10 to 20 percent off the nominal. This prevented precise knowledge of either $\dot{\Delta m}_L$ or $\dot{\Delta m}_g$, the incremental flow. An inspection of the figures 38 to 64 indicates noise-free responses on the simulator and noisy responses on the tunnel, particularly in respect to Mach number.

The typical impulse response of the tunnel is presented as a response trajectory A through K for the total pressure test section Mach number and total temperature. These response trajectories A through K are now analyzed for each control input pulse.

Liquid Nitrogen Pulse Input

The trajectories ABCD, of typical responses in figure 38 (55 or 56), correspond to tunnel dynamics in P , T and M for a liquid nitrogen pulse input. Prior to point A, the cryogenic tunnel is in equilibrium with $\dot{P} = \dot{T} = 0$ and $\dot{m}_L = \dot{m}_g$. During period AC of the trajectory, an extra liquid flow $\dot{\Delta m}_L$ is imposed on the tunnel.

The tunnel gas temperature T reduces in period AC, due to negative \dot{T} as in equation 39. Since the wall temperature lags the tunnel gas, \dot{T} is largest at A and progressively reduces in period AC as dictated by the lead lag term. This effect is due to wall heat release described by metal time constant t_g . At point C, the extra liquid nitrogen is cut off. The gas temperature gradient \dot{T} is now positive because of metal being warmer than gas. Hence gas temperature T increases in period CD, and at point D bulk of heat transfer effects are complete. The metal and gas temperatures stabilize. A transport delay between gas temperature and command, corresponding to particle transit time from liquid injection station to settling chamber, is noticeable.

The gas temperature at point C is lowest and ΔT away from the starting value. This ΔT can be related to transient temperature gain of figure 28. Study of tunnel and simulator responses to liquid nitrogen pulse, of figures 38 to 64, generally confirm the relations of figure 24. At low gas weight (figs. 56 to 58) ΔT is very large, and at high gas weight (figs. 44 to 46) ΔT is smallest. However discrepancies between tunnel and simulation responses are evident in figures 56 to 58. Since the tunnel responses are from a thermocouple, the differences can be attributed to first order filtering that occurs in this sensor.

The total pressure trajectory ABCD can now be analyzed (figs. 38, 55, 56). As detailed in equation (40), the total pressure gradient \dot{P} is the sum of a cooling term $\frac{P}{T} \dot{T}$ and a mass term $\frac{P}{W} \Delta \dot{m}_L$. During period AB the cooling term is greater than the mass term and \dot{P} is negative. At point B, the two are equal and pressure is at a minimum. During period BC the mass term is greater than the cooling term and \dot{P} is positive despite \dot{T} being negative. At point C the excess liquid flow is made zero and \dot{P} continues to be positive because of term $\frac{P}{T} \dot{T}$. At point D pressure stabilizes on completion of bulk of heat transfer.

Thus a typical pressure response of the cryogenic tunnel to a liquid flow pulse is characterized by pressure falling initially and after reaching a minimum the pressure starts rising during the pulse period. All 27 pressure responses, of figures 38 to 64, reveal this signature of the tunnel.

In case of low temperature 100 K responses, of figures 33 to 39, the minimum pressure point consistently occurs at or very near point C in both the tunnel and the simulator. Thus at low temperatures cooling effect $P \frac{\dot{T}}{T}$ dominates the mass effect because of relatively poorer heat release from the walls. It may be noted that at 100 K metal enthalpy is 12 percent of that at 300 K, as in equation (11). Hence pressure rises over the period BD are relatively small.

In contrast, the high temperature runs at 275 K (figs. 56 to 64) consistently locate the minimum pressure point B at or very near A, indicating a dominant $\frac{P}{W_g} \Delta \dot{m}_L$ over the cooling term $P \frac{\dot{T}}{T}$. Hence the tunnel pressure rises almost from the instant of liquid injection. The pressure rise in period BD is comparatively larger because of higher metal enthalpy, lower gas weight,

and high specific heat of metal [eqs. (9) and (10)]. The tunnel and simulator responses demonstrate this feature.

The 200 K runs (figs. 47 to 55) show a minimum point B occurring at all phases of AC. The point B shifts from near A (as in fig. 44) to C (as in fig. 48) with increasing gas weight and reduced Mach number (corresponding to lower convection heat transfer).

The pressure gradient at the peak pressure near point D in the post-LN₂ pulse period makes an interesting point of study. At its peak near point D, the gas bleeding is greater than \dot{m}_L [eq. (40)] and the pressure gradient is a function of A_g . The steady state A_g [eq. (26b)] exponentially increases with Mach number. Hence largest \dot{P} occurs at $M = 0.75/0.9$ as in figures 49, 52, 55, 58, 61 and 64, and \dot{P} is smallest at $M = 0.3$ as in figures 47, 50, 53, 56, 59 and 62. However, since peak pressure P is very nearly the same as starting at 100 K, these effects are not very evident in 100 K runs (figs. 38 to 46). Both the tunnel and the simulator confirm the features discussed. No transport delay is evident in the response.

The Mach number trajectories ABCD of figures 38, 55 and 56 can now be analyzed. In the period AC, the Mach number rises linearly and reaches a maximum at C. This can be explained as being due to change in the fan pressure ratio caused by cooler gases passing through the fan. The fan performance at constant speed can be noted to be of type $M\sqrt{T}$ and is constant [eq. (41)]. Since the tunnel gas temperature drops in AC, the Mach number rises. Similarly, during period CD the extra liquid is made zero and temperature rises; hence Mach number drops linearly to the original value.

At point C, the Mach number is largest and has an incremental value ΔM . This response amplitude can be related to gas temperature by equation $\frac{\Delta M}{M} = - \frac{\Delta T}{2T}$ derived from equation (41). The actual ΔM in all the runs of figures 38 to 64 can be used to estimate ΔT . Typically, in figure 38, the test section Mach number is 0.30 with $\Delta M = 0.006$ at 100 K, which corresponds to ΔT of -4 K. However, the recorded ΔT is only -1.5 K, and the difference can be attributed to attenuation caused by the first order dynamics of thermocouple. In all the 27 cases, the tunnel and simulator responses show good agreement. No transport delay occurs since the coupling is through fan.

In summary, the response trajectories of the tunnel variables to a liquid nitrogen pulse correlate well with the math model responses predicted by the simulator. Pressure responses with a minimum occurring during pulse period show a characteristic signature of a cryogenic tunnel with metal in the tunnel. The model and tunnel responses agree quite well over the entire range of tunnel operation. The test section Mach number responses also show generally good agreement throughout. Relatively poorer agreement in gas temperature responses are evident in some cases. This can be attributed to thermocouple dynamics. Since Mach number match between the tunnel and the model are good and temperature predictions based on Mach numbers do agree well, it appears that the thermocouple response varies as a function of P , T and M . Further, transport delay effects are evident in all the tunnel and model responses and agree generally.

Gaseous Nitrogen Bleed Pulse

The response trajectories EFG correspond to the tunnel dynamics in P , T and M for a gas bleed pulse input. Prior to point E, the cryogenic tunnel is almost in equilibrium with $\dot{P} = \dot{T} = 0$ and $\dot{m}_g = \dot{m}_L$. During period EF, the gas valve is incrementally opened to allow an extra flow $\Delta\dot{m}_g$ out of the tunnel.

The tunnel total pressure P drops linearly with a negative \dot{P} . This gradient is caused by mass term $\frac{P}{W_g} \Delta\dot{m}_g$ and by a second order $\frac{P}{T} \dot{T}$ term. The contribution of the cooling term is very small. The pressure P reduces linearly in the period EF. At F the incremental valve area is made zero and $\Delta\dot{m}_g = 0$. However, the pressure at point F is lower than the starting valve and hence \dot{m}_L is greater than \dot{m}_g , resulting in a positive gradient for \dot{P} during FG.

The pressure at F is lower than the starting pressure by a magnitude ΔP , which is a function of $\frac{P}{W_g} \Delta Q_g$ and in turn is proportional to $P\sqrt{T}$. The largest gradient occurs at $P = 5$ atm and $T = 275$ K as in figures 62 to 64, and the smallest gradient occurs at $P = 1.5$ atm and $T = 100$ K as in figures 38 to 40. The tunnel and the simulator responses agree well throughout as in figures 38 to 64.

During period FG, the pressure gradient is positive and is a function of steady-state valve opening A_g . However the valve A_g is a function of fan power and is largest at $M = 0.75/0.9$. Thus the pressure recovery is fastest at $M = 0.75/0.9$ as illustrated in figures 40, 43, 46, 49, 52, 55, 58, 61 and 64 and slowest at $M = 0.3$ as in figures 38, 41, 44, 47, 50, 53, 56, 59 and 62. No transport delays are evident in the tunnel pressure responses.

The tunnel gas temperature T shows a very poor coupling to gas bleed. Energy equation (39) predicts a negative T for gas bleed. This gain sensitivity is shown in figure 29 and is comparatively very low because $\alpha < \beta$. During the period EF the temperature tends to drop but is filtered by the lead lag term due to wall heat release. The temperature T at F can be approximated to $\frac{\alpha}{W_g C_v} \Delta Q_g$. Since ΔQ_g is a function of P/\sqrt{T} , ΔT is only a function of temperature T , the largest responses occur at 275 K and smallest at 100 K. Figures 38 to 64 generally confirm this, but many of the responses are small in amplitude. The temperature recovers slowly in period FG to its original value because of continued heat release.

The tunnel Mach number responses to gas bleed pulse are insignificant. The coupling between Mach number and gas bleed occurs dominantly through temperature only. The test section Mach number is related to pressure by a very weak empirical function $P^{0.035}$ and can be ignored [eq. (41)] for small perturbation. In principle, during period EF the Mach number ought to rise, demonstrate a peak at F, and fall back to original value by B. In the tunnel responses, the noise submerges these changes. In the model responses which are noise free this effect can be observed in figures 38 to 64.

In summary, the tunnel responses to a gas-bleed pulse correlate well with the model predictions in the form of simulator responses. The most dominant effect of gas bleed is in respect to total pressure, which falls linearly as predicted. The temperature responses to the gas bleed pulse are quite small, and the simulator predictions agree generally. The Mach number responses of the tunnel to gas-bleed pulse are very insignificant.

Fan Speed Pulse Input

The response trajectories HJK correspond to the tunnel dynamics in P, T, and M for a fan speed pulse input. Prior to point H, the cryogenic tunnel is almost in equilibrium with $\dot{P} = \dot{T} = 0$ and $\dot{m}_L = \dot{m}_g$.

During period HJ, the fan speed command is reduced by 100 rpm and the fan decelerates as defined in equation (42) in a second order fashion. The decreasing speed results in reduced fan pressure ratio, which in turn manifests itself as decreasing Mach number profile HJ. During the period JK, the fan is accelerated back to original speed by restoring full speed. The fan pressure ratio increases gradually in JK as does the Mach number and is restored to near original value at K. The Mach number response of the cryogenic tunnel to a fan speed pulse is almost a linear fall in HJ and a linear rise in JK with maximum deviation ΔM occurring at J. This ΔM is related to $\Delta N/\sqrt{T}$ as in equation (41). Since ΔN is constant for all the runs, ΔM is proportional to $1/\sqrt{T}$. The largest decrement of about 0.034 occurs at 100 K (figs. 38 to 46), and the smallest occurs at 275 K (figs. 56 to 64). The model and the tunnel Mach number responses match reasonably well throughout. The Mach number response to fan speed pulse has another constituent via temperature drop which opposes the pressure ratio effect. However, its contribution is very small. The Mach number responses to fan speed do not indicate any transport delays.

The tunnel total temperature trajectory HJK, due to fan speed drop, shows a reducing temperature T in the period HJ and a very slow rise in JK. This is due to decreasing \dot{Q}_F in HJ, which results in a negative T, which is affected by wall heat release, as in equation (37). The maximum deviation occurs at J, when the original fan speed command is restored, and \dot{Q}_F reaches normal value at K. During period JK the gradient \dot{T} is changed from negative to positive due to wall heat release.

The fan power drop $\Delta \dot{Q}_F$ is maximum at J and is proportional to $P\sqrt{T} f(M)$ as in equation (25). Thus maximum ΔT occurs when $\Delta \dot{Q}_F$ is maximum as at $M = 0.75/0.9$, $P = 5$ atm, and $T = 275$ K as in figure 64. The lowest response occurs at $M = 0.3$, $P = 1.5$ atm, and $T = 100$ as in figure 38. The trajectories HJK in temperature show a time delay from

command to response corresponding to particle transit time from fan to settling chamber, which is a function of tunnel circuit time. The tunnel and model responses agree with each other in their temperature responses generally (figures 38 to 64) and confirm their relation to $\Delta \dot{Q}_F$.

The tunnel total pressure trajectories HJK, due to fan speed pulse, can be analyzed using equation (40). The pressure gradient is contributed to by $\frac{P}{T} \dot{T}$ and by k_k , BMP $\frac{dM}{dt}$. During the period HJ, \dot{T} is negative and $\frac{dM}{dt}$ is negative. Hence \dot{P} is negative and pressure continues to fall during HJ. At J the fan speed command is restored and $\frac{dM}{dt}$ is positive with \dot{T} slowly reaching a positive value in the period JK. The maximum pressure deviation ΔP occurs at J. Since the effect $\frac{dM}{dt}$ is most dominant, ΔP can be related to product MP. Thus largest ΔP occurs at $P = 5$ atm and $M = 0.75/0.9$ as in figures 46, 55 and 64. The smallest ΔP occurs at $P = 1.5$ atm and $M = 0.3$ as in figures 38, 47, and 56. The pressure responses do not show any transport delay features to fan speed command.

In summary, the fan speed pulse on a cryogenic tunnel creates a dynamic change in all tunnel variables M, P and T. The Mach responses are most dominant and are functions of $1/\sqrt{T}$. The pressure and temperature responses are functions of fan power and are evident only at high P and M. Transport delay effects are observable only in respect to tunnel temperature. The tunnel responses generally agree with the model responses predicted by the simulator.

Tunnel responses of figures 39, 52 and 57 need clarification. Oscillatory responses of figure 39 were caused by inadvertent cycling of one of the smaller elements of the gas valve. The fan rpm command in figure 52 actually consisted of a 0.5-sec pulse followed by a 3-sec gap and another 3-sec pulse. All the tunnel variables show the cumulative effect of twin pulses. In figure 57, the large temperature response of the tunnel for LN_2 flow was caused by a five-sec LN_2 pulse.

QUASI-STEADY-STATE TESTS

In addition to the transient response test, studies on the cool down of the tunnel from ambient and warmup of the tunnel to ambient, using excess liquid nitrogen flow and excess fan heating respectively, were conducted in order to validate the long-term dynamics of the heat transfer model.

The basic energy equation of the cryogenic tunnel process is

$$W_g C_v \frac{dT}{dt} + C_v T (\dot{m}_L - \dot{m}_g) = \dot{Q}_F + \dot{m}_L h_L - \dot{m}_g C_p T - \int \dot{Q}_t^{\text{Surface}}$$

where

$$\int \dot{Q}_t^{\text{Surface}} = \frac{W_t C_m T_s}{1 + t_m S} = (T - T_m) y$$

In order to prove this heat transfer model, time histories of average metal temperature T_m and gas temperature T were recorded for ordered energy input terms. Matches between temperature, metal to gas temperature difference, and time were sought for the tunnel and simulator quasi-steady-state responses.

Cool Down Studies

The tunnel cool down test consisted of starting with a metal and gas temperature at ambient of 290 K and running the tunnel with excess liquid nitrogen flow while the tunnel pressure and low fan speed were maintained constant.

Under these conditions $\dot{m}_L \approx \dot{m}_g$ because of constant pressure and $\dot{Q}_F \ll \dot{m}_L (h_L - C_p T)$ because of low fan speed, then

$$W_g C_v \frac{dT}{dt} = - \int \dot{Q}_t^{\text{Surface}} + \dot{m}_L \beta$$

$$\dot{Q}_t = (T - T_m) y \quad ; \quad T_m = \frac{T}{1 + t_m S}$$

The tunnel and the simulator were balanced at an equilibrium condition of 290 K, 1.5 atm at 1200 rpm. The liquid nitrogen pressure was maintained at

6 atm. The tunnel cooling was started by rapidly opening the liquid valve to 12.5 percent open, corresponding to about 1 kg/sec flow. The tunnel pressure was maintained at 1.5 atm throughout. Gradually the tunnel metal cooled down, and time histories of gas temperature, metal temperature at a forward diffuser leg location (fig. 23) and the test section Mach number were recorded. Figure 65 shows the time histories of tunnel gas and average metal temperature, the tunnel gas and metal pressure. The tunnel cooling was taken down to about 100 K in about 35 min. It may be noted that model and the tunnel temperature histories match reasonably well. An initial gas to metal temperature difference of about 65 K (at 290 K) and a final difference of 15 K (at 100 K) occur in both the tunnel and simulator. The simulator and tunnel temperatures agree to within 5 K over most of the cooling period except at the very end where the difference is 10 K. This can be attributed to heat gains through some flanges in the actual tunnel which make cool down a bit slower. The Mach number time histories of tunnel and simulator agreed to better than 0.005, starting from an initial value of 0.140 and ending with a value of 0.228. The total quantity of liquid nitrogen consumed for cool down from 290 K to 105 K was determined for both the tunnel and simulator. The tunnel value was 1825 kg against a simulated consumption of 1800 kg. Thus, a fairly good match between the tunnel and the model for a quasi-steady-state cool down confirmed the heat transfer modeling used.

Warmup Studies

The tunnel warmup test consisted of starting with a cold tunnel with both the gas and metal at 100 K, and then running the tunnel at fairly high Mach number with the liquid flow fully cut off and the tunnel pressure maintained constant, then

$$\dot{m}_L \approx \dot{m}_g = 0 \quad \text{and} \quad \dot{Q}_F \gg \dot{m}_g C_p T$$

$$W_g C_v \frac{dT}{dt} \approx \dot{Q}_F - \int \dot{Q}_t^{\text{Surface}}$$

$$\int \dot{Q}_t = \frac{W_t C_m T S}{1 + t_m S}$$

$$\dot{Q}_F = \frac{K_F P M^3 \sqrt{T}}{(1 + 0.2 M^2)^3}$$

Both the tunnel and the simulator were cooled to 100 K and were balanced at 100 K, 2 atm, and a Mach number of 0.6.

The warmup was started by cutting off the liquid nitrogen flow into the tunnel, then maintaining the tunnel pressure and Mach number by fine adjustment of the gas valve area and fan speed. Records of gas temperature and the average metal temperature were taken as functions of time. The average metal temperature in the tunnel occurs and is sensed at a location in the forward leg diffuser (see fig. 23), which provides a metal time constant as a function of tunnel space. The warmup profile of the tunnel and the simulator at $M = 0.6$, $P = 2$ atm from 100 K to 300 K is shown in figure 66. The metal to gas temperature differences agree very well. However, the tunnel shows an initial warmup rate lower than the simulator, and this has been attributed to an initial tunnel pressure of less than 2 atm. Subsequently the tunnel and simulator warmup gradients match quite well. The metal to gas temperature difference in the tunnel and the simulator agree to within 2 K, indicating the adequacy of the heat transfer model.

Validation

In summary, the 0.3-m transonic cryogenic tunnel and its model responses show acceptable agreement, not only in their transient responses to various control inputs over the entire range of operational envelope, but also in their long-term quasi-steady-state warmup and cool down characteristics. All the features of the transient and quasi-steady responses correlate well with math model predicted effects.

This overall steady-state, transient, and quasi-steady long-term response match leads to the conclusion that the model is a basic representation of the tunnel and that the model is validated.

CONCLUDING REMARKS

In this report, the development of a control compatible mathematical model of a liquid nitrogen cooled, gaseous nitrogen operated, transonic, cryogenic pressure tunnel has been detailed. Utilizing the thermophysical properties of liquid nitrogen, gaseous nitrogen, and the tunnel metal aluminum, the thermodynamics and the flow dynamics of the cryogenic tunnel have been analyzed. The concept of controlling the energy state of tunnel gas provided a simple understanding of the energy associated with various physical processes occurring in the tunnel. The metal enthalpy was proven to be the most dominant store of energy in the system followed by the internal energy of the gas. The flow-induced energy terms, other than wall friction, turned out to be a very insignificant fraction of the total energy of the system, thus providing an idea of relative importance to be attached to various energy storage terms.

The basic control inputs to the tunnel were identified as rate vectors of gas mass and energy either entering or leaving the system. The tunnel insulation makes the system an autonomous thermodynamic system with mass and energy crossing the boundary. This open thermodynamical system was analyzed in order to arrive at a very simple, lumped, multivariable, global, mathematical model of any closed circuit, cryogenic pressure tunnel. The parameters of this model are nonlinear functions of thermophysical parameters of the tunnel metal and gas and tunnel variables.

Secondly, validation of the lumped, multivariable model using the tunnel transient and quasi-steady-state responses was discussed. The validation has been based on matching the impulse responses of the tunnel with the model. The model responses for various disturbances were derived using a cryogenic tunnel simulator. The cryogenic tunnel simulator is an interactive real-time simulation of the various model equations realized on a hybrid computer. The hybrid computer uses the digital processor to estimate complex nonlinear product terms, which updates a continuous running analog computer.

The validation has been demonstrated by good agreement of both transient and quasi-steady responses between the tunnel and the simulator under similar operating conditions.

ACKNOWLEDGMENTS

The author wishes to acknowledge and thank the following persons from NASA/LARC for their contributions to this project:

- Dr. R.A. Kilgore for his overall direction of the modeling effort.
- J.J. Thibodeaux for his contributions and participation in the hybrid simulation and tunnel studies.
- J.B. Adcock, C. Johnson and P. Lawing for their data inputs to the physical modeling.

The author further wishes to acknowledge participation of Dr. G.L. Goglia, professor and chairperson, Department of Mechanical Engineering and Mechanics, Old Dominion University in the project effort and thank him for his administrative guidance.

APPENDIX

RUOH COMPILER OUTPUT FOR TEST PROGRAM

SEOF JUTRO2

DIMENSION IDEL(3),VAROUT(3),VARIN(3)

DIMENSION X(4),Y(3),Z(5)

REAL MOV

REAL A,B,M0,BL,K6,M1,M4SC

REAL VARG(3),STACK(3,51),V(5)

SCALED FRACTION VAL(13)

LOGICAL IS

INTEGER CUESCR

LOGICAL SEHS

COMMON IDEL,VARGOUT,VARIN,VARG,STACK,V

INTEGER ISIA(4) (0,-1)

EQUIVALENCE (STACK(1,1),ISTACK(1,1))

EXTERNAL CUESCR

DATA JM/JM/3.51/

DATA VARG/0.0.0.0.0/

DATA PS/0.5000/

DATA P04/74HP047/

DATA SP/0.0025/

DATA P048/4HP048/

DATA PD/0.0025/

DATA P042/4HP042/

DATA PV/0.0030/

DATA P053/4HP053/

DATA RP/0.2500/

DATA P112/4HP112/

DATA VP/0.5000/

DATA P118/4HP118/

DATA S/0.151/

DATA P077/4HP077/

DATA ST/0.0002/

DATA P078/4HP078/

DATA SC/0.1450/

DATA P079/4HP079/

DATA SP/0.0051/

DATA P080/4HP080/

DATA SF/0.1184/

DATA P081/4HP081/

DATA P046/4HP046/

DATA CT/0.25/

DATA P058/4HP058/

DATA VM/0.10/

CALL CSBYIN(IEPS,680)

CALL OSC(1,IEPS)

CALL CSIPIN

CALL TIME0

CALL OSCIN(1,IEPS)

CALL DELAY0(STACK,3,51,VARG,V)

```

CALL PSSM1
ISW=.TRUE.
CALL QPR(P047,PS,IEPR)
CALL QPR(P048,SP,IEPR)
CALL QPR(P052,EF,IEPR)
CALL QPR(P053,PV,IEPR)
CALL QPR(P112,RP,IEPR)
CALL QPR(P118,VP,IEPR)
CALL QPR(P077,SW,IEPR)
CALL QPR(P078,ST,IEPR)
CALL QPR(P079,SC,IEPR)
CALL QPR(P090,SG,IEPR)
CALL QPR(P081,SF,IEPR)
CALL QPR(P046,CT,IEPR)
CALL QPR(P058,VV,IEPR)
6 CONTINUE
VOL=0.0
IT=0
TIME=0.0
10 CALL QPRALR(X,0.9,IEPR)
CALL TIMER(IT)
RIT=IT
DELT=0.0001*RIT
TIME=TIME+DELT
VOL=VOL+ML*DELT
IF (SENS(2)) GO TO 93
GO TO 91
93 IT=0
TIME=0.0
VOL=0.0
91 CONTINUE
ISW=.NOT. ISW
CALL QCELL(0,ISW,IEPR)
P=X(1)*10.
T=X(2)*800.
M=X(3)
N=X(4)*12000.
AL=X(5)
IF (AL .LE. 0.) AL=0.
AG=X(6)
IF (AG .LE. 0.) AG=0.
PL=X(7)*30.
TDT2=X(8)*25.666
QV=3.47*SQR(PL-P)
TM=X(9)*800.
VARIN(1)=AG
VARIN(2)=T
VARIN(3)=M
MASC=M**2

```

```

      SBT=S*BT(T)
      IE=0.0*(1.0+.2*(S-1.0)*2/2-1)
      T7=0.1*IE
      IE=0.0*IE
      T9=0.4*IE
      IDEL(1)=I7*25
      IDEL(2)=IE*25
      IDEL(3)=I9*25
      IF (ABS(VL-1(3)-VLSI).LT. 1000.) GO TO 30
      WRITE (16,99) VFI(3),VL-SI
30 CONTINUE
      VLASI=VFI(3)
      CALL DELAY(IDEL,1,1,0,0,0)
      IF ((P-1.0).LT. 0.) GO TO 12
      GO TO 13
12 MG=21.0*P*V*(2.-(1.5/2)*1.7/2)/S-T
      GO TO 14
13 MG=21.0*P*V/S-T
14 VL=2.0/59*V*(PL-4)*L
      VL=1.5/59*V*(2.77-1*(5**0.635)/170./S-T)
      IF (T.LT. 15.) GO TO 17
      GO TO 21
17 BT=0.
      GO TO 22
21 BT=-121.-2.8*P-T
22 ALP=0.3*BT-0.0*BT
      CV=0.75*P
      BT=3280.
      TEMP=BT**2
      CM=(5.5*BT'-0.0*BT*(T*BT'))/1000.
      SG1=0.0*BT**4*2.0*(1.0+250.0*BT/P)/T
      SG=SG1*(1.0-0.133*(5**1.5))
      T2=0.2*(T**1.0)/(P**0.000.7)
      T+=5.4*(P**0.10)/(T**0.45)/(P**0.7)
      T1=4.
      T4=4.
      H=0.44*BT/S-T/(1.0-0.3*BT)
      K6= 0.008/(1.0-0.3*BT)/((1.0+0.2*(.650))**3)
      HEAT=P*BT**4*50***(1.0-7.0*BT/T)
      TOT1=-L*(BT+ALP)-5*BT*P+HEAT
      TOT=TOT1/CG/CM
      PBT=P*VL/CG-P*BT/(1.0*BT*T2/T)
      Y(1)=PBT
      Y(2)=TOT/500.
      Y(3)=1
      Z(1)=4.
      Z(2)=1./T2
      Z(3)=BT*(T/(5**CV*T2))
      Z(4)=5*BT*P/(P)/50./V/T

```

```

      Z(5)=Z(2000)
      Z(6)=7.5/P/SCRT(T)
      Z(7)=Z(3)
      Z(8)=Z(2)
      IF (SENS(3)) GO TO 10
      GO TO 10
10  TYPE 95,2,I,M,B,T,TOT2,G,TX
11  FORMAT(2X,2HP=.F6,3,2X,2HT=.F5,0,2X,2HN=.F4,3,2X,4HMDT=.F8,5,2X,
12  14HTDI=.F6,3,2X,3HVC=.F5,0,3HTI=.F6,2)
      TYPE 85,M,L,M,G,FEAT
13  FORMAT(2X,3FH,2)
      TYPE 87,VOL,TIME
14  FORMAT(2X,4HVOL=.F8,0,4X,5-TIME=.F8,0)
15  VAL(1)=Y(1)
      IF (ABS(Y(2)-YLAST).LT. .1) GO TO 20
      CALL CSHM1
      WRITE (16,94) Y(2),YLAST,TOT,TOT1,THEI,T2,T4
      WRITE (16,95) T,FL,F,VAPOUT(3)
      WRITE (16,96) VAPI(3)
      WRITE (16,97) IOFL
16  FORMAT (1H 5110)
17  FORMAT (1H 3612.5)
      IF (.NOT. SENS(2)) GO TO 20
      LA CURSOR
      STA ICUES
      WRITE (16,97) ICUES
      WRITE (16,95) ISTACK
      WRITE (16,96) STACK
18  FORMAT (1H 508)
19  FORMAT (1H 3612.5)
20  CALL CSM1
      YLAST=Y(2)
      VAL(2)=Y(2)
      VAL(3)=FEAT*0.66/(121.+T)/GV
      VAL(4)=Z(2)
      VAL(5)=Z(3)
      VAL(8)=Z(2)
      VAL(9)=Z(1)
      VAL(10)=-Z(5)
      VAL(11)=Z(5)
      VAL(12)=VAPOUT(2)/800.
      VAL(13)=66.6/T
      CALL CSHDCS(0,VAL,13,IEVF)
      GO TO 10
      END

```

```

[
RDEV.2

```

REFERENCES

1. Kilgore, R.A.; Goodyer, M.J.; Adcock, J.B.; and Davenport, E.E.: The Cryogenic Wind Tunnel Concept for High Reynolds Number Testing. NASA TN D-7762, Nov. 1974.
2. Proceedings of First International Symposium on Cryogenic Wind Tunnels. The University (Southampton, England), April 3-5, 1979.
3. Kilgore, R.A.: Design Features and Operational Characteristics of the 0.3-Meter Transonic Cryogenic Tunnel. NASA TN-D-8034, Dec. 1976.
4. Pope, A.; and Harper, J.J.: Low Speed Wind Tunnel Testing. John Wiley and Sons, 1966.
5. Jacobsen, R.T.: Thermophysical Properties of Nitrogen from 65 K to 2,000 K with Pressures up to 10,000 Atmospheres. NBS TN-648, 1977.
6. Adcock, J.B.; Kilgore, R.A.; and Ray, E.J.: Cryogenic Nitrogen as a Transonic Wind Tunnel Test Gas. AIAA paper No. 75-143, Jan. 1975.
7. Kilgore, R.A.; and Adcock, J.B.: Specific Cooling Capacity of Liquid Nitrogen. NASA TM X-74015, 1977.
8. Scurlock, R.G.: Low Temperature Behavior of Solids: An Introduction. Dover Publications.
9. Corrucini, R.J.; and Gniewek, J.J.: NBS Monograph 21, Oct. 3, 1960.
10. Bartz, D.R.: A Simple Equation for Rapid Estimation of Rocket Nozzle Convective Heat Transfer Coefficients. Jet Propulsion, pp. 49-51, Jan. 1957.
11. Rao, D.M.: Wind Tunnel Design Studies and Technical Evaluation of Advanced Cargo Aircraft Concepts. NASA Final Report for Grant NSG 1135, May 1976.
12. Shapiro, A.H.: The Dynamics and Thermodynamics of Compressible Fluid Flow. Vols. I and II. The Royal Press Co., 1954.
13. Composition of Aluminums. Cryogenic Engineering News, 1969.
14. Ray, E.J.; Ladson, C.L.; Adcock, J.B.; Lawing, P.L.; Hall, R.M.: Review of Design and Operational Characteristics of 0.3-Meter Transonic Cryogenic Tunnel. NASA-TM-80123, Sept. 1979.

Table 1. 0.3-m TCT area distribution.

| DISTANCE, x (m) | AREA, A(x) (m ²) | DISTANCE, x (m) | AREA, A(x) (m ²) |
|--------------------------------|---------------------------------|---------------------------------|---------------------------------|
| 0 | 0.254 | 12.440 | 0.267 |
| 0.635 | 0.282 | 12.540 | 0.2192 |
| 1.245 | 0.357 | 12.640 | 0.184 |
| 1.854 | 0.437 | 12.750 | 0.158 |
| 2.641 | 0.516 | 12.85 | 0.138 |
| 3.251 | 0.566 | 12.950 | 0.129 |
| 4.470 | 0.816 | 13.050 | 0.1250 |
| 5.690 | 1.006 | 13.220 | 0.1235 |
| | | - TEST SECTION - | |
| 6.299 | 1.108 | 14.14 | 0.1250 |
| 6.908 ← GN ₂ flow → | 1.168 | 14.25 | 0.130 |
| 8.485 | 1.168 | 14.52 | 0.145 |
| 9.956 | 1.168 | 14.65 | 0.152 |
| 11.328 | 1.162 | 15.19 | 0.189 |
| 11.430 | 1.149 | 15.64 | 0.210 |
| 11.530 | 1.112 | 15.850 ← LN ₂ flow → | 0.240 |
| 11.630 | 1.042 | 16.307 | 0.284 |
| 11.730 | 0.948 | 16.764 | 0.330 |
| 11.830 | 0.833 | 17.221 | 0.379 |
| 11.930 | 0.719 | 17.678 | 0.4338 |
| 12.030 | 0.597 | 18.135 | 0.4552 |
| 12.140 | 0.496 | 19.354 | 0.455 |
| 12.240 | 0.404 | 20.570 | 0.394 |
| 12.340 | 0.328 | 21.285 | 0.253 |
| | | {Fan} | |
| | | 21.540 | 0.252 |

Table 2. 0.3-m TCT circuit loss pattern.

| DISTANCE | CIRCUIT LOSS FACTOR |
|----------|-------------------------------------|
| (m) | $\sum k_1 = \frac{\Delta P_s}{P_s}$ |
| 0.00 | 0.00 |
| 0.521 | 0.004 |
| 1.435 | 0.008 |
| 2.438 | 0.0120 |
| 4.779 | 0.0140 |
| 7.214 | 0.0160 |
| 8.759 | 0.0180 |
| 11.061 | 0.0190 |
| 13.075 | 0.020 |
| 14.630 | 0.109 |
| 16.581 | 0.121 |
| 13.105 | 0.133 |
| 19.627 | 0.153 |
| 20.080 | 0.169 |
| 21.305 | 0.186 |
| 21.701 | 0.197 |

$$\text{Pressure ratio } r = 1 + M^2 \left[\sum k_1 \left(1 - \frac{7}{T} \frac{PM}{T} \right) \right]$$

M = Test section Mach number

Table 3. Tunnel and simulator test conditions.

| Fig. No. | Total Temperature (K) | Test Section (Mach Number) | Total Pressure (atm) |
|-------------|--------------------------|-------------------------------|-------------------------|
| 38 | 100 | 0.3 | 1.57 |
| 39 | 100 | 0.6 | 1.57 |
| 40 | 100 | 0.9 | 1.57 |
| 41 | 100 | 0.3 | 3.00 |
| 42 | 100 | 0.6 | 3.00 |
| 43 | 100 | 0.95 | 3.07 |
| 44 | 100 | 0.3 | 5.00 |
| 45 | 100 | 0.6 | 5.00 |
| 46 | 100 | 0.9 | 4.93 |
| 47 | 200 | 0.3 | 1.57 |
| 48 | 200 | 0.6 | 1.50 |
| 49 | 200 | 0.9 | 1.57 |
| 50 | 200 | 0.3 | 2.65 |
| 51 | 200 | 0.6 | 3.00 |
| 52 | 200 | 0.9 | 3.00 |
| 53 | 200 | 0.3 | 5.00 |
| 54 | 200 | 0.6 | 5.00 |
| 55 | 200 | 0.9 | 5.00 |
| 56 | 275 | 0.3 | 1.57 |
| 57 | 275 | 0.6 | 1.57 |
| 58 | 275 | 0.75 | 1.57 |
| 59 | 275 | 0.3 | 3.00 |
| 60 | 274 | 0.6 | 3.00 |
| 61 | 275 | 0.75 | 3.00 |
| 62 | 275 | 0.3 | 5.00 |
| 63 | 275 | 0.6 | 5.00 |
| 64 | 275 | 0.8 | 5.00 |

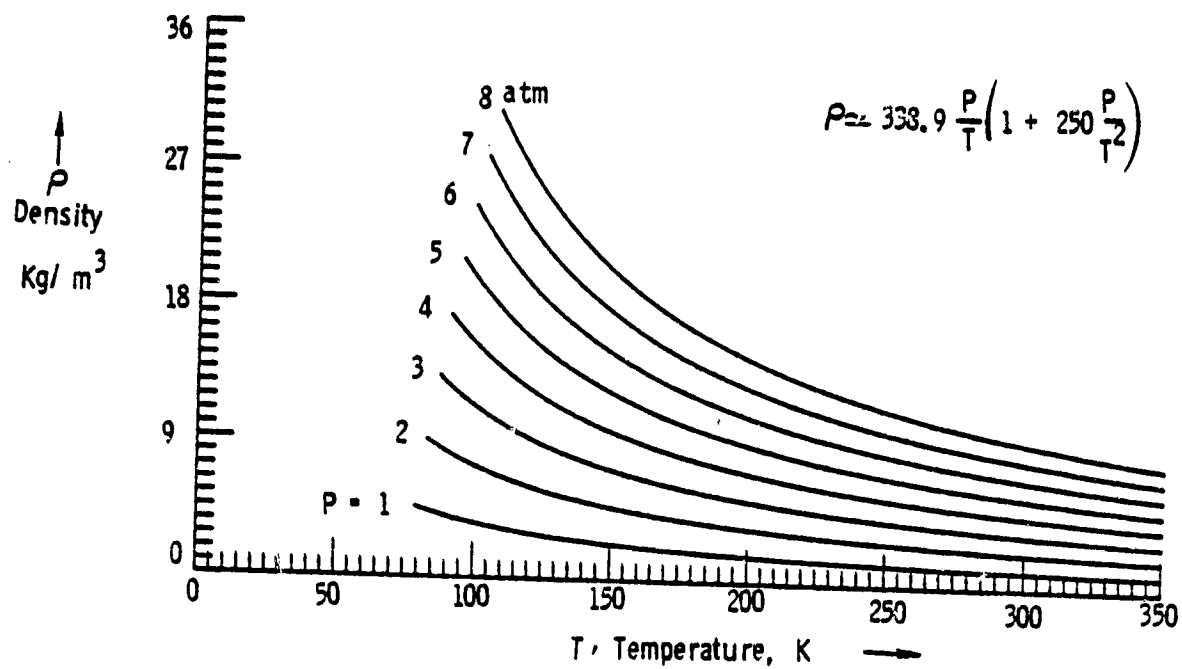


Figure 1. Density of nitrogen gas.

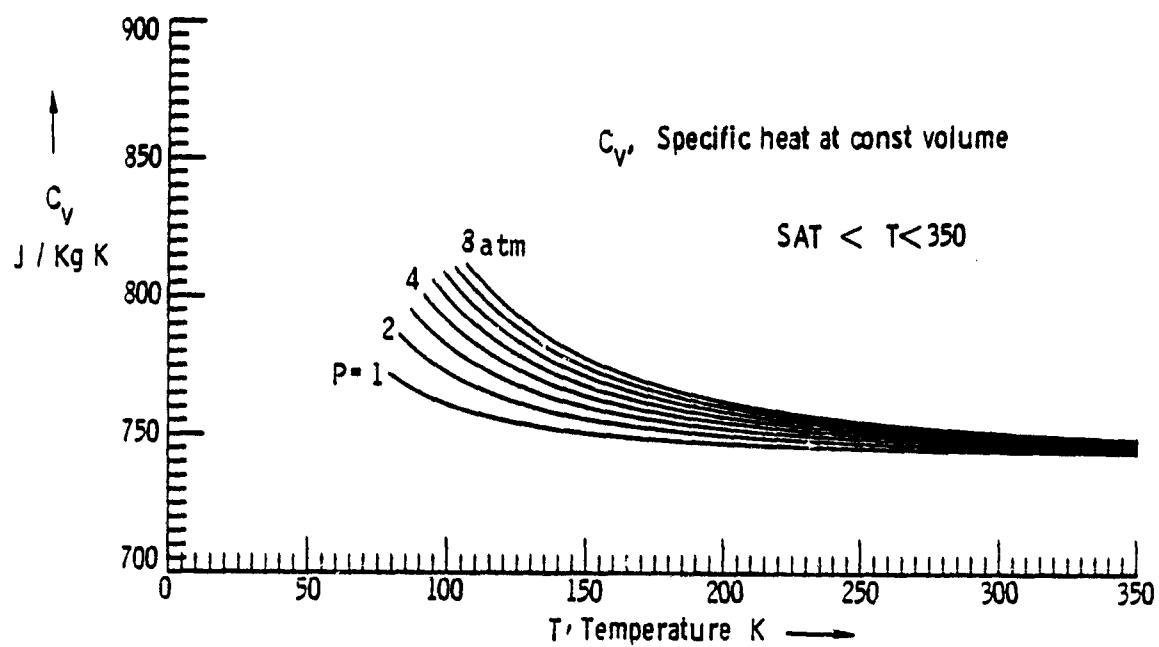


Figure 2. Specific heat of nitrogen gas.

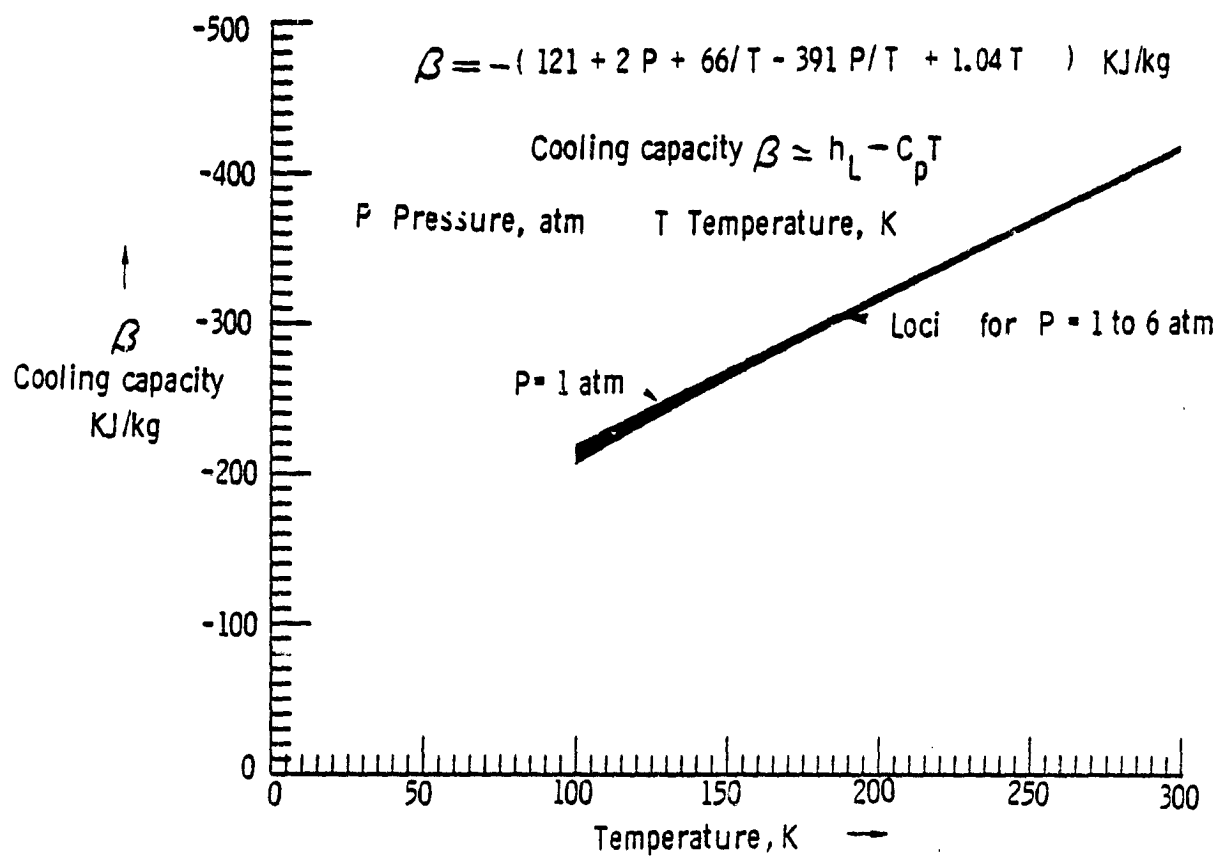


Figure 3. Cooling capacity of liquid nitrogen.

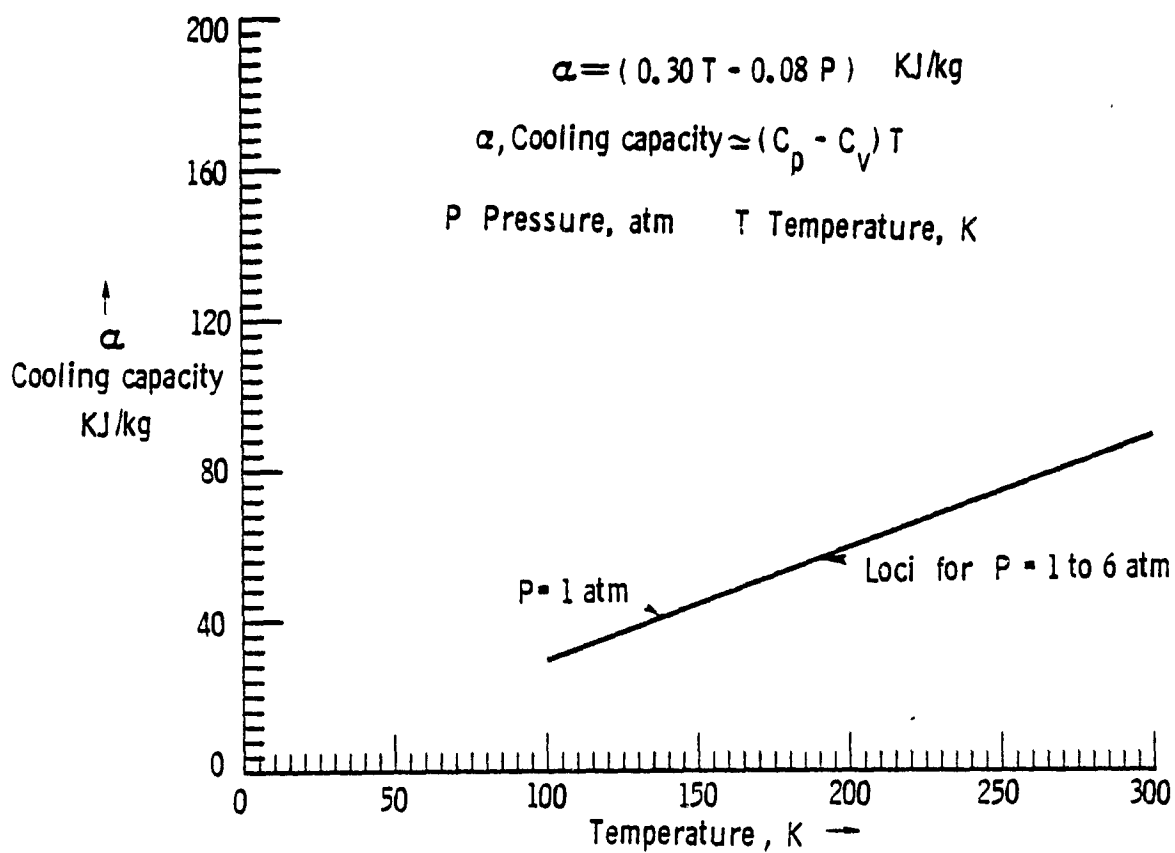


Figure 4. Cooling capacity of gaseous bleed.

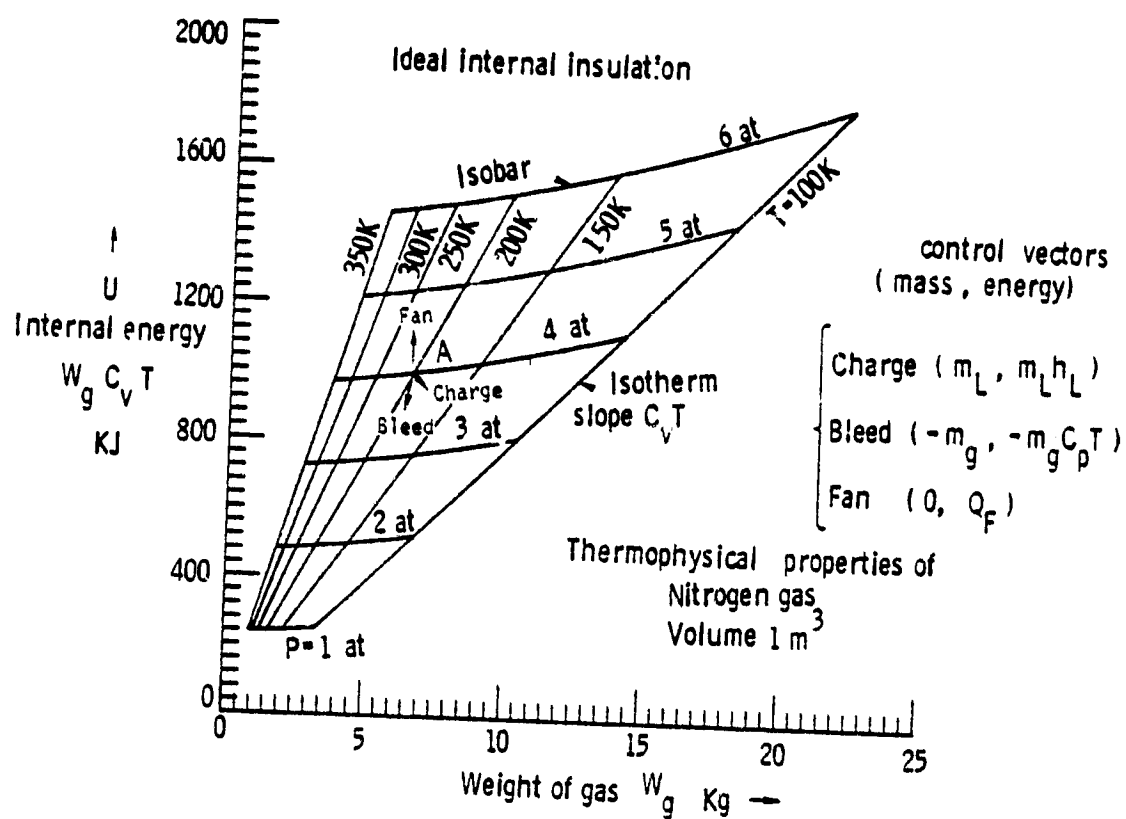
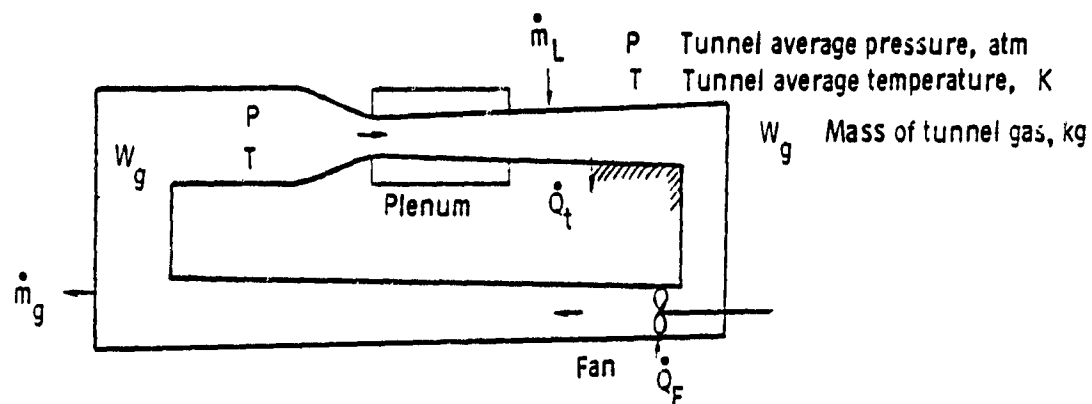


Figure 5. Energy state diagram.



Assumptions

- Perfect gas behavior
- Uniform tunnel temperature
- Work, potential & kinetic energy ignored

first law of thermodynamics
$$-\dot{Q}_t + \dot{Q}_F + \dot{m}_L h_L - \dot{m}_g h_g = W_g C_v \frac{dT}{dt} + u(\dot{m}_L - \dot{m}_g)$$

Where

| | |
|--|--|
| h_L Liquid nitrogen enthalpy J/kg | \dot{Q}_F Heat flow from Fan operation J/sec |
| u Specific internal energy | \dot{m}_g Gaseous nitrogen bleed kg/sec |
| h_g Gas enthalpy J/kg | \dot{m}_L Liquid nitrogen mass flow kg/sec |
| \dot{Q}_t Heat flow to tunnel metal wall J/sec | |

Figure 6. Thermodynamic model of a closed circuit cryogenic tunnel.

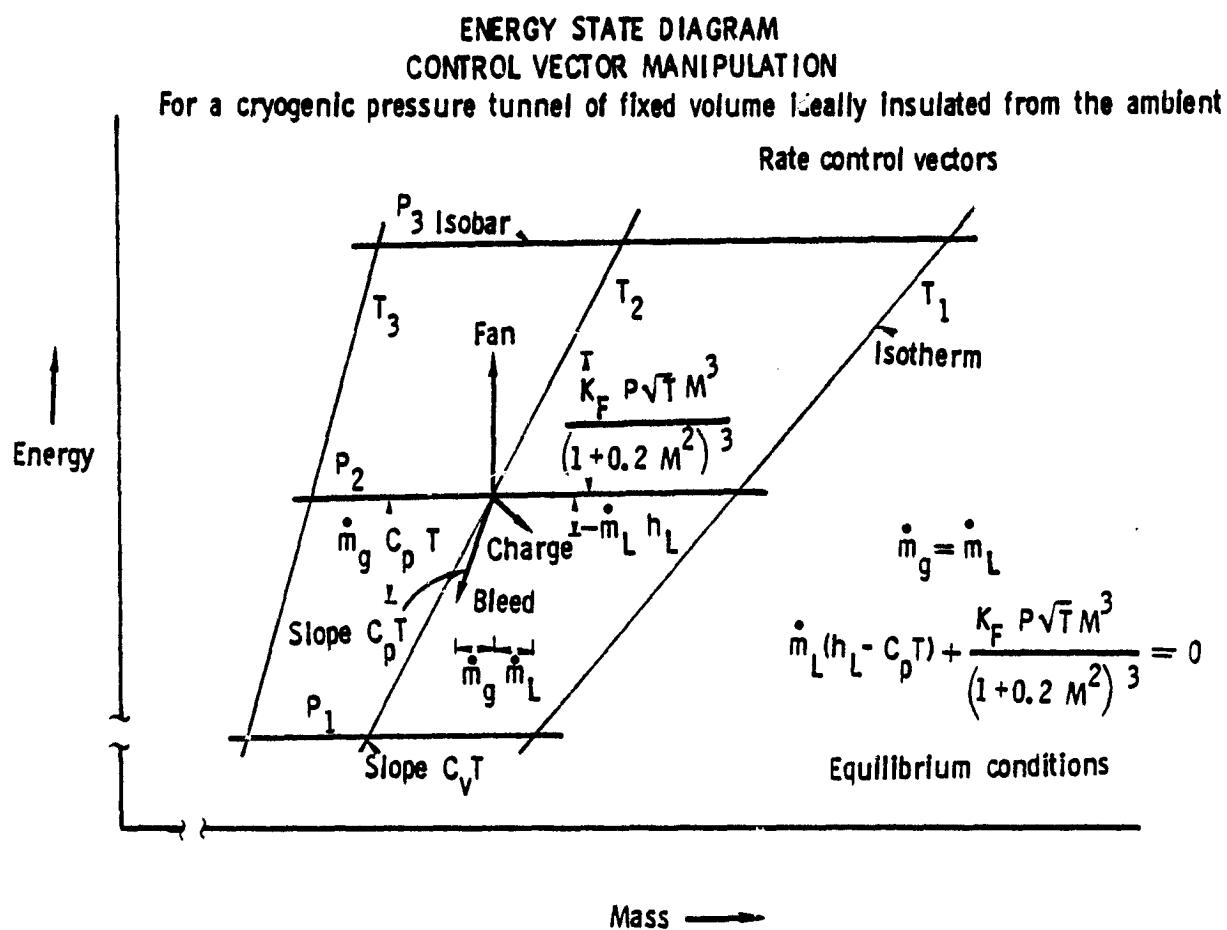


Figure 7. Tunnel state manipulation, equilibrium.

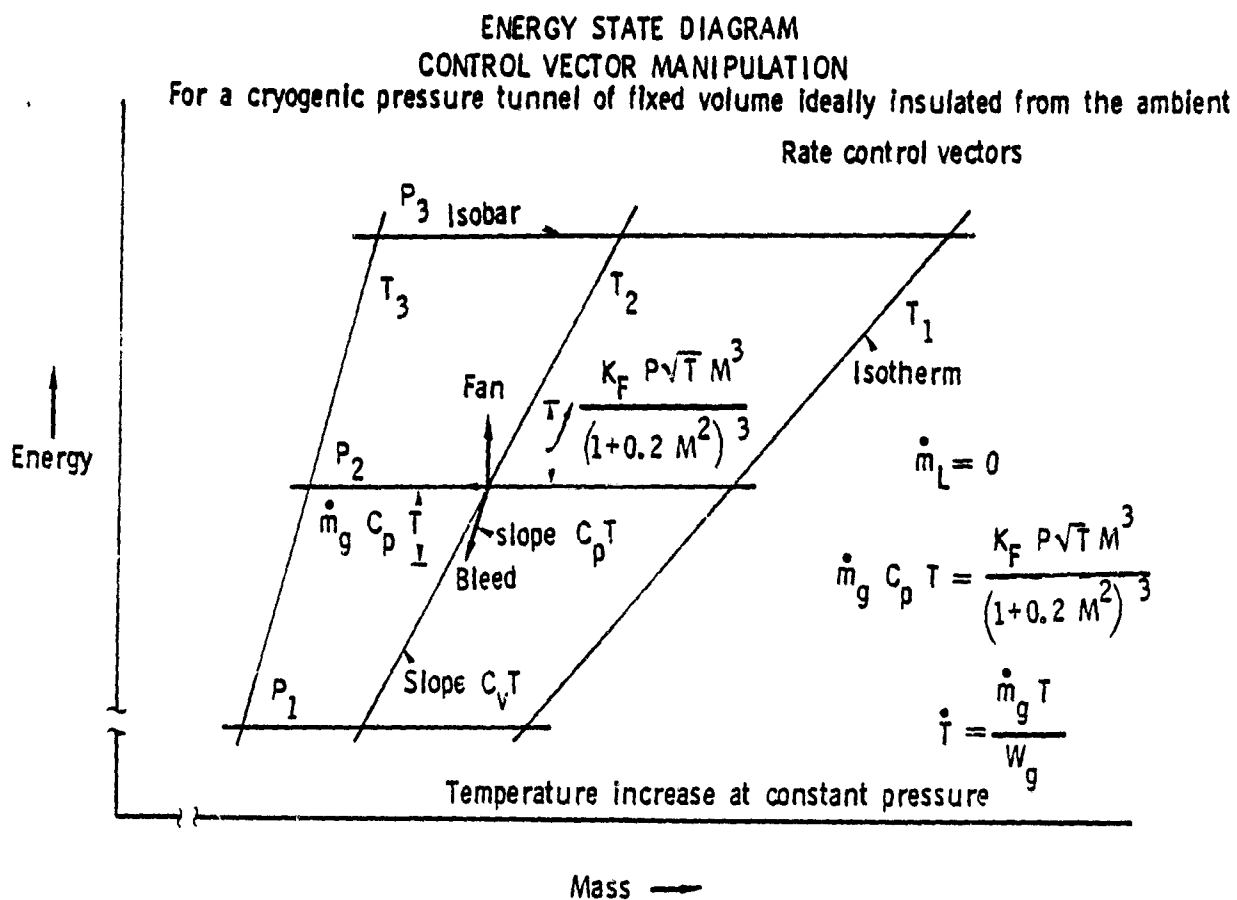


Figure 8. Tunnel state manipulation, temperature rise at constant pressure.

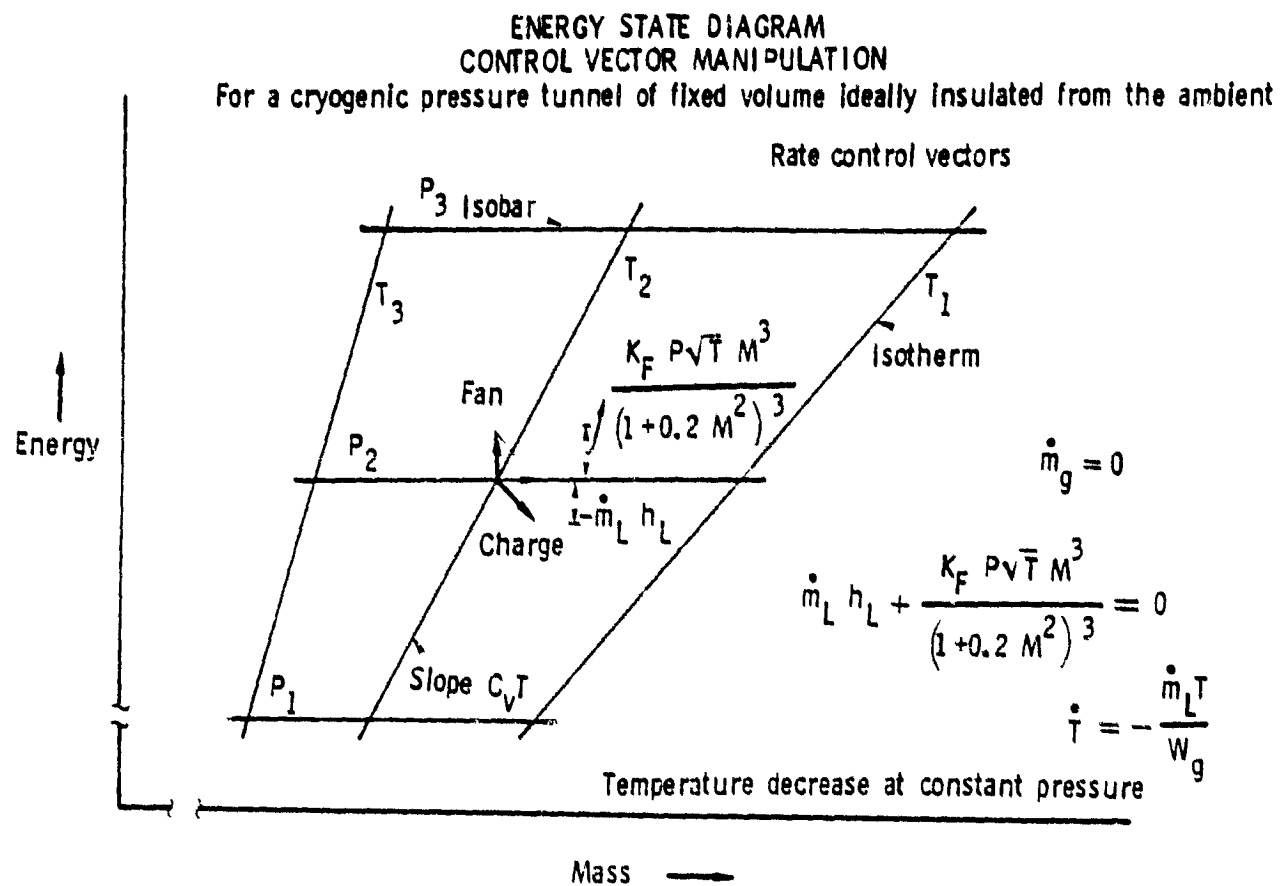


Figure 9. Tunnel state manipulation, temperature drop at constant pressure.

ENERGY STATE DIAGRAM CONTROL VECTOR MANIPULATION

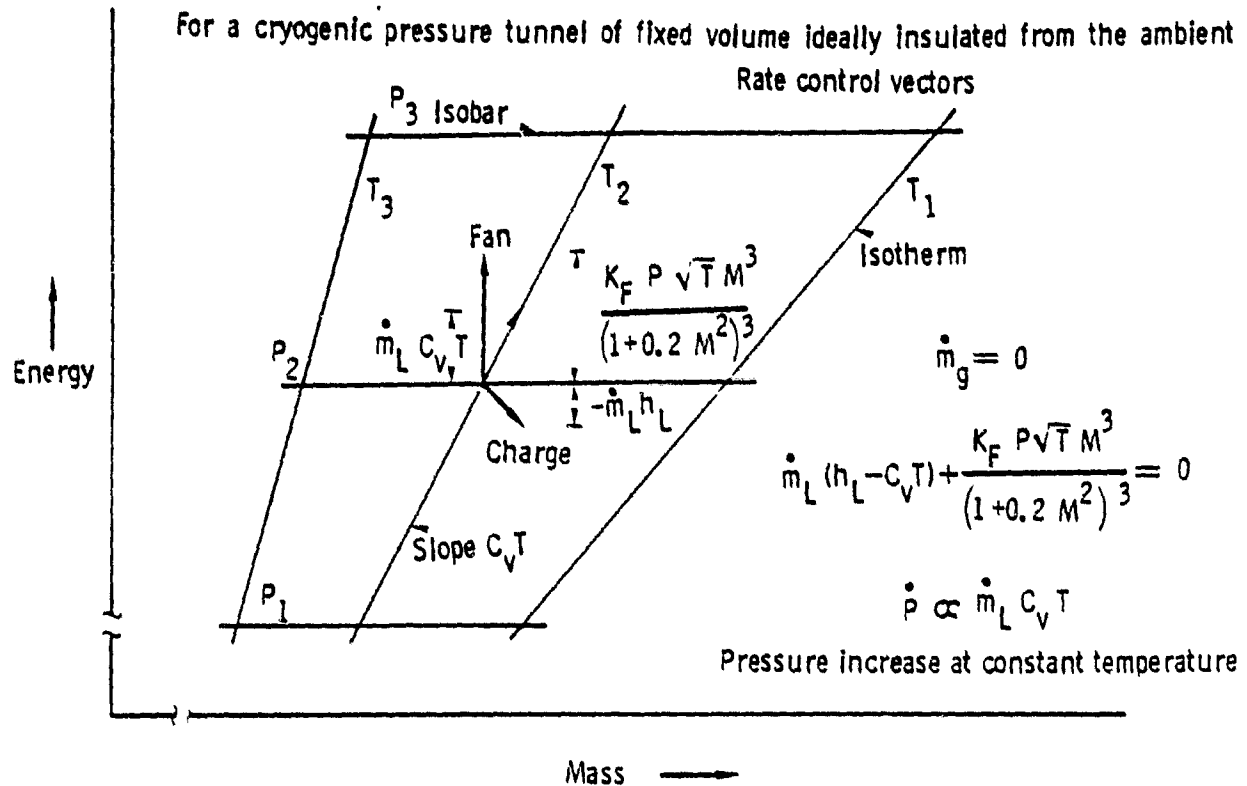


Figure 10. Tunnel state manipulation, pressure rise at constant temperature.

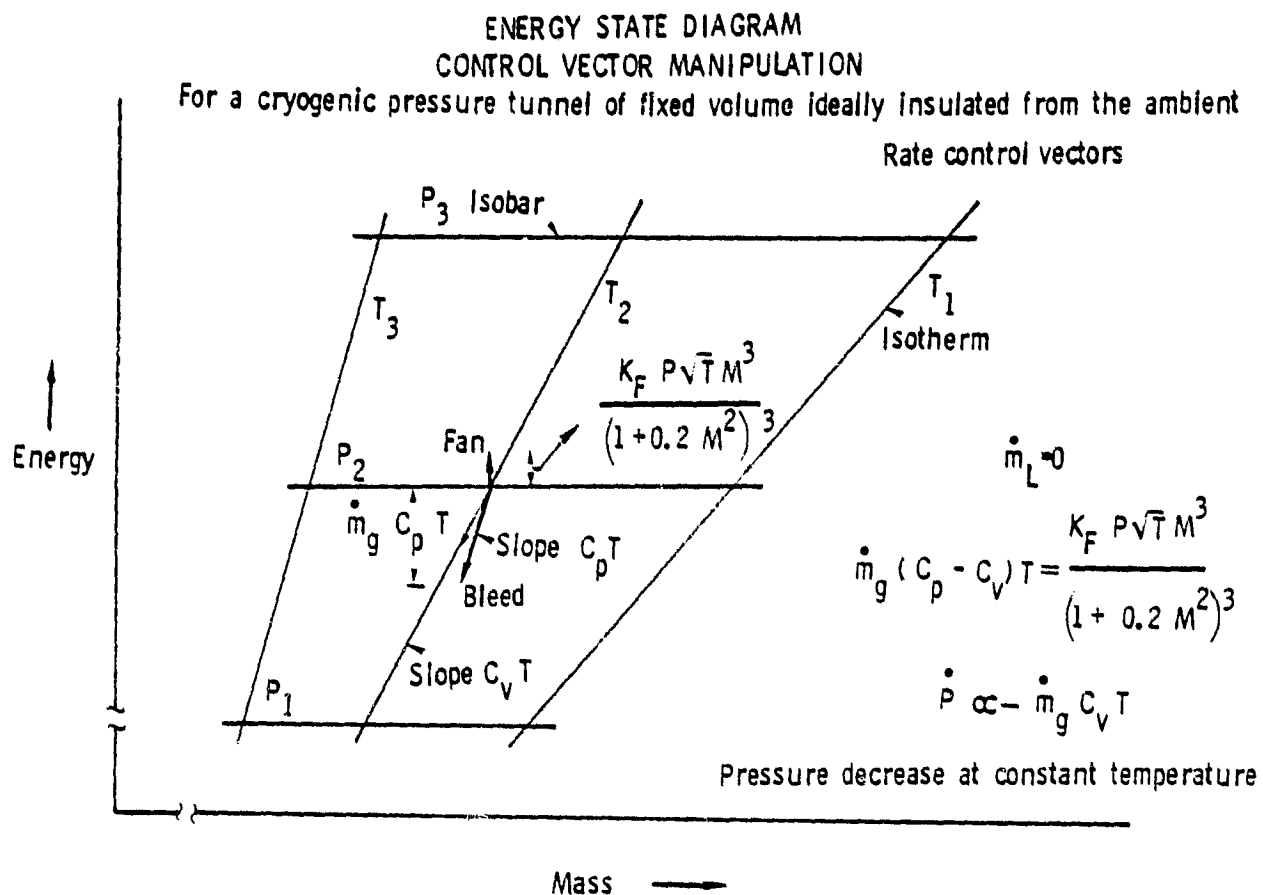


Figure 11. Tunnel state manipulation, pressure drop at constant temperature.

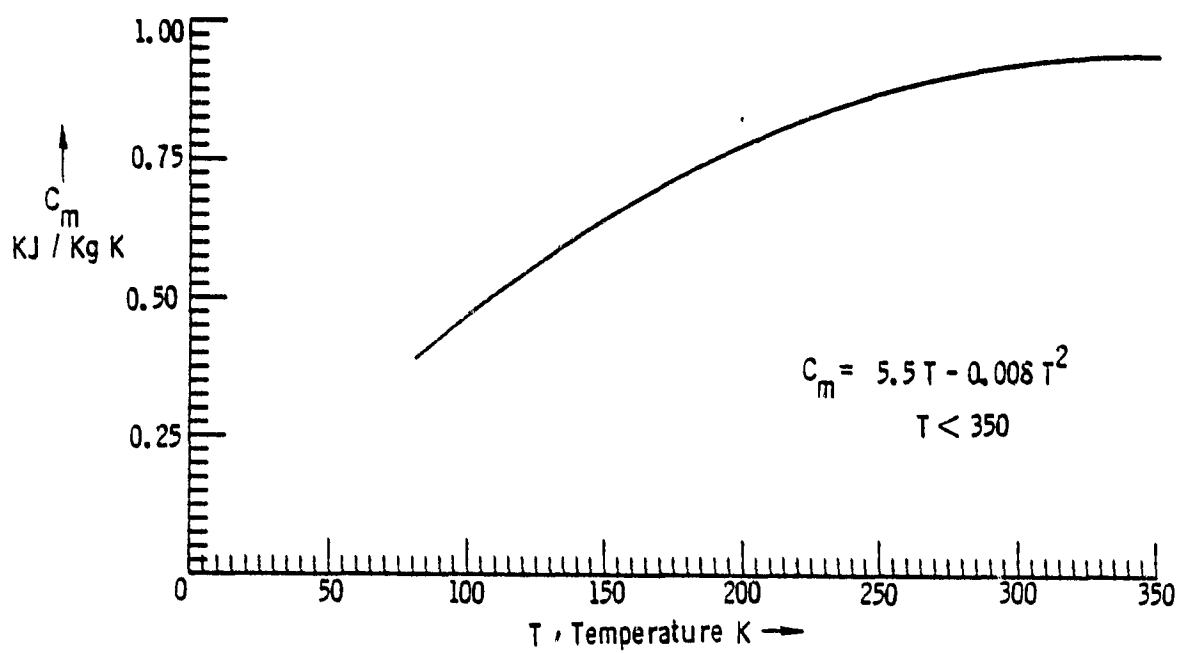


Figure 12. Specific heat of aluminum alloy 6061-T6.

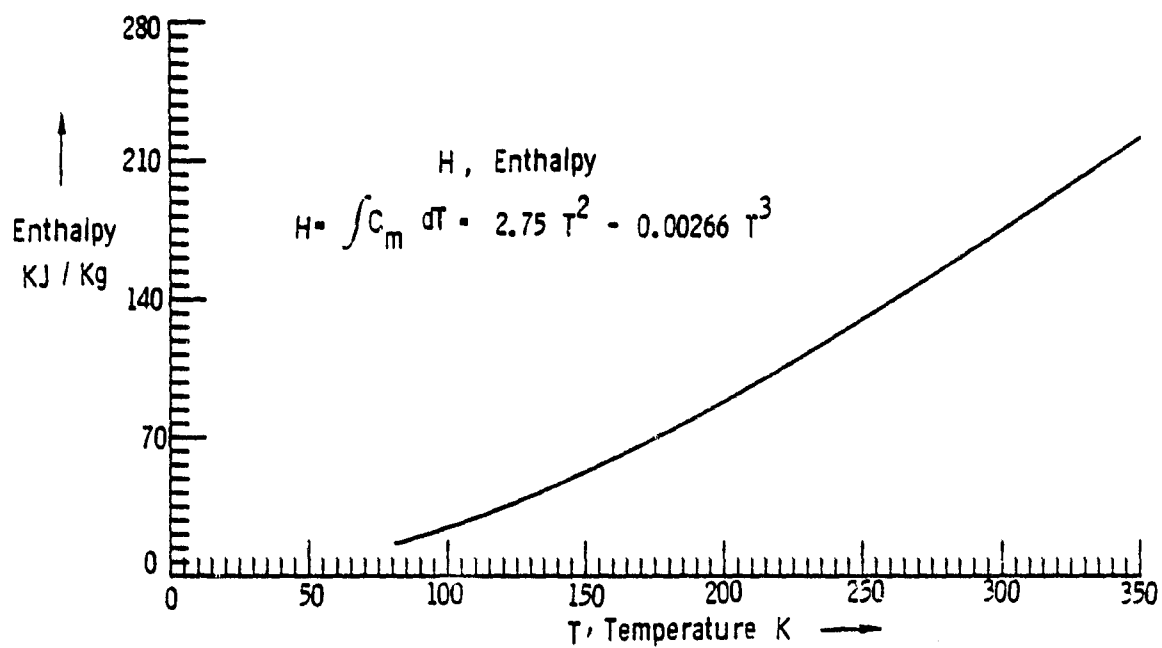


Figure 13. Enthalpy of aluminum alloy 6061-T6.

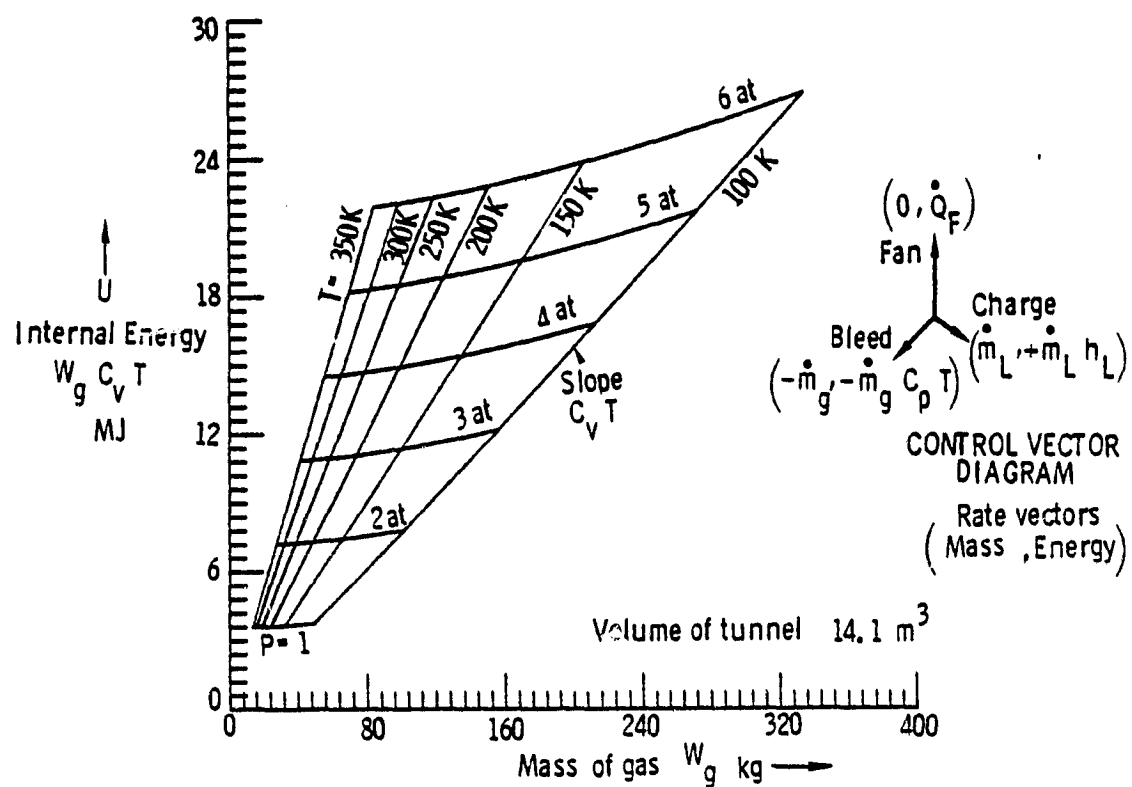


Figure 14. 0.3-m cryogenic tunnel energy state diagram, ideal internal insulation.

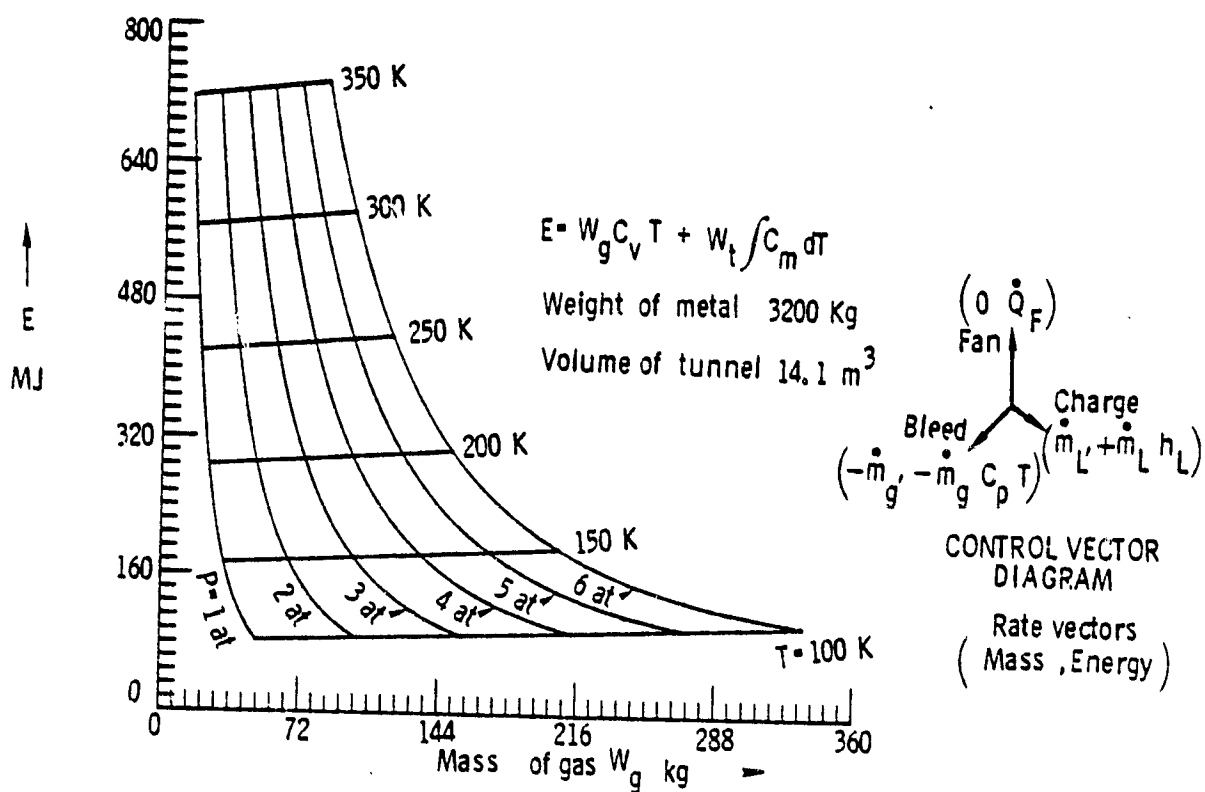


Figure 15. 0.3-m cryogenic tunnel energy state diagram, ideal external insulation.

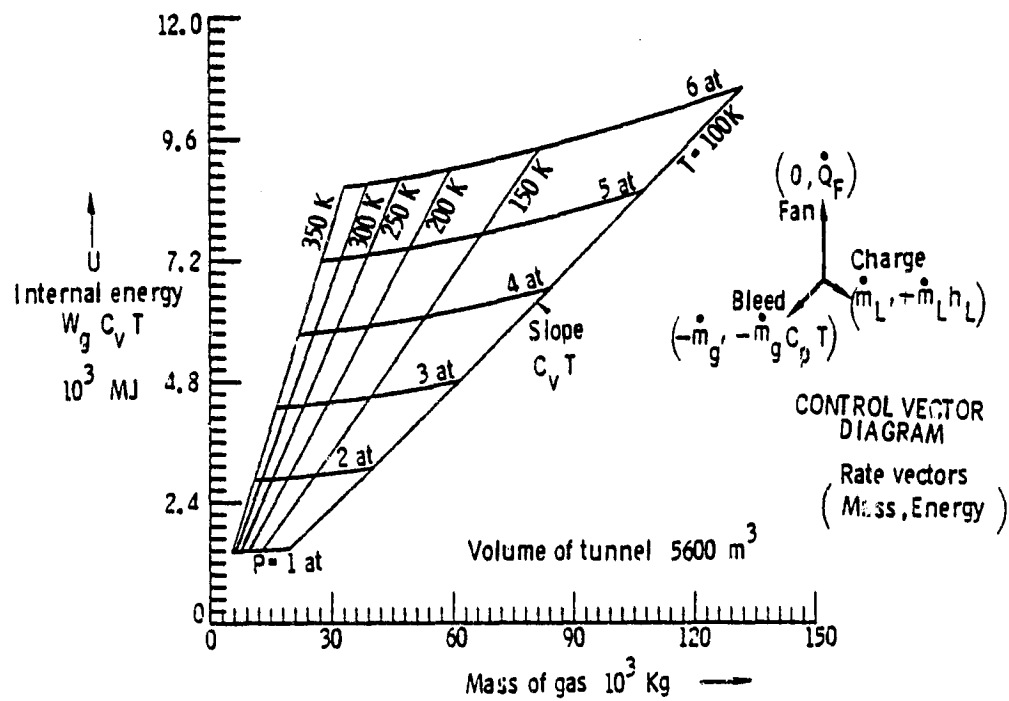


Figure 16. NTF energy state diagram, ideal internal insulation.

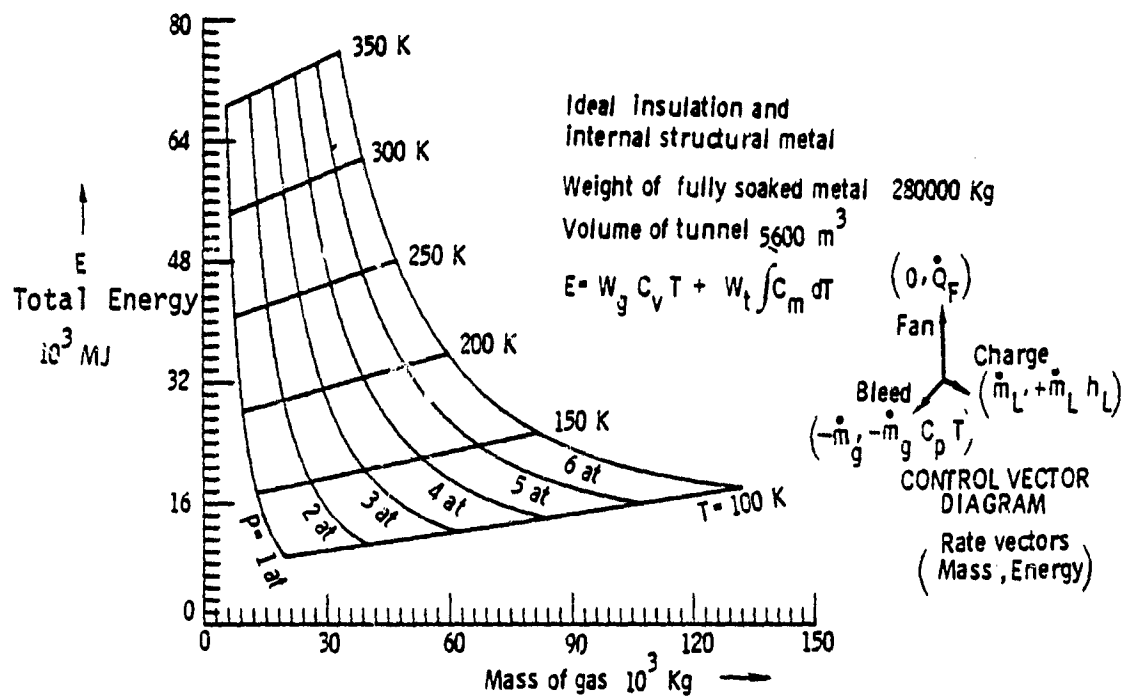
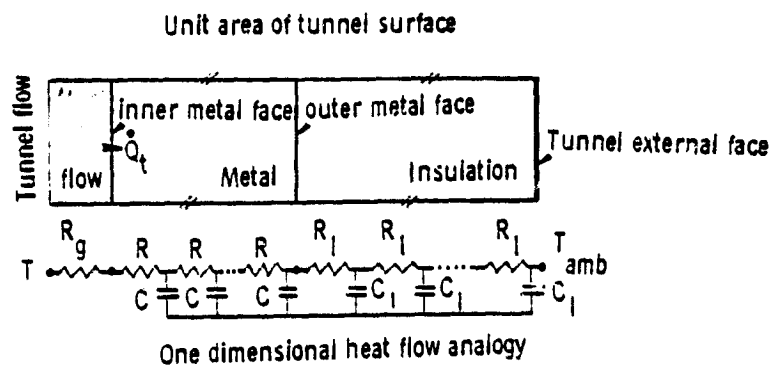


Figure 17. NTF energy state diagram, ideal insulation with structural metal.



$C_m = \Sigma C$ Thermal capacity of metal wall $J/m^2 K$
 $1/R_m = 1/\Sigma R$ Thermal conductivity of metal wall $J/m^2 K \text{ sec}$
 $1/R_g = y_g$ Turbulent boundary layer heat transfer coefficient $J/m^2 K \text{ sec}$
 $1/R_i$ Thermal conductivity of one layer of insulation $J/m^2 K \text{ sec}$
 C_i Thermal capacity of one layer of insulation $J/m^2 K$
 T Average tunnel gas temperature T_{amb} Ambient temperature

Heat flow model

$$\dot{Q}_t = \frac{T - T_{amb}}{Z}$$

Z = Thermal impedance of the unit wall

Figure 18. Metal-to-gas heat transfer mechanism.

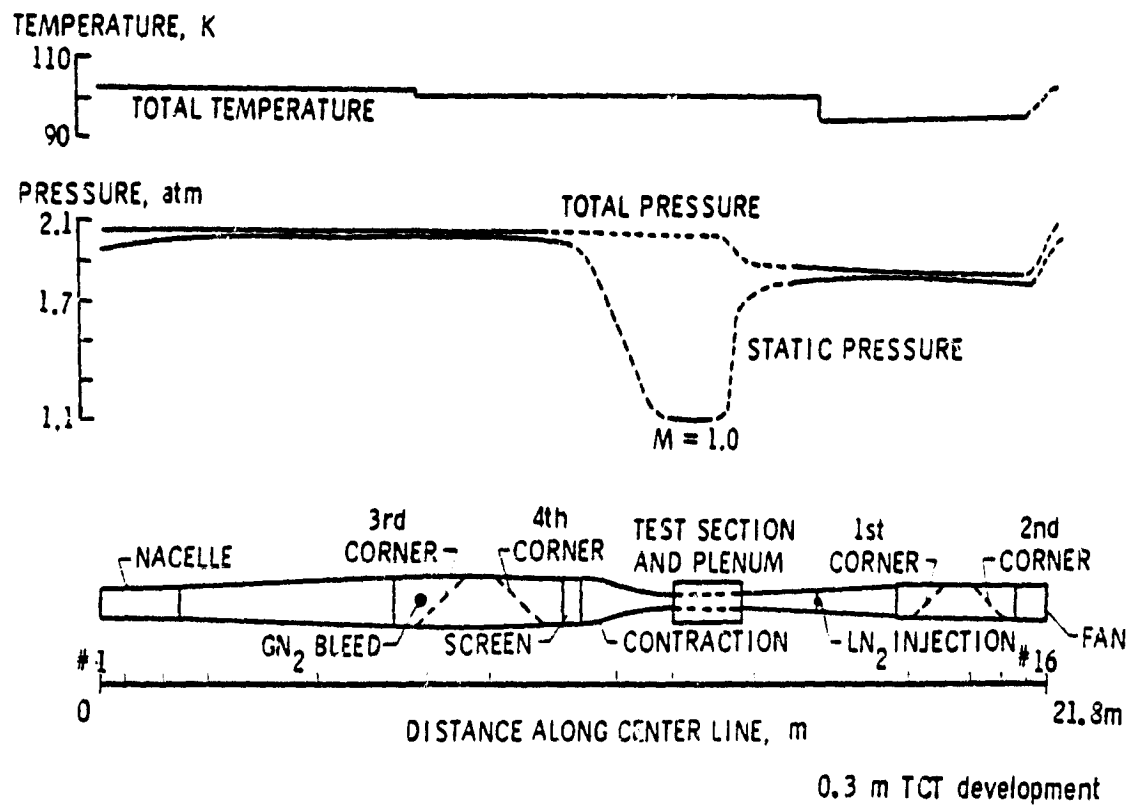


Figure 19. Spatial profile of total temperature and pressure.

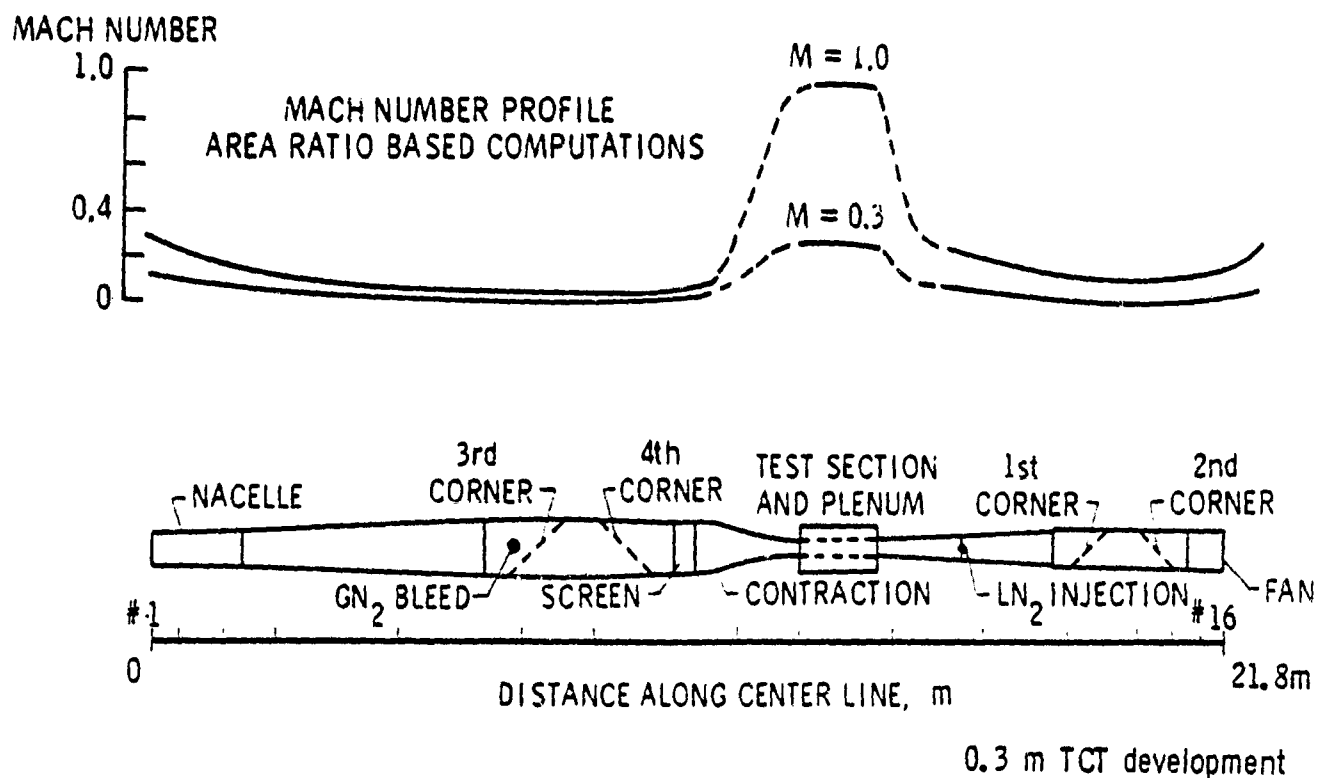


Figure 20. Spatial profile of tunnel flow Mach number.

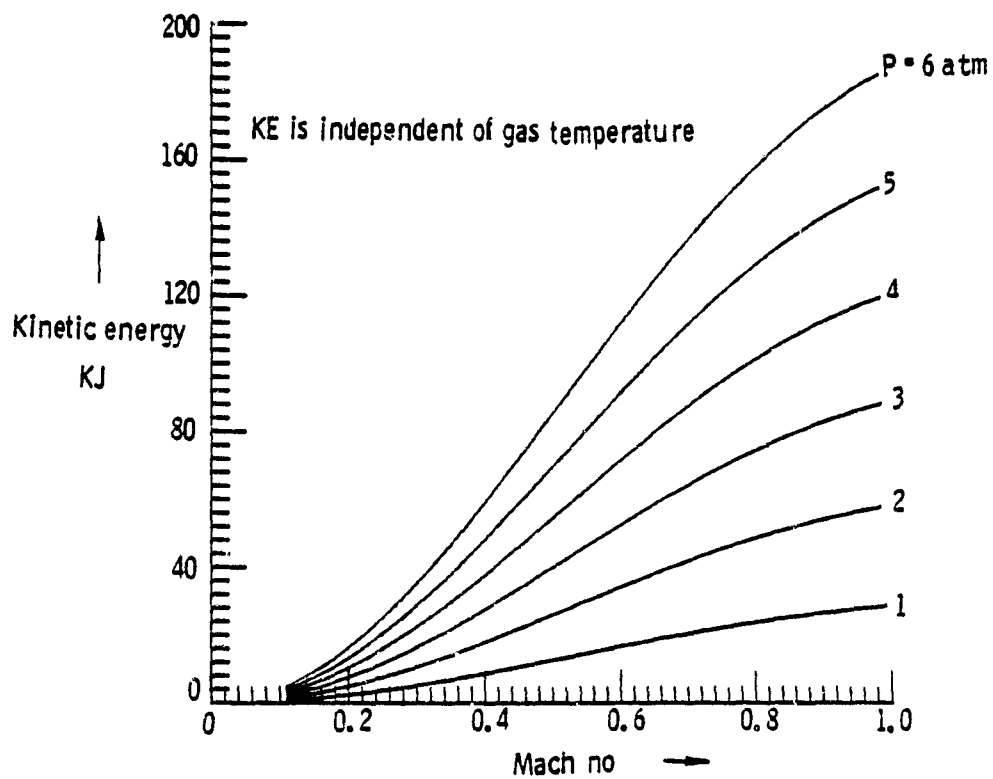


Figure 21. Kinetic energy of moving gas, 0.3-m TCT.

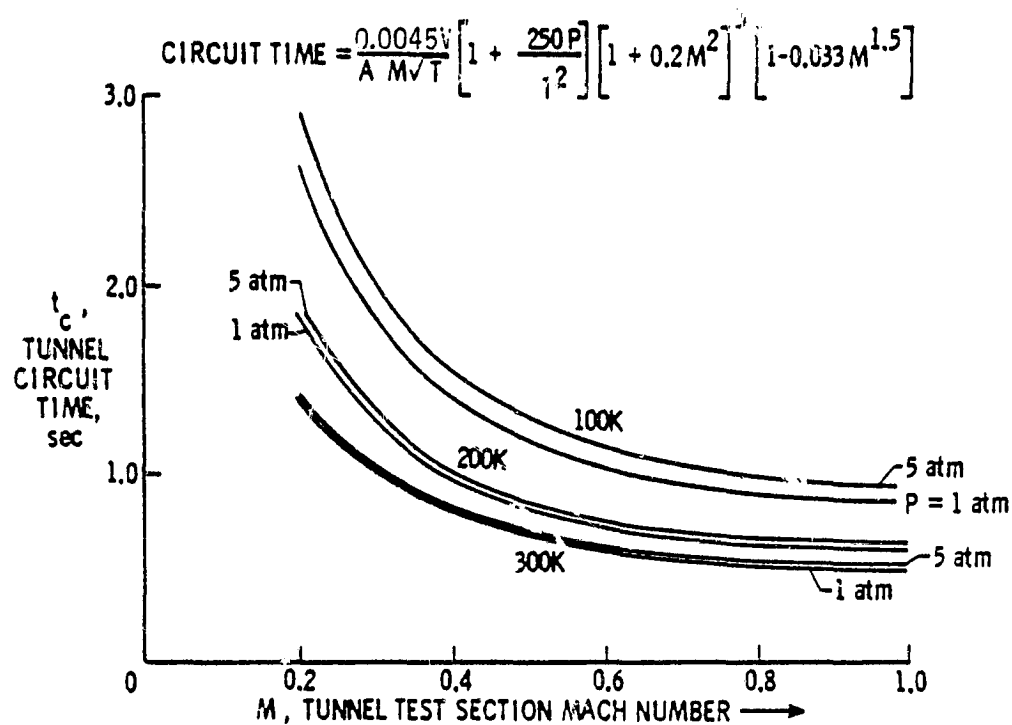


Figure 22. Tunnel circuit time, 0.3-m TCT.

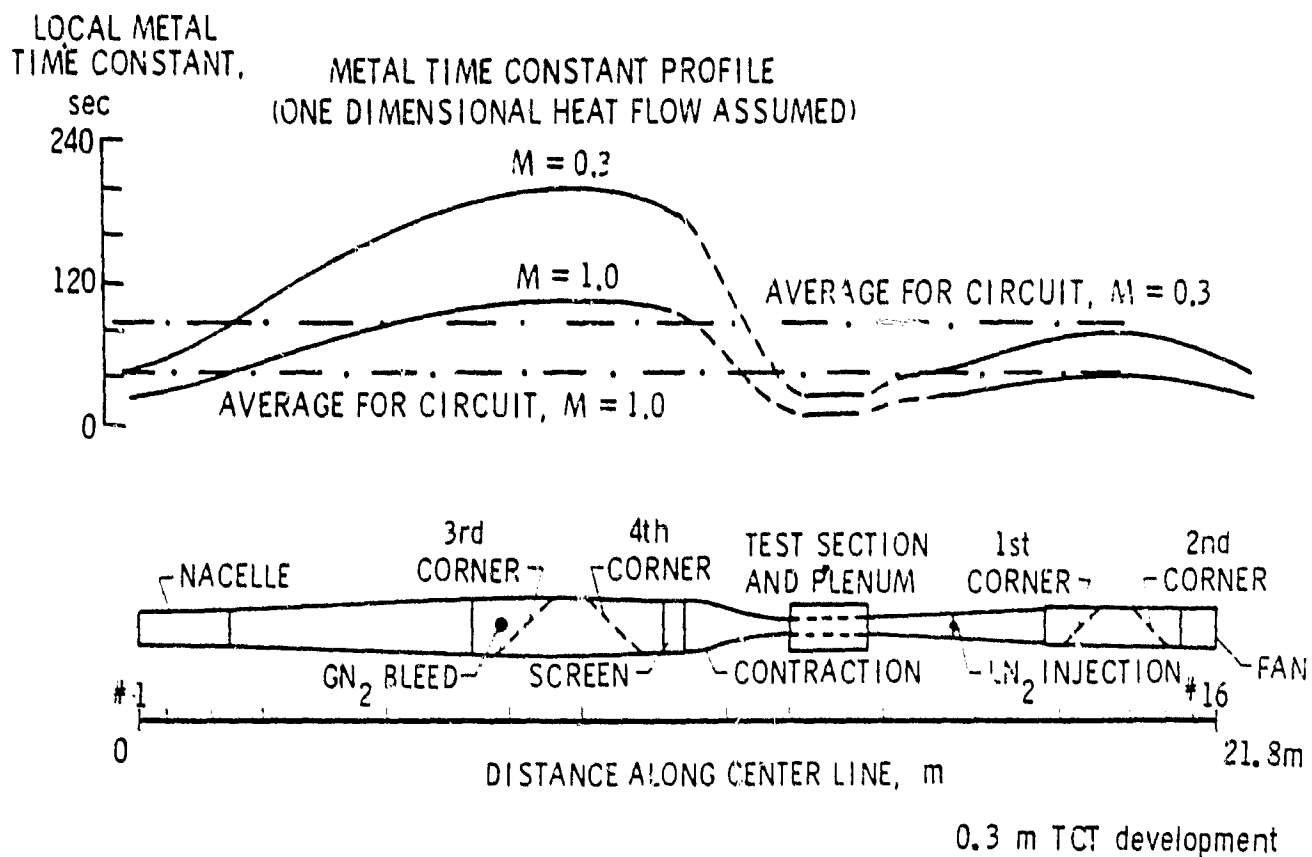


Figure 23. Spatial profile of local metal time constant.

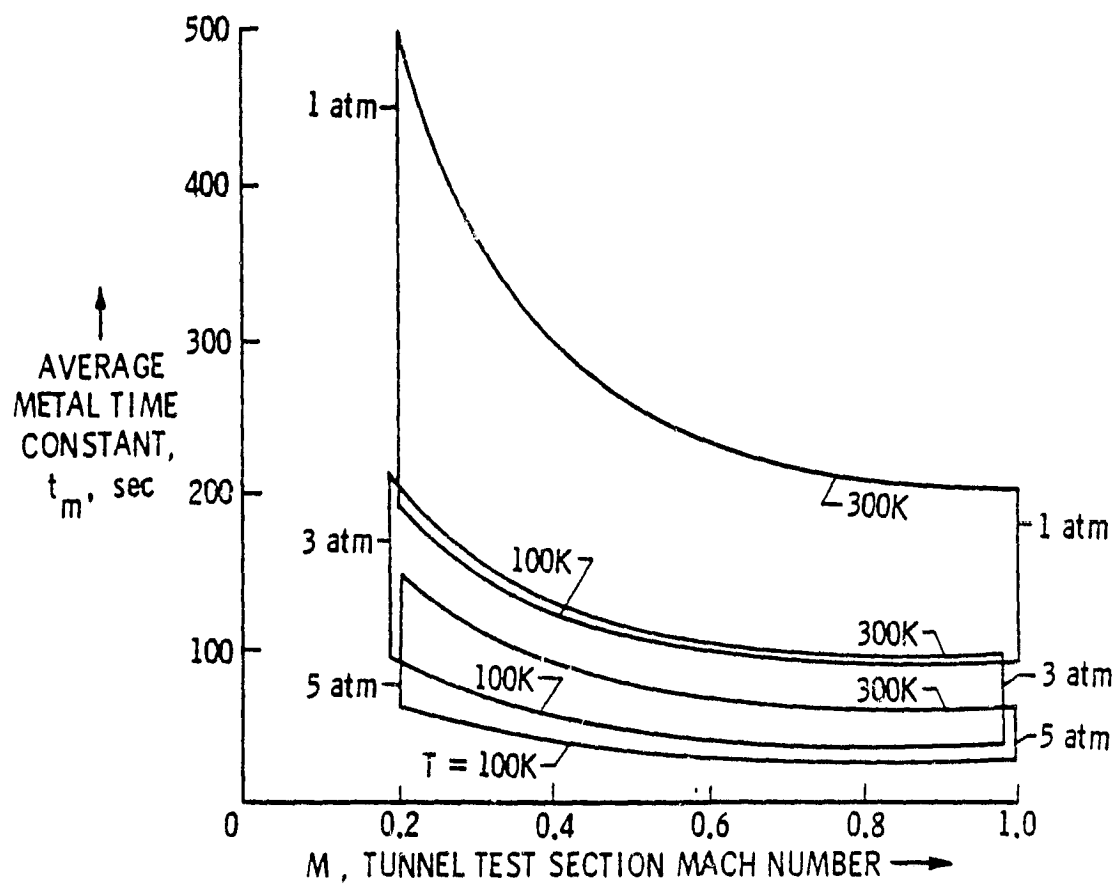


Figure 24. Average metal time constant.

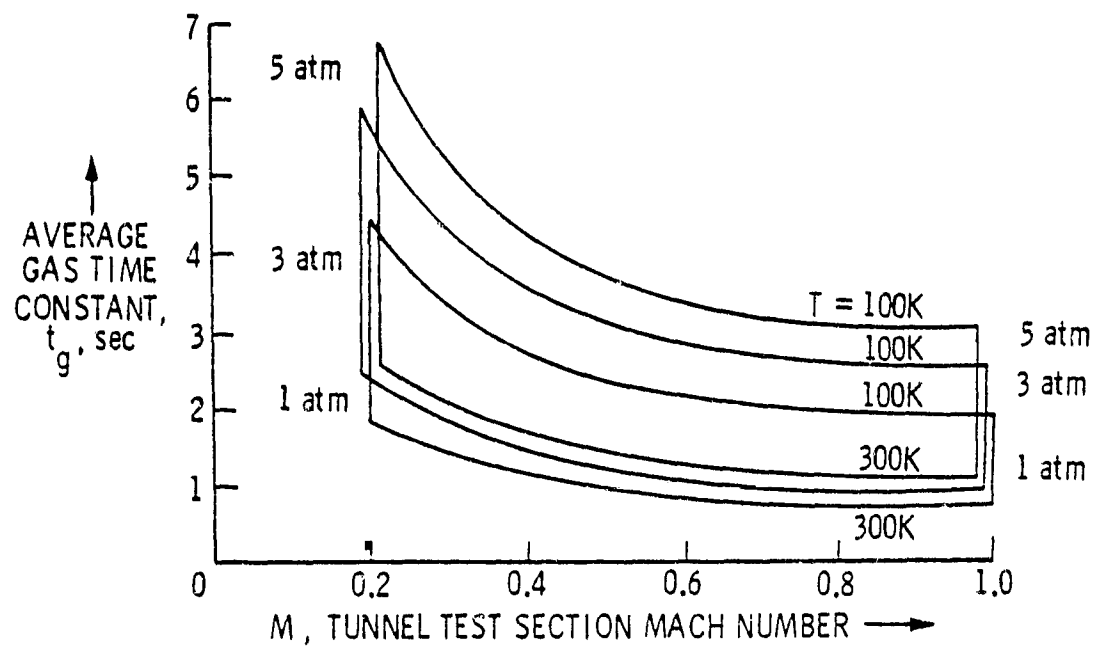


Figure 25. Average gas time constant.

TUNNEL PROCESS MODEL

$$\begin{bmatrix} \dot{O} \\ \dot{T} \\ \dot{M} \\ \dot{V} \\ \dot{P} \end{bmatrix} = \begin{bmatrix} k_L \cdot \frac{p \cdot a}{\theta} \cdot \frac{1 + i_m s}{1 + i_g s} e^{-\tau_L s} & \frac{k_I}{k_m} \cdot \frac{p M^2}{\theta(1 + 0.2M^2)} \cdot \frac{1 + i_m s}{1 + i_g s} e^{-\tau_I s} & -k_g \frac{p a}{\sqrt{T} \theta} \cdot \frac{1 + i_m s}{1 + i_g s} \\ 0 & \frac{e^{-\tau_d s}}{k_m \sqrt{T} \theta + i_g s} & 0 \\ k_L \left[\frac{p}{W} + \frac{p/B + a}{\tau \theta} \cdot \frac{1 + i_m s}{1 + i_g s} \right] & \left[\frac{k_I}{k_m} \cdot \frac{p^2 M^2}{T \theta(1 + 0.2M^2)} \cdot \frac{1 + i_m s}{1 + i_g s} + \frac{\partial M P s}{k_m \sqrt{T}} \right] & -\frac{k_g p}{\sqrt{T}} \left[\frac{p}{W} + \frac{p a}{\tau \theta} \cdot \frac{1 + i_m s}{1 + i_g s} \right] \end{bmatrix} \begin{bmatrix} A_L \\ V \\ A_g \end{bmatrix}$$

Figure 26. Lumped multivariable model of a cryogenic tunnel.

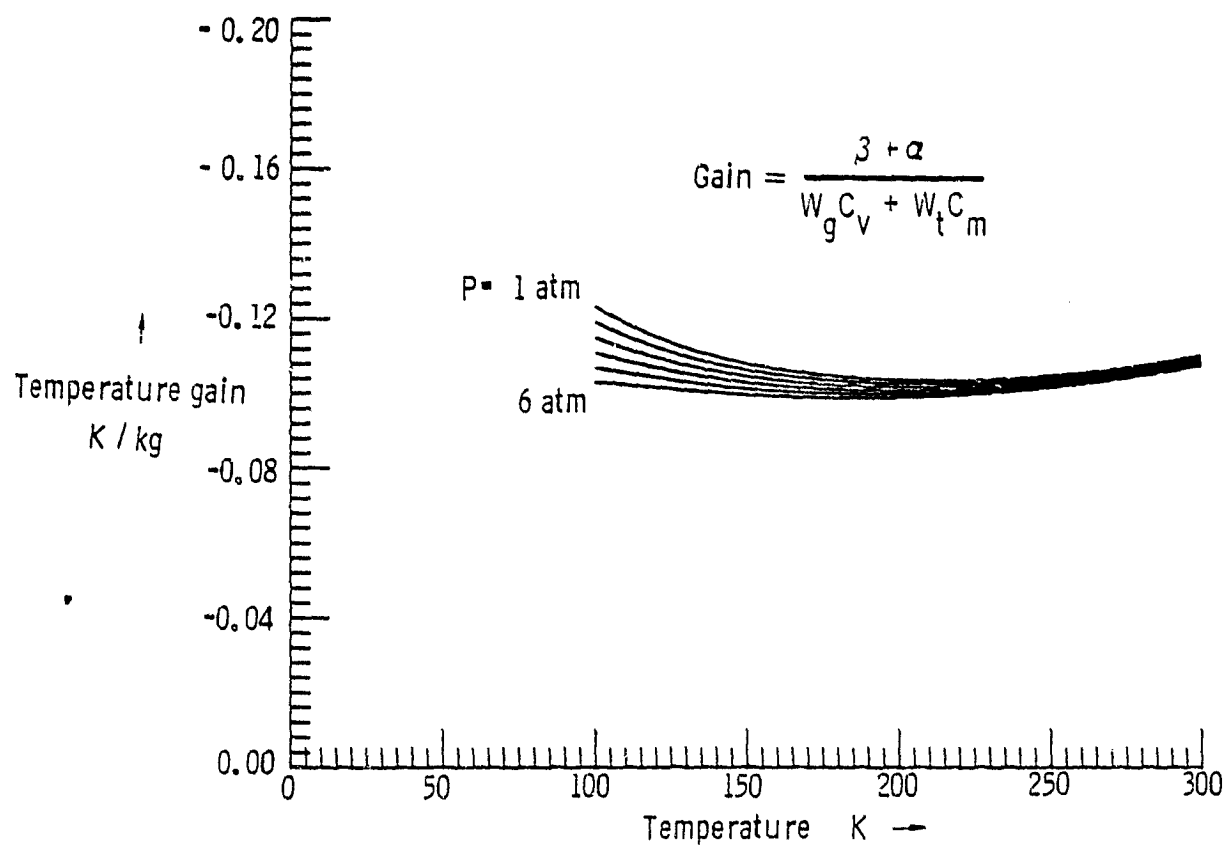


Figure 27. Steady-state tunnel temperature gain for LN_2 input.

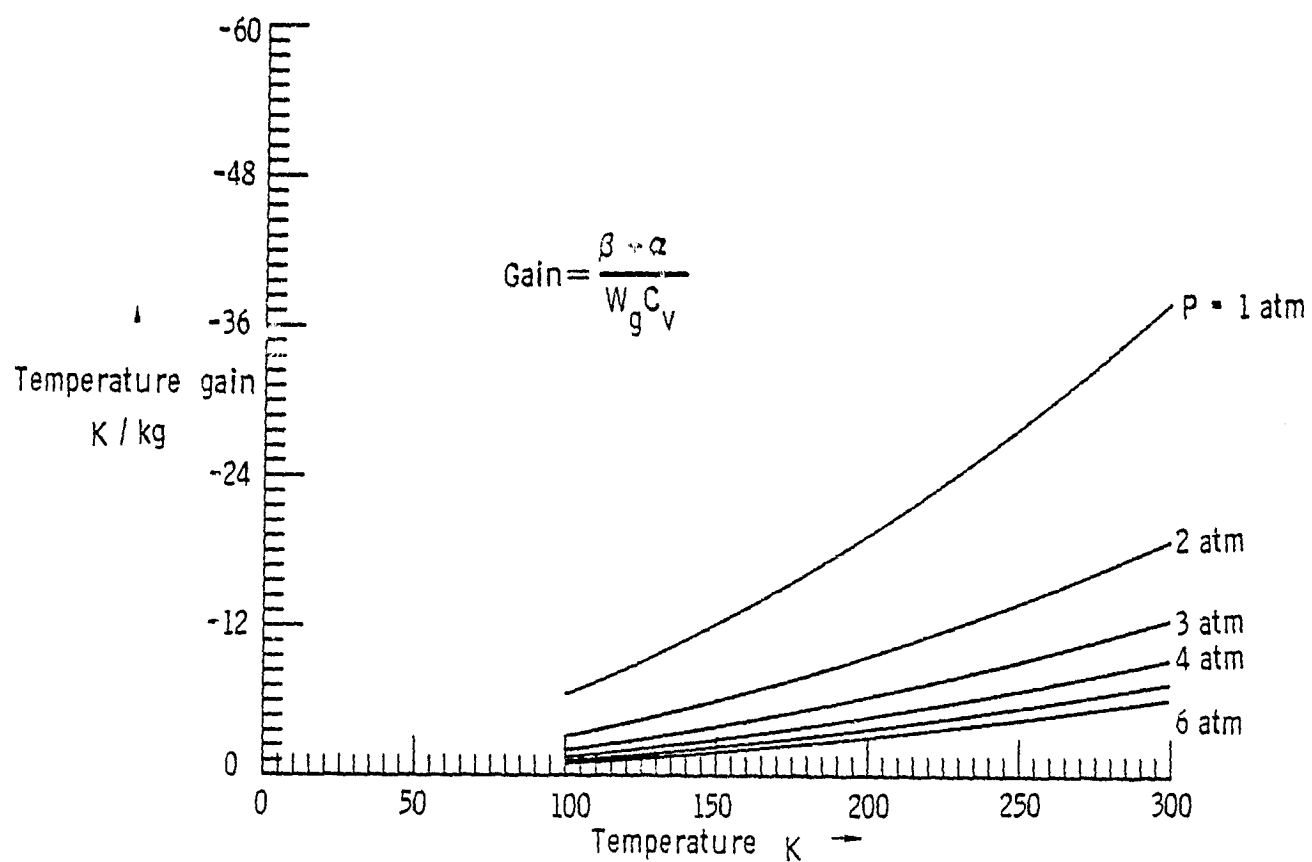


Figure 28. Transient tunnel temperature gain for LN₂ input.

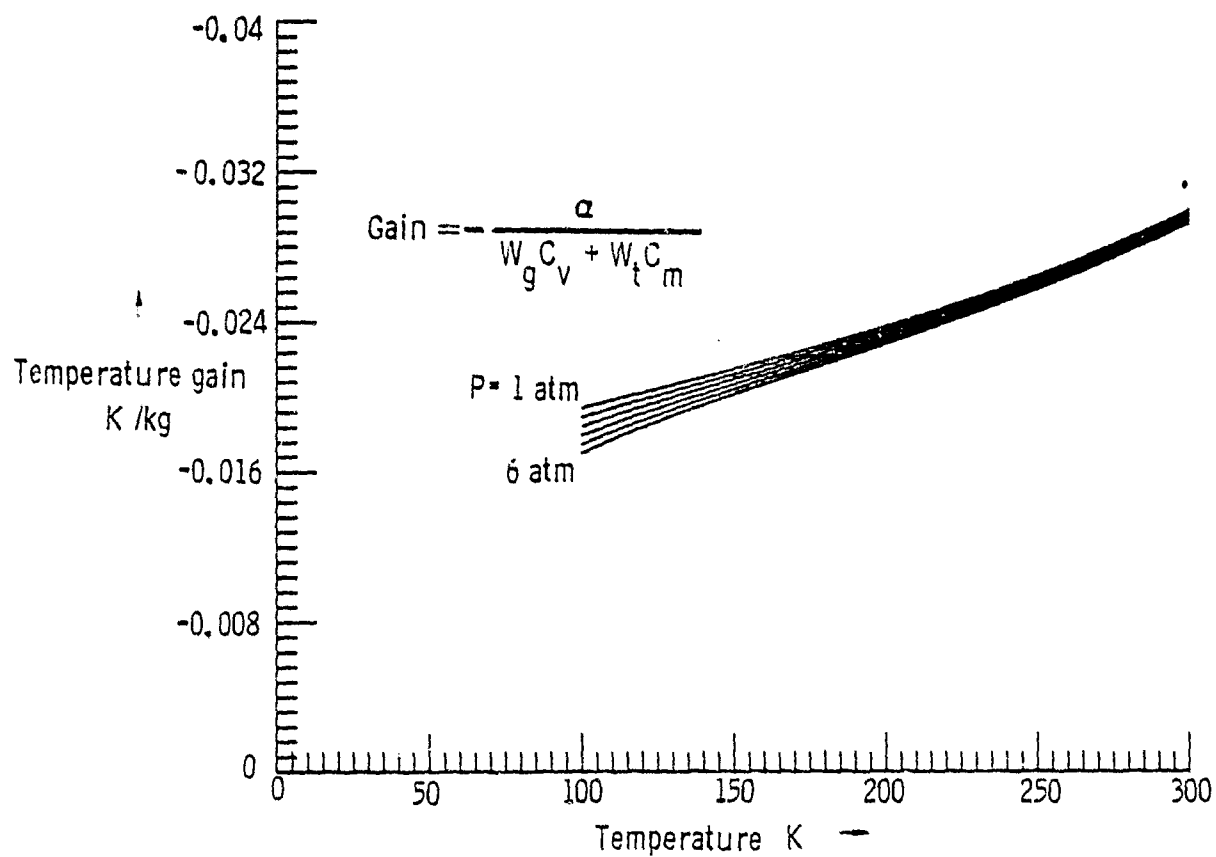


Figure 29. Steady-state tunnel temperature gain for gas bleed.

0.3-m TRANSONIC CRYOGENIC TUNNEL CONTROL CONFIGURATION

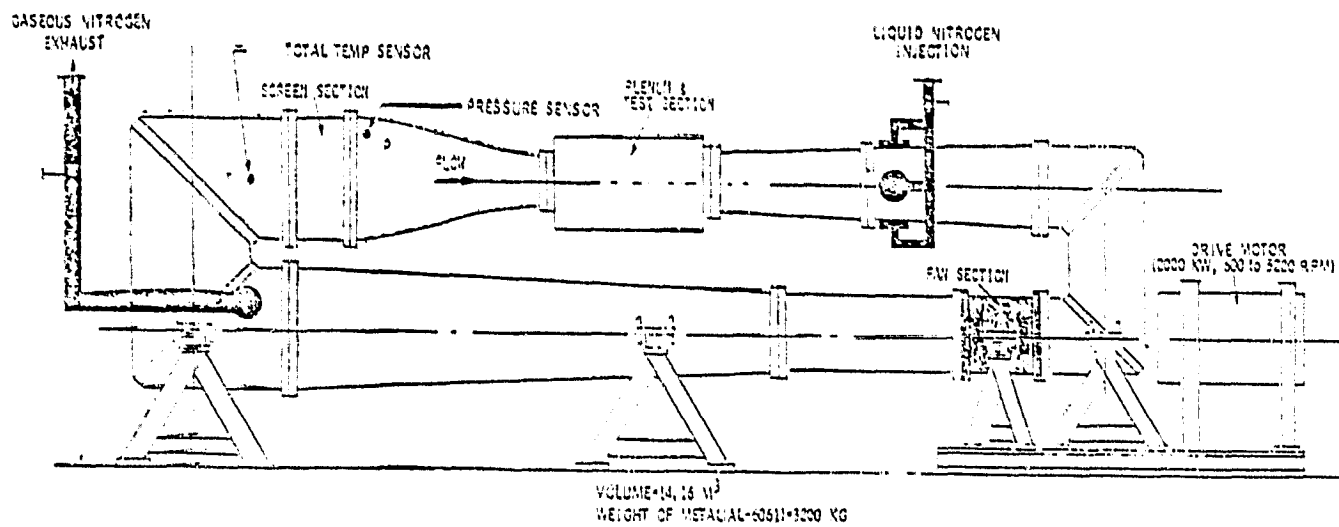


Figure 30. 0.3-m transonic cryogenic tunnel control configuration.

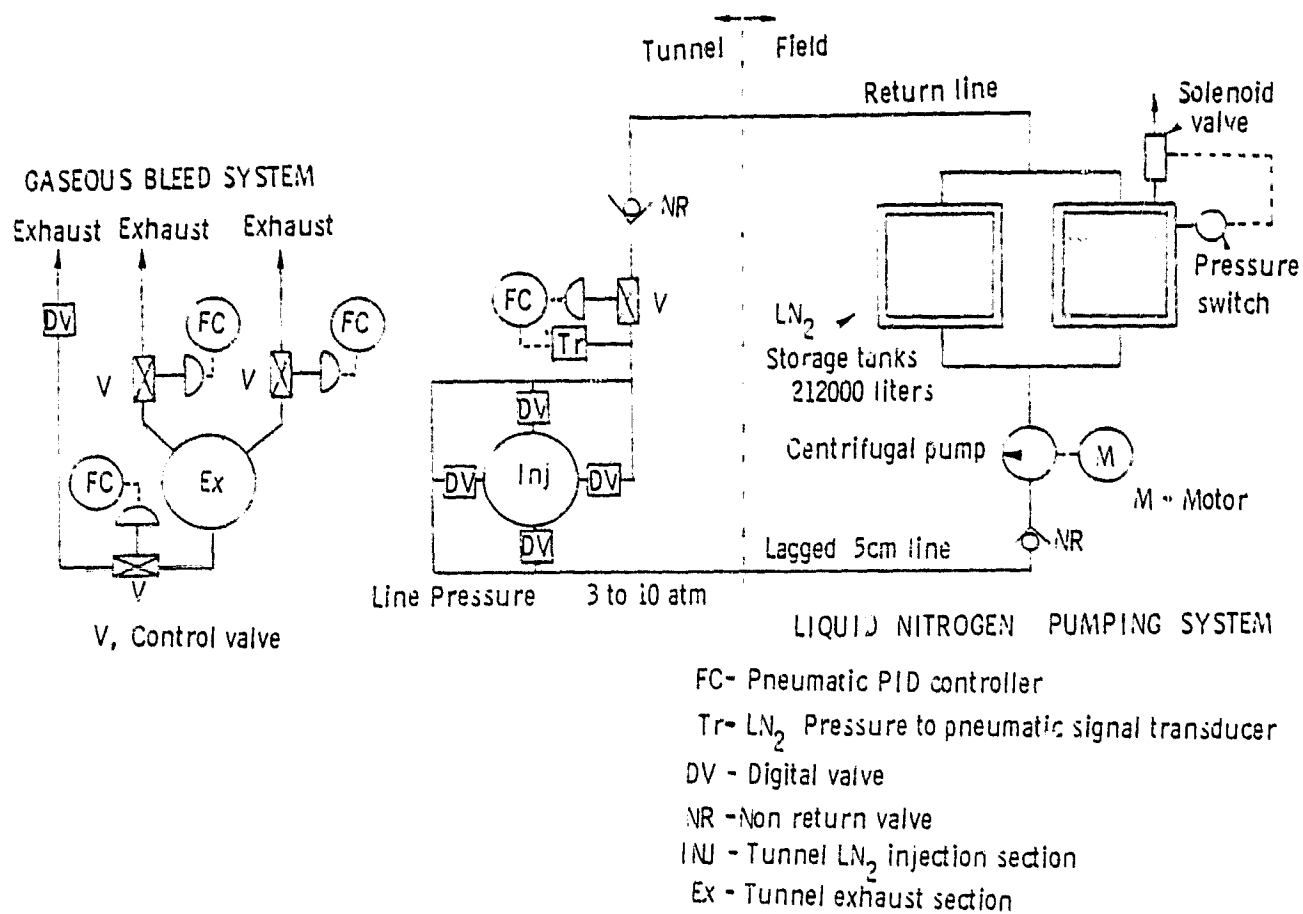
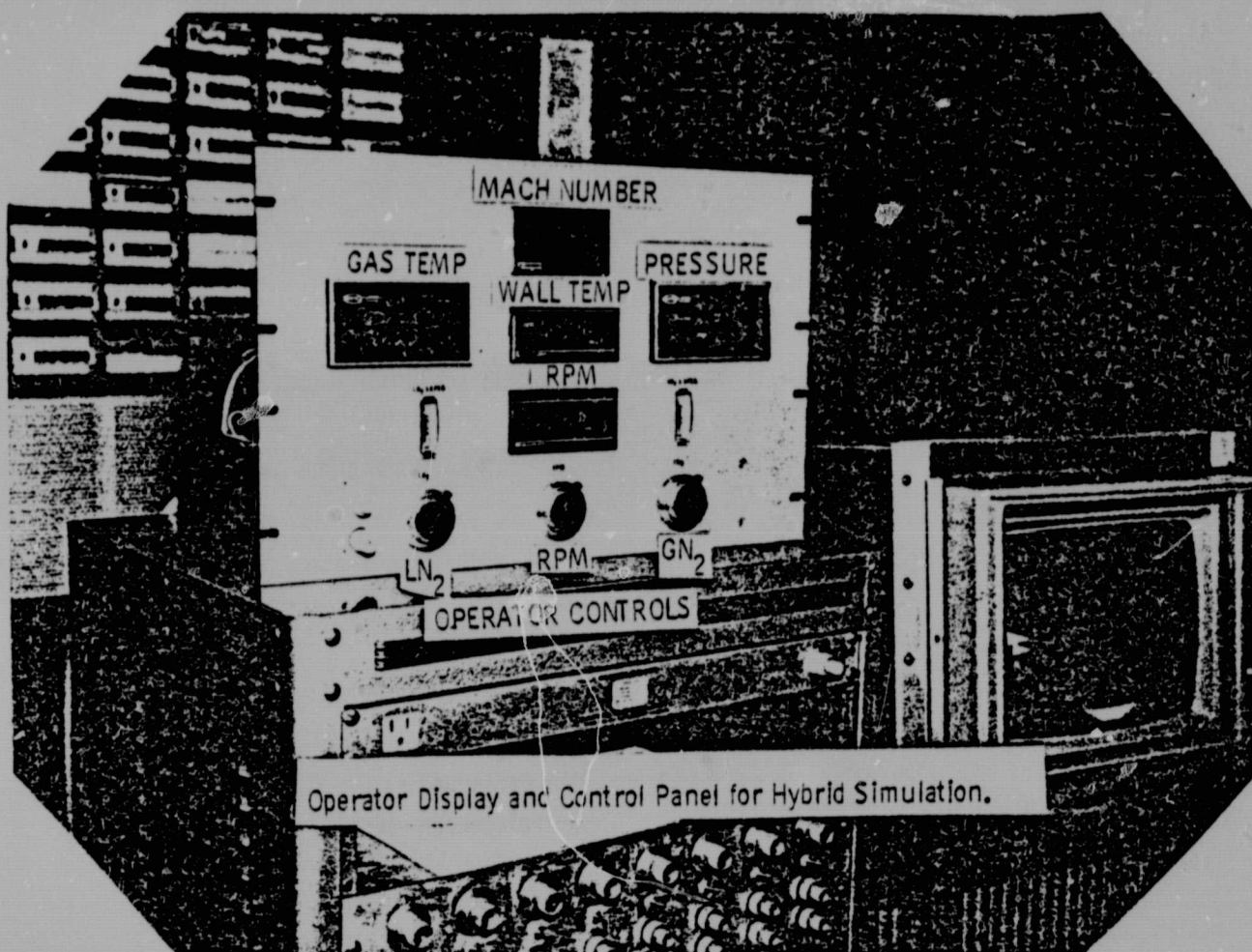


Figure 31. Liquid nitrogen charge and gaseous bleed system schematic diagram.



Operator Display and Control Panel for Hybrid Simulation.

ORIGINAL PAGE IS
OF POOR QUALITY

Figure 32. Operator display and control panel for hybrid simulation.

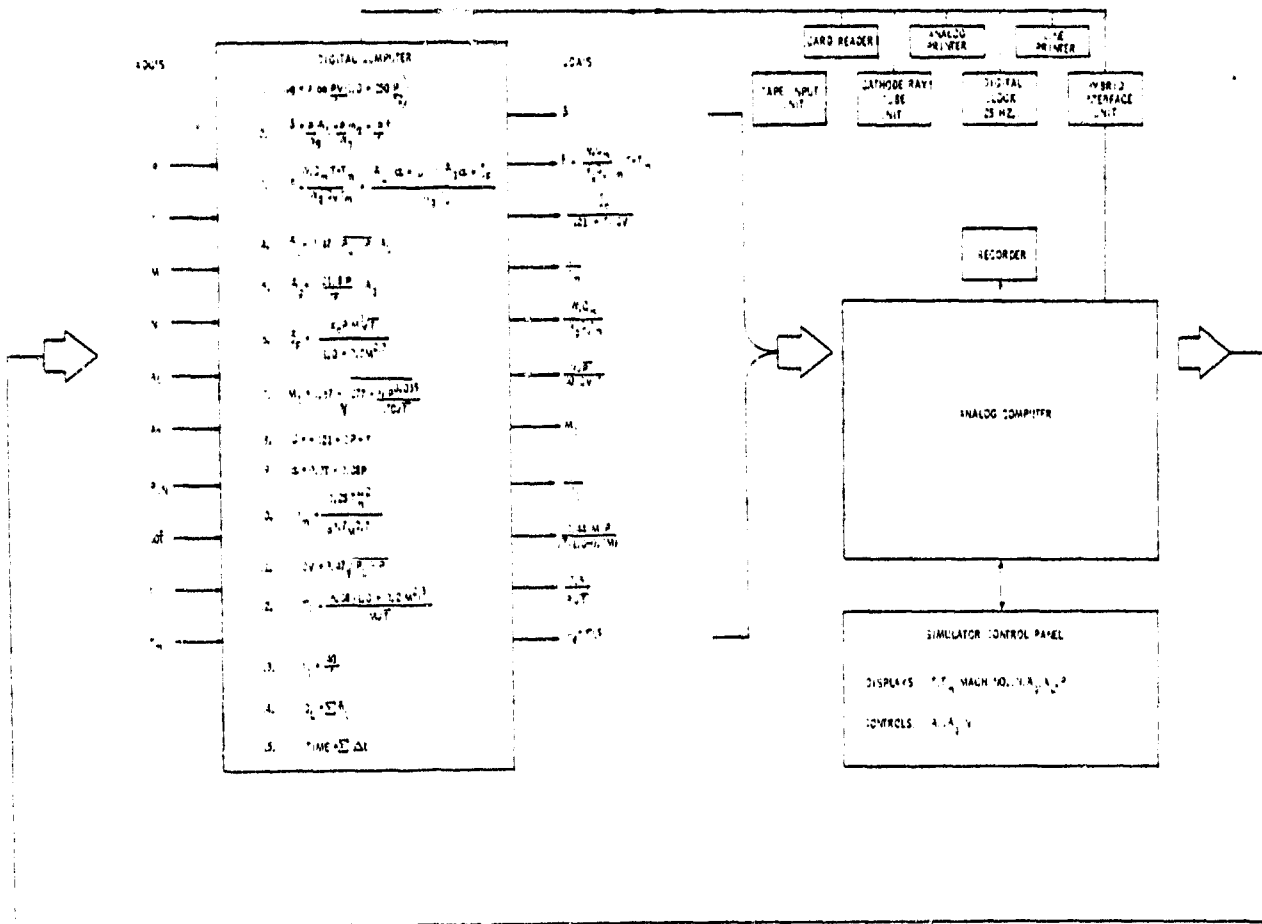


Figure 33. Hybrid simulation of a cryogenic tunnel.

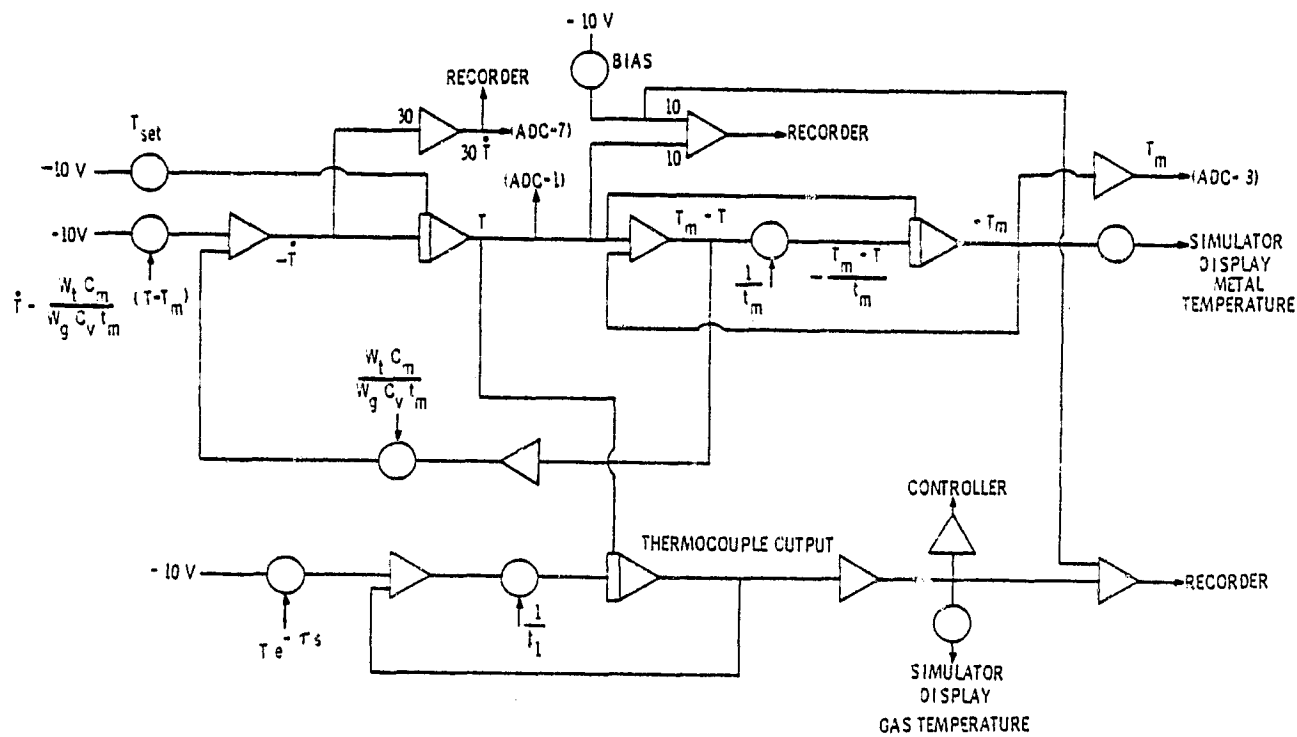


Figure 34. Analog scheme for temperature dynamics simulation.

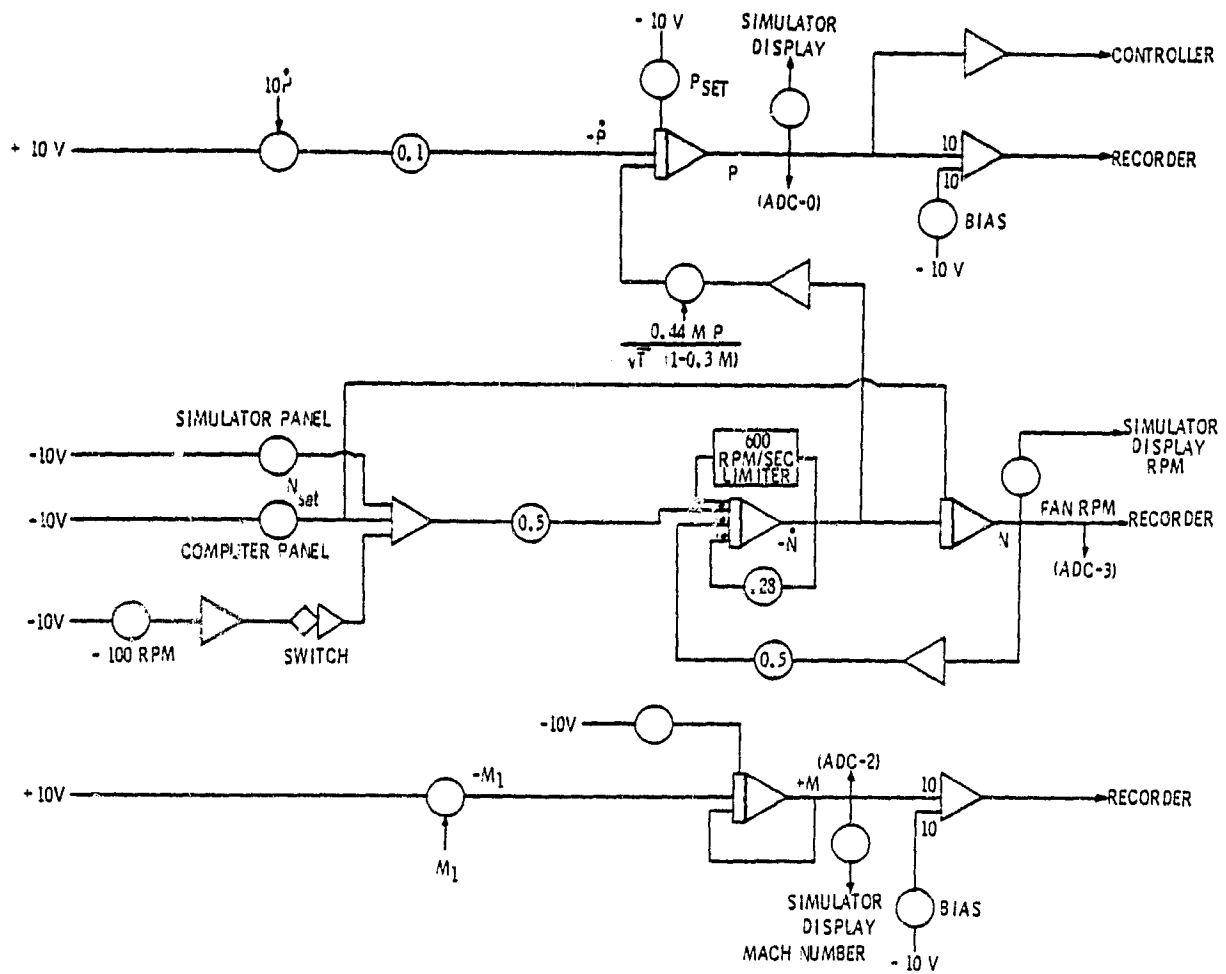


Figure 35. Analog scheme for pressure, fan and Mach number dynamics.

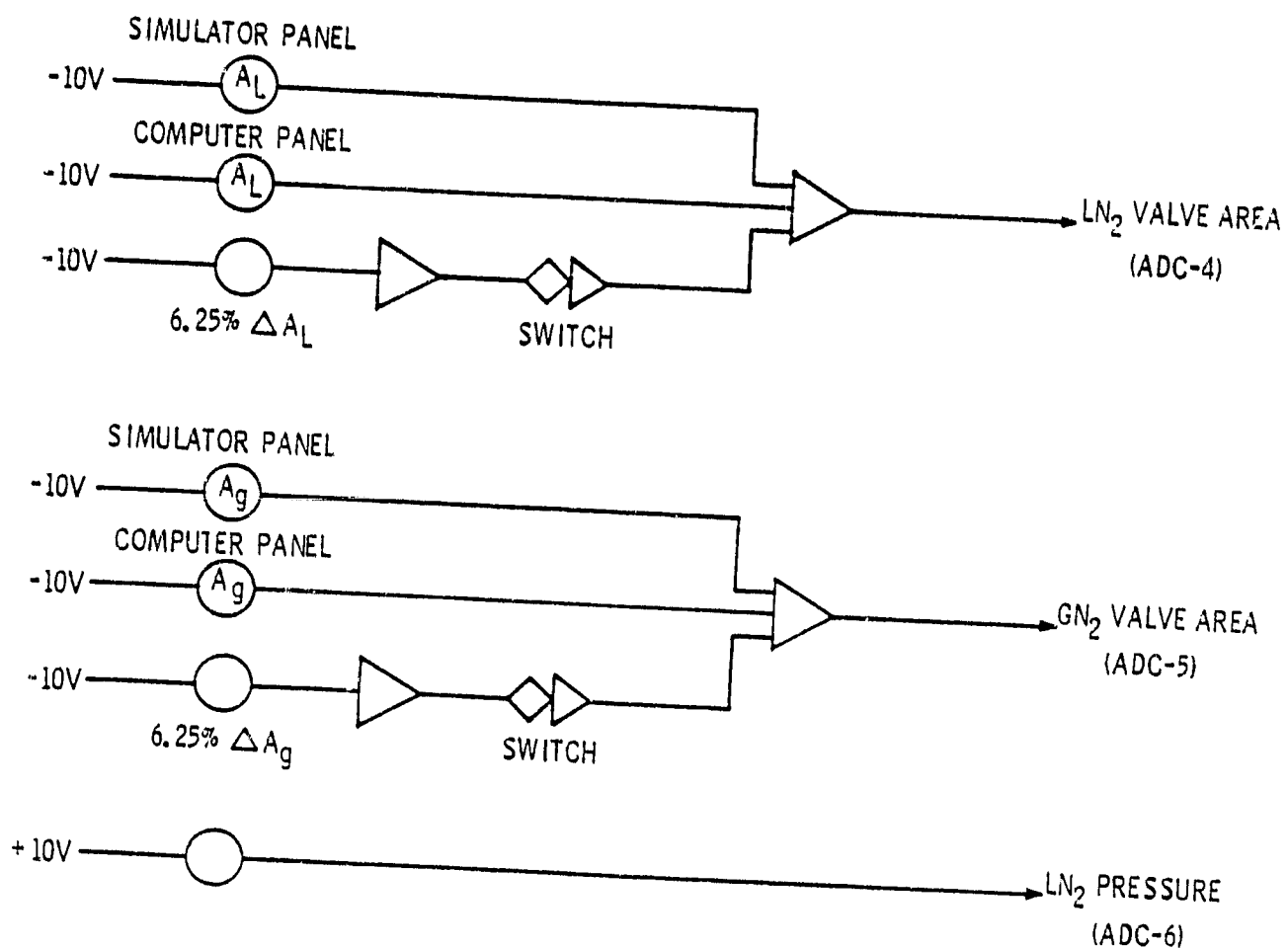


Figure 36. Simulator input function control.

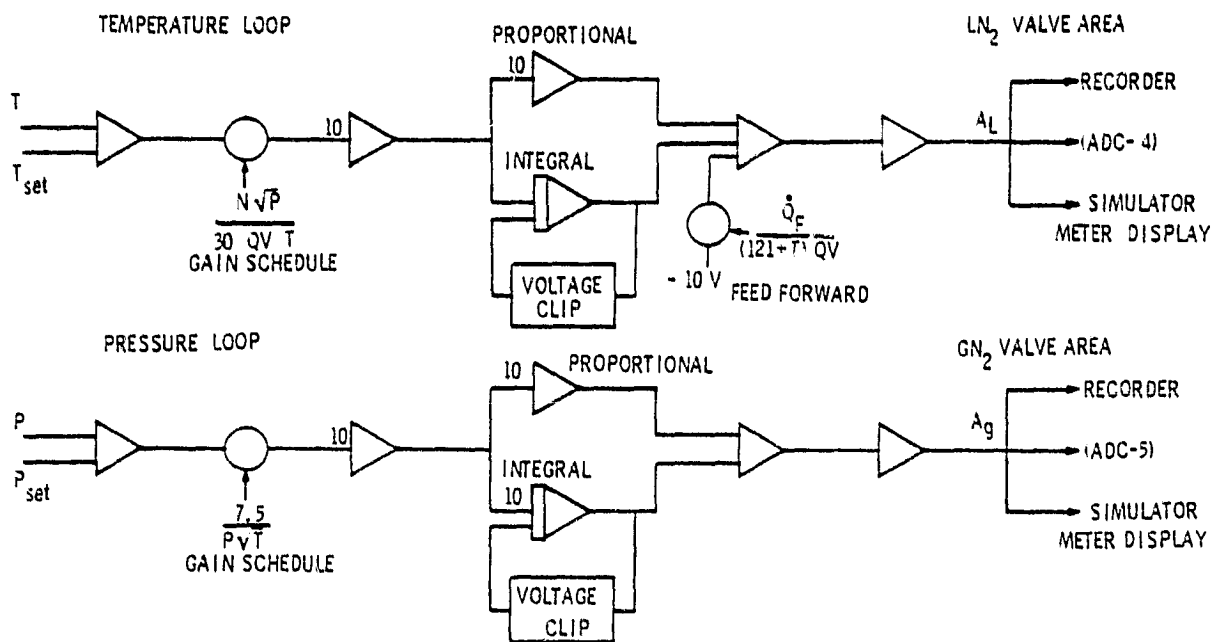


Figure 37. Closed loop controllers.

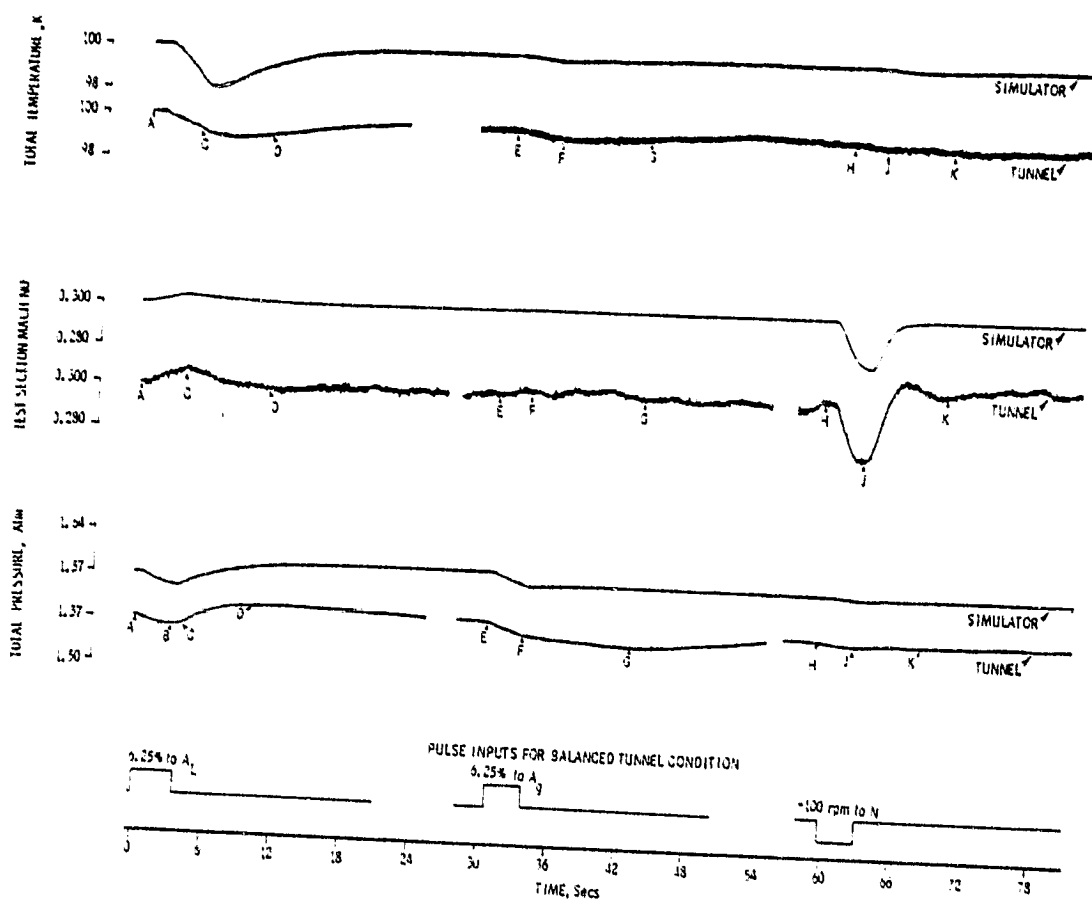


Figure 38. Tunnel and simulator responses; 0.3 M, 1.57 atm, 100 K.

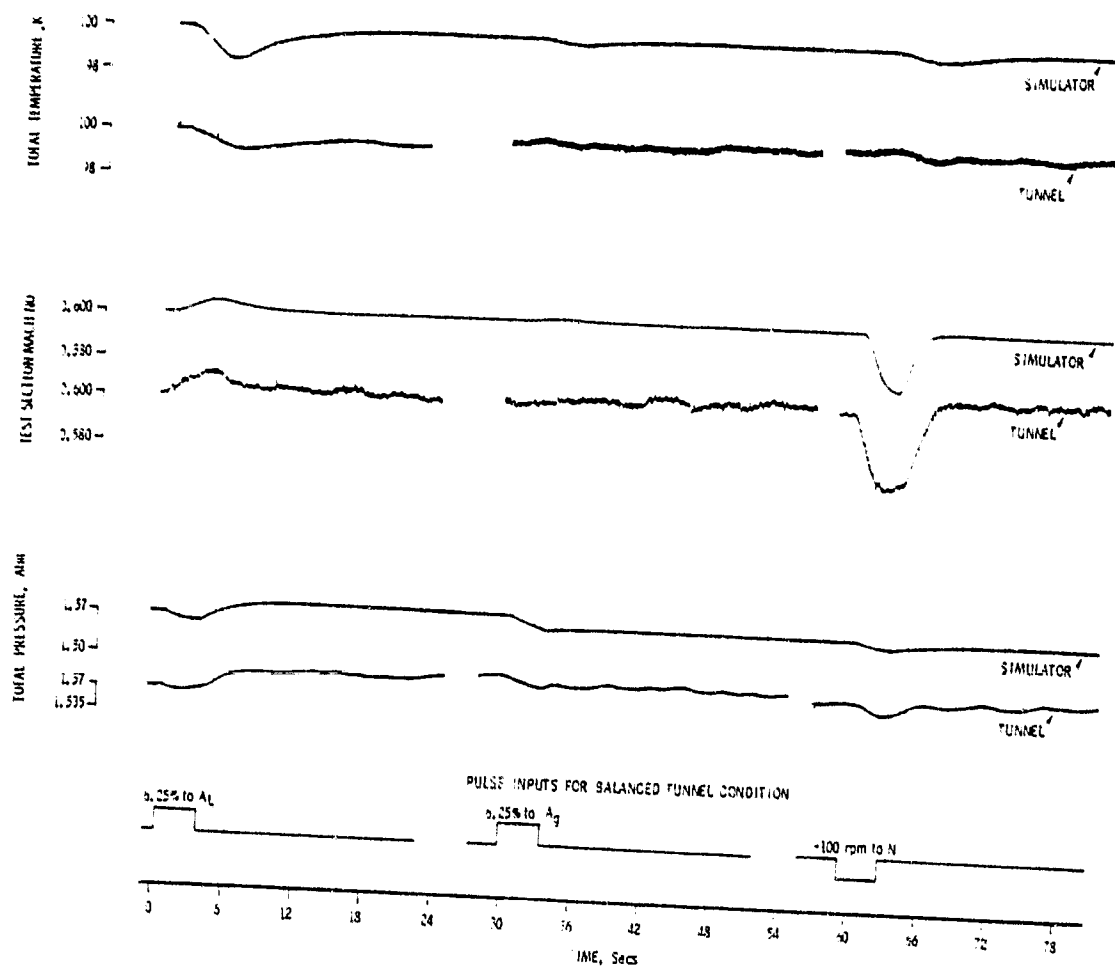


Figure 39. Tunnel and simulator responses; 0.6 M, 1.57 atm, 100 K.

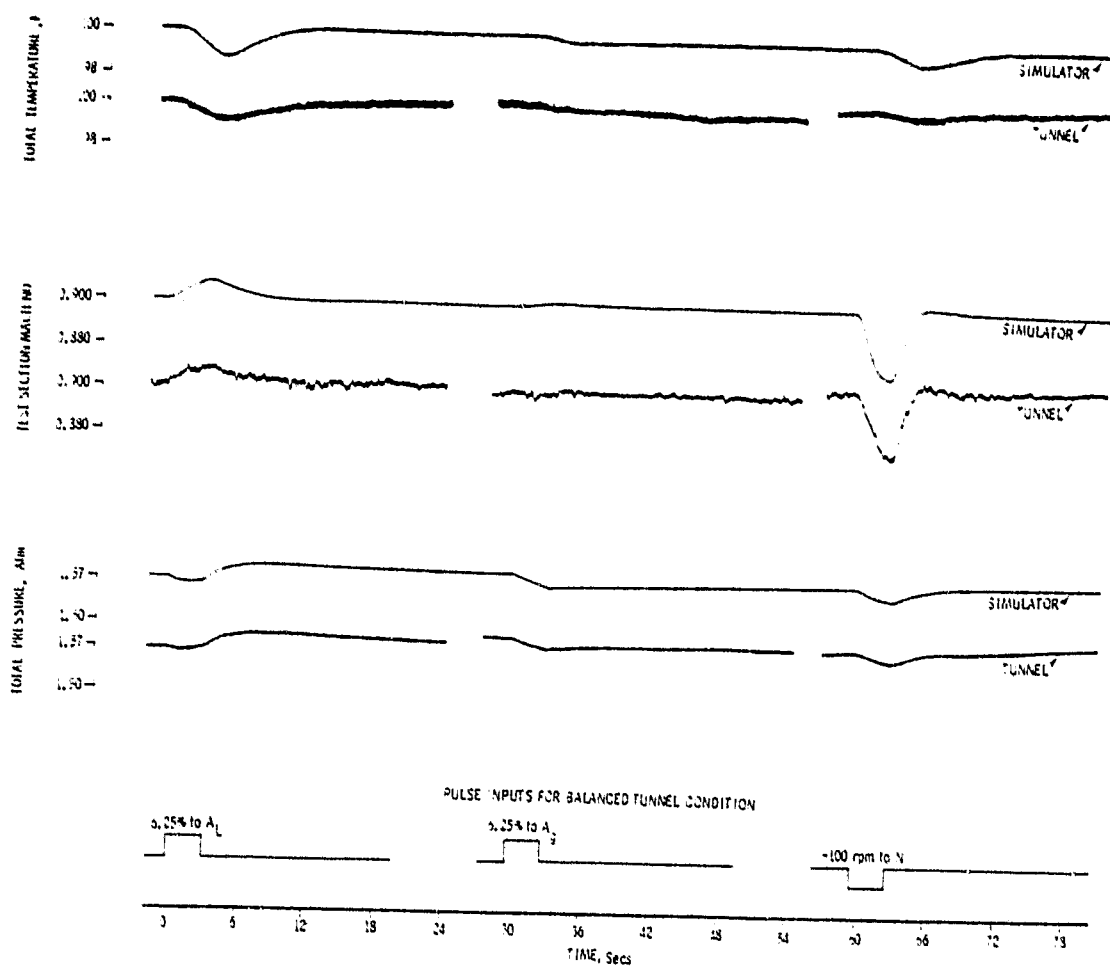


Figure 40. Tunnel and simulator responses; 0.9 M, 1.57 atm, 100 K.

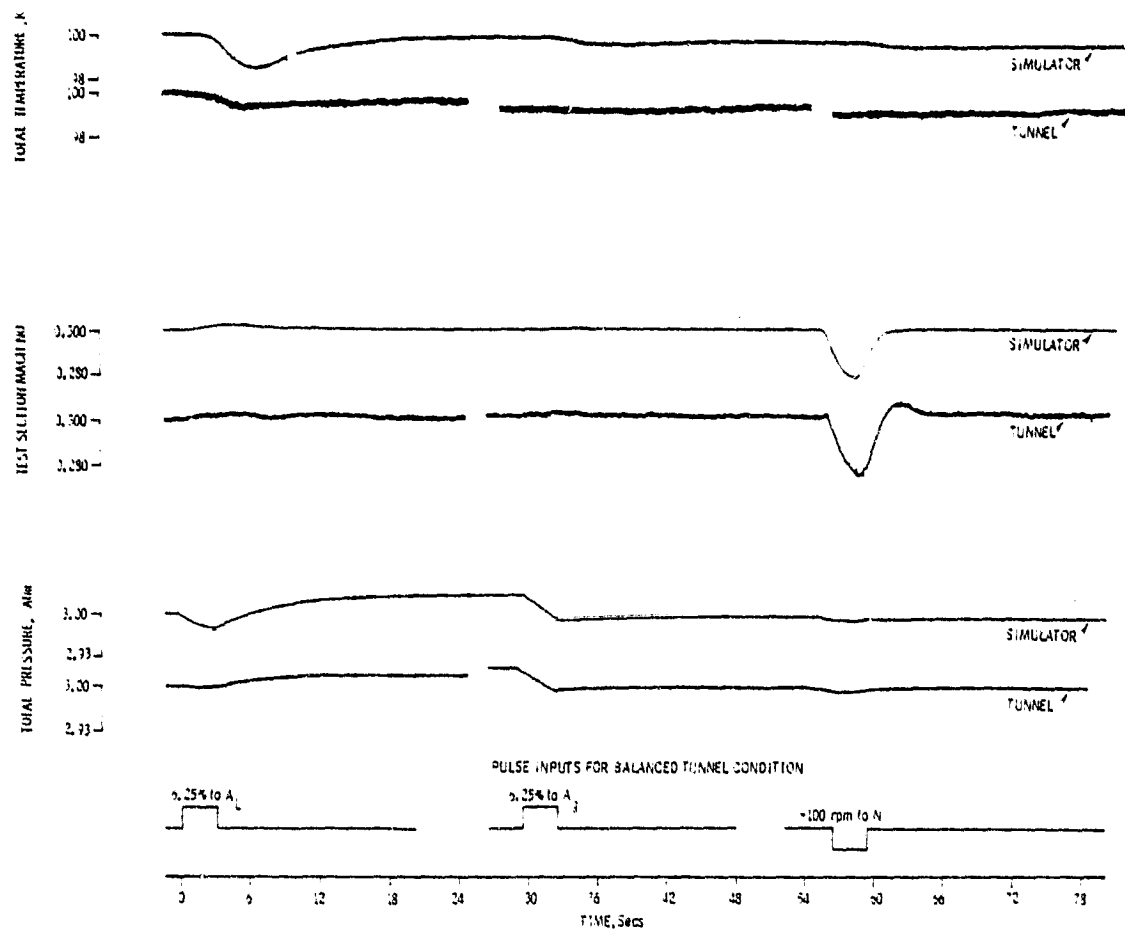


Figure 41. Tunnel and simulator responses; 0.3 M, 3 atm, 100 K.

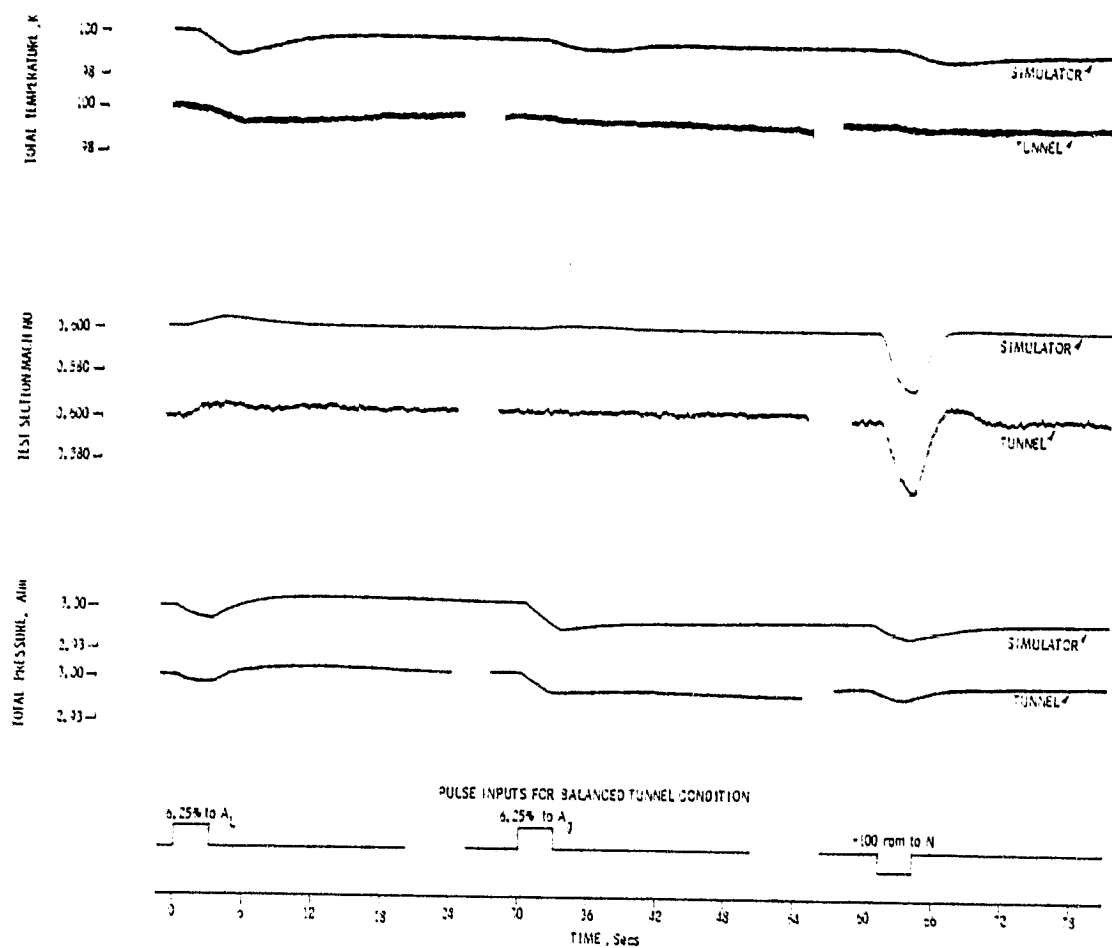


Figure 42. Tunnel and simulator responses; 0.6 M, 3 atm, 100 K.

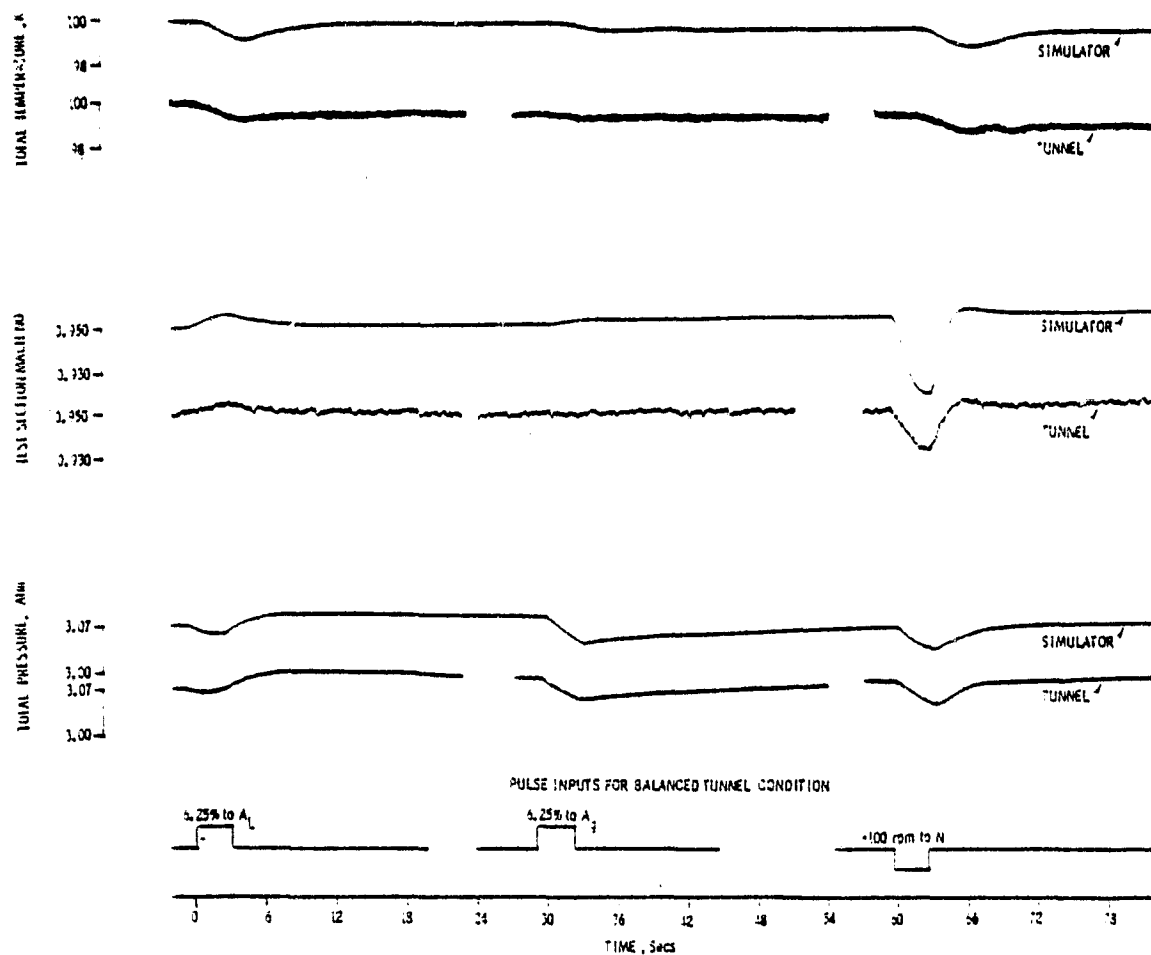


Figure 43. Tunnel and simulator responses; 0.95 M, 3.07 atm, 100 K.

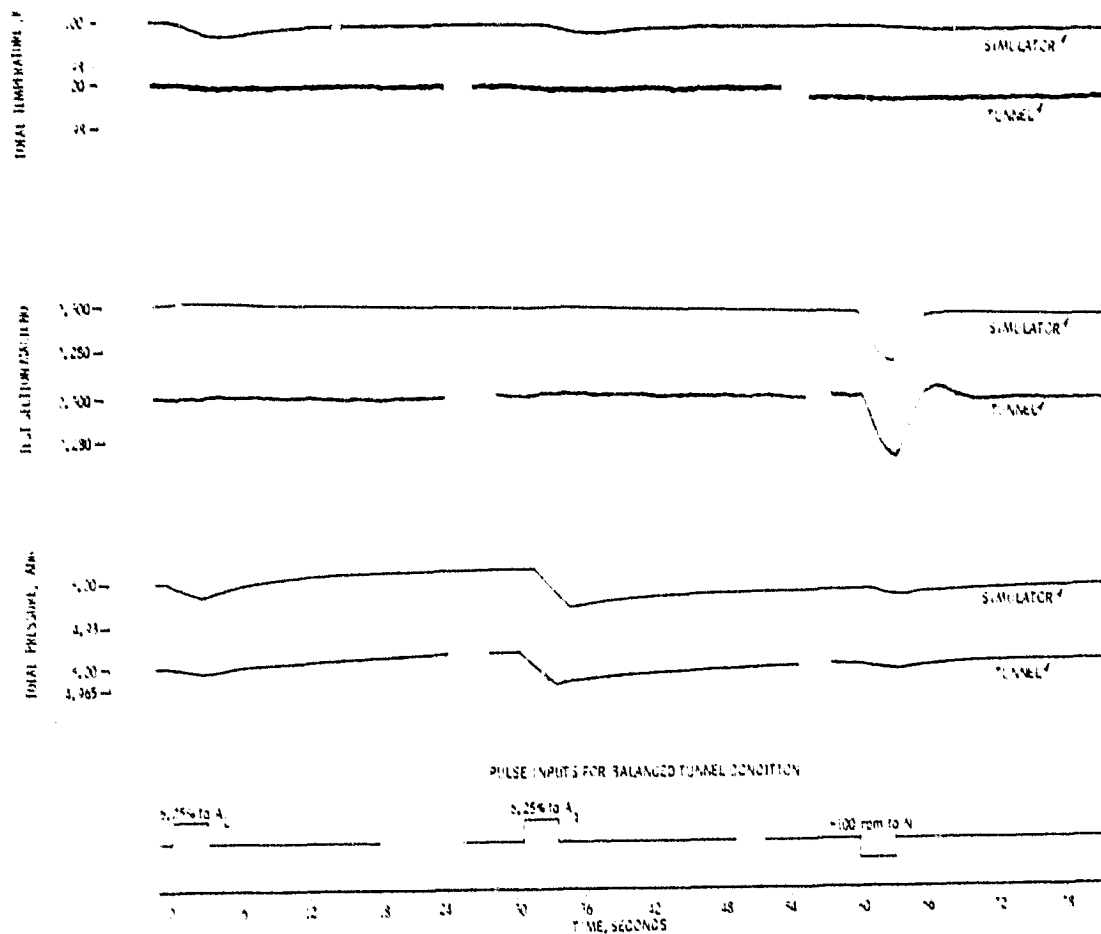


Figure 44. Tunnel and simulator responses; 0.3 M, 5.0 atm, 100 K.

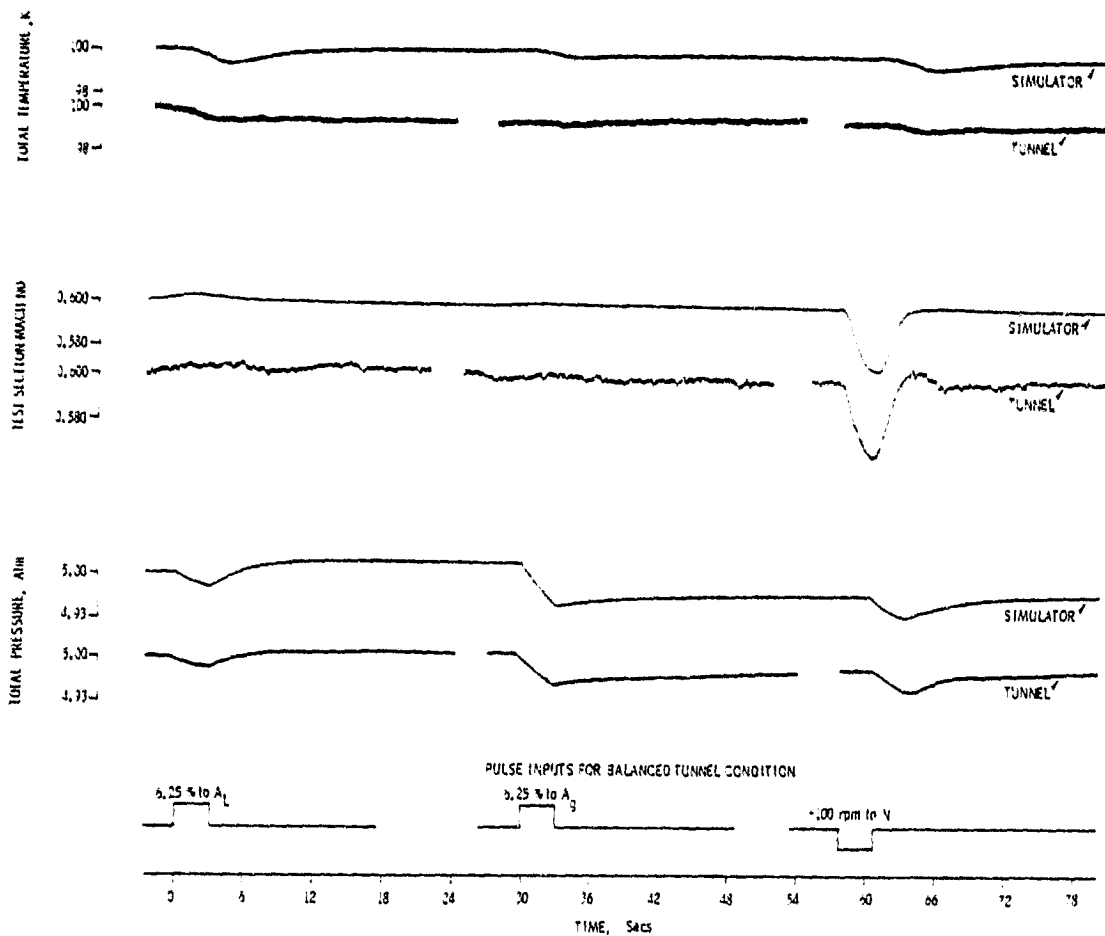


Figure 45. Tunnel and simulator responses; 0.6 M, 5.0 atm, 100 K.

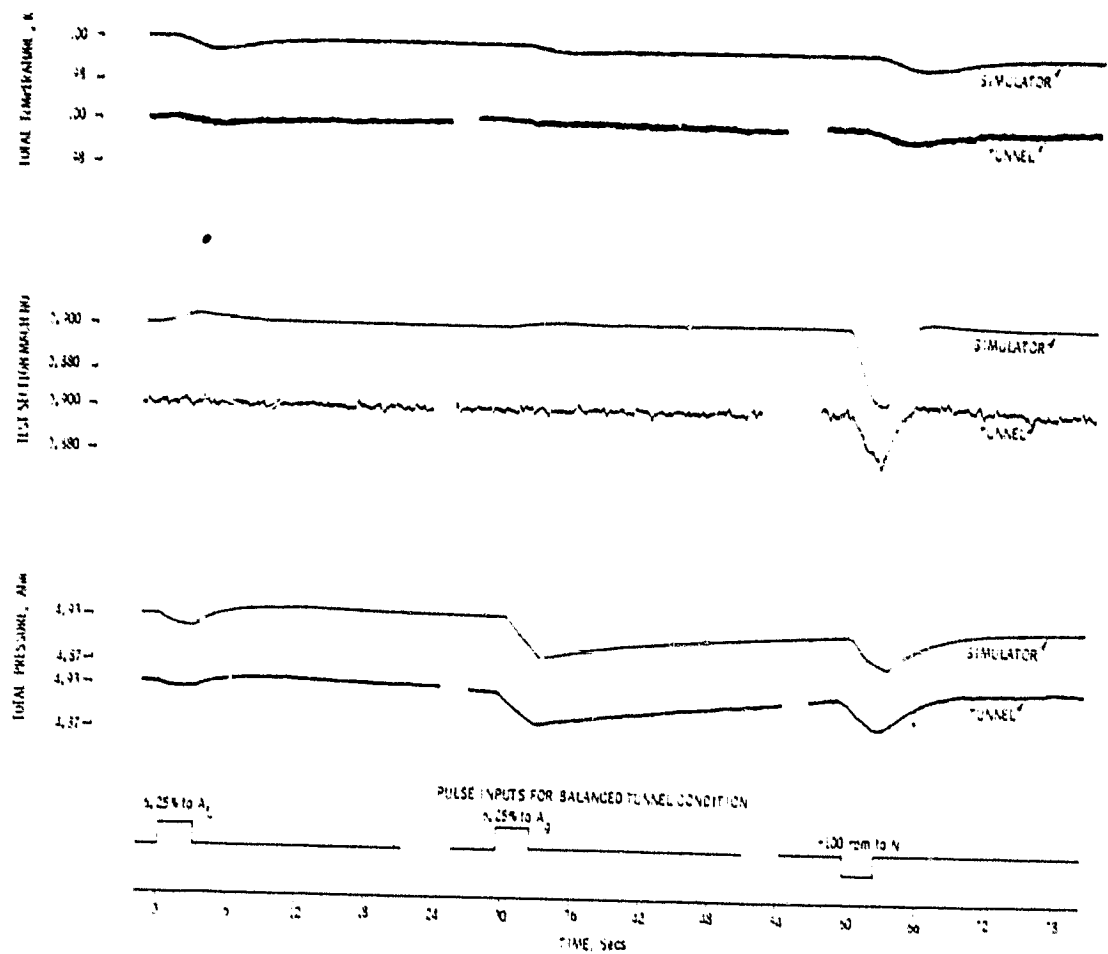


Figure 46. Tunnel and simulator responses; 0.9 M, 4.93 atm, 100 K.

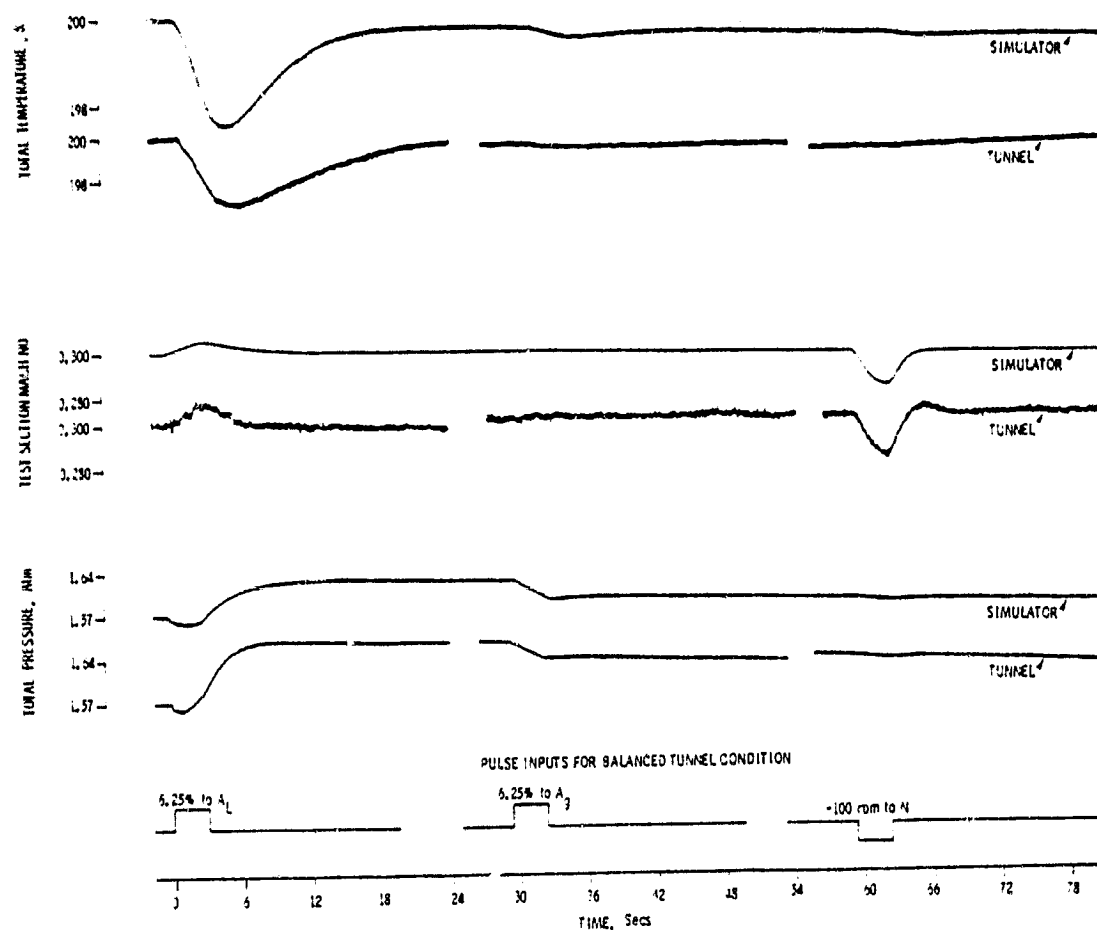


Figure 47. Tunnel and simulator responses; 0.3 M, 1.57 atm, 200 K.

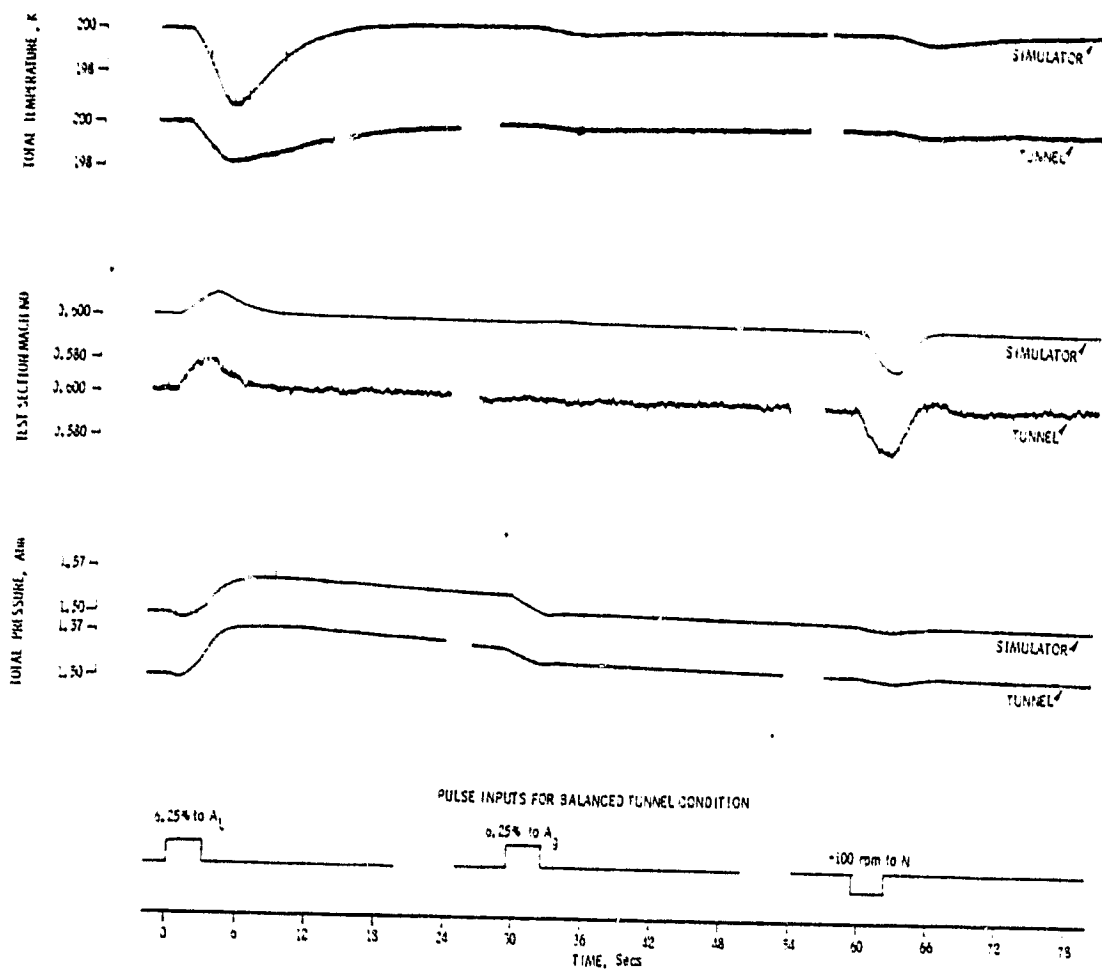


Figure 48. Tunnel and simulator responses; 0.6 M, 1.50 atm, 200 K.

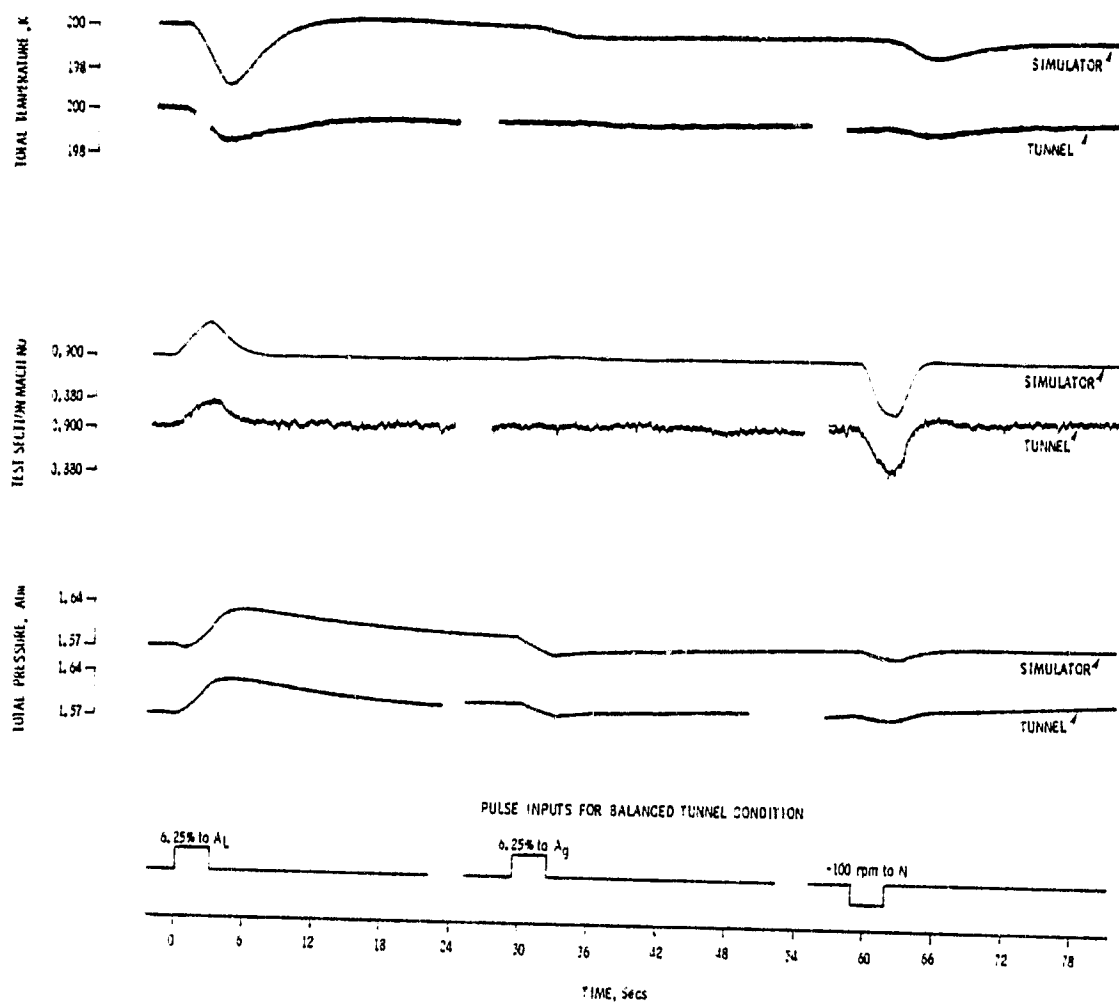


Figure 49. Tunnel and simulator responses; 0.9 M, 1.57 atm, 200 K.

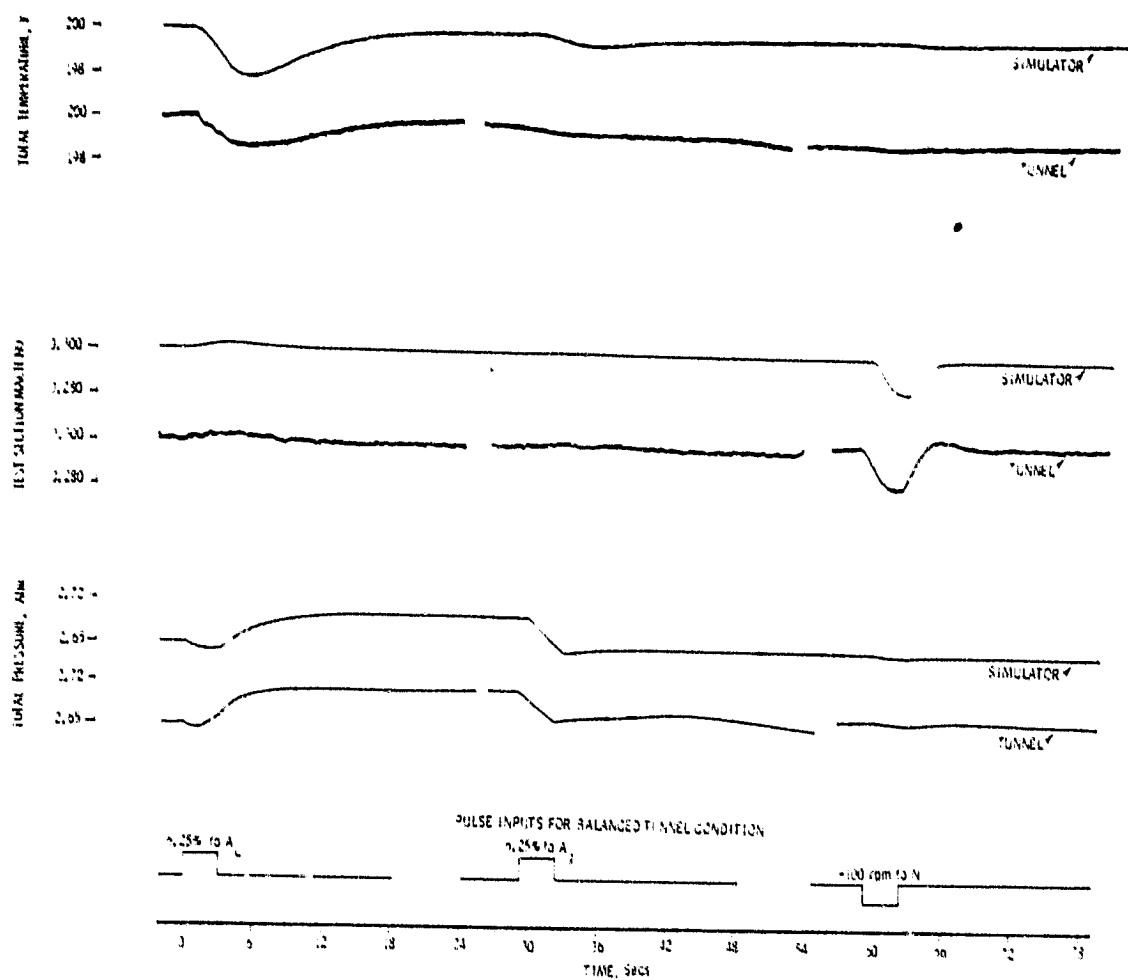


Figure 50. Tunnel and simulator responses; 0.3 M, 2.65 atm, 200 K.

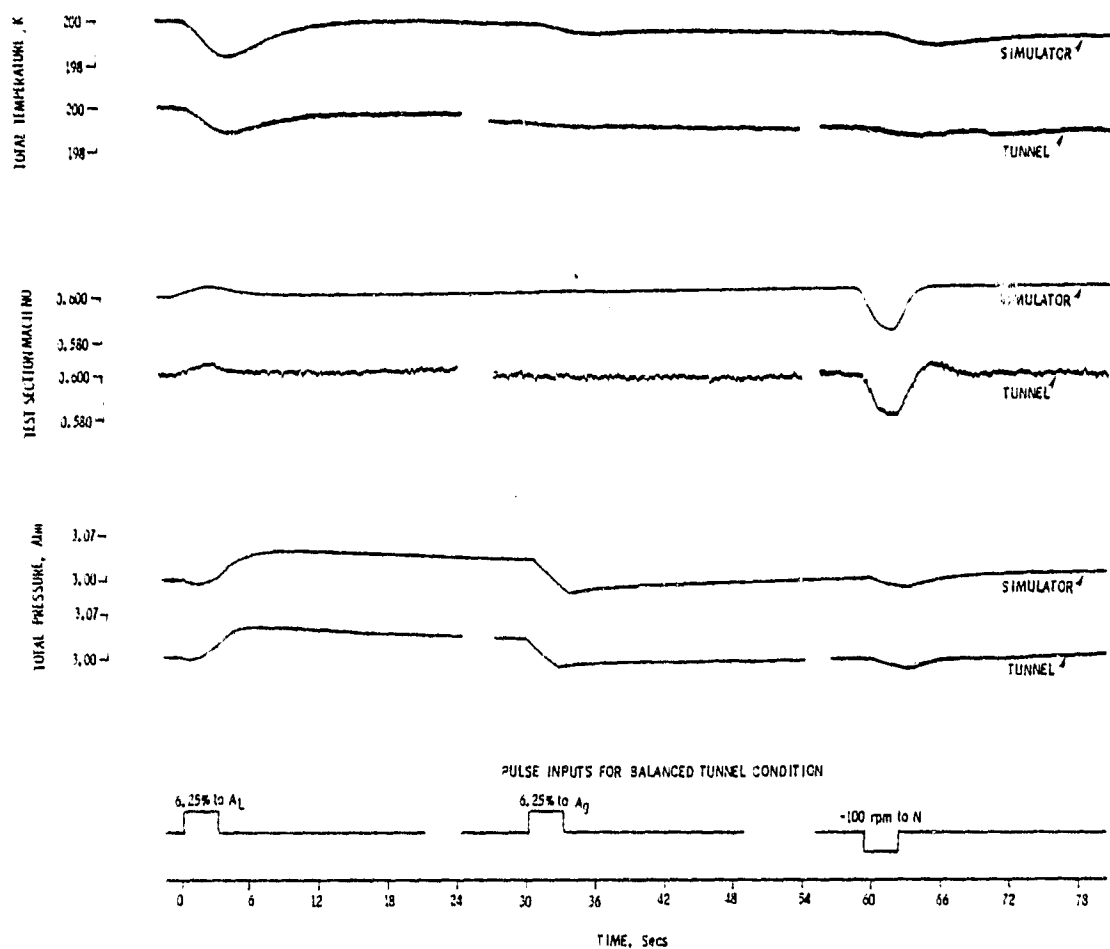


Figure 51. Tunnel and simulator responses; 0.6 M, 3 atm, 200 K.

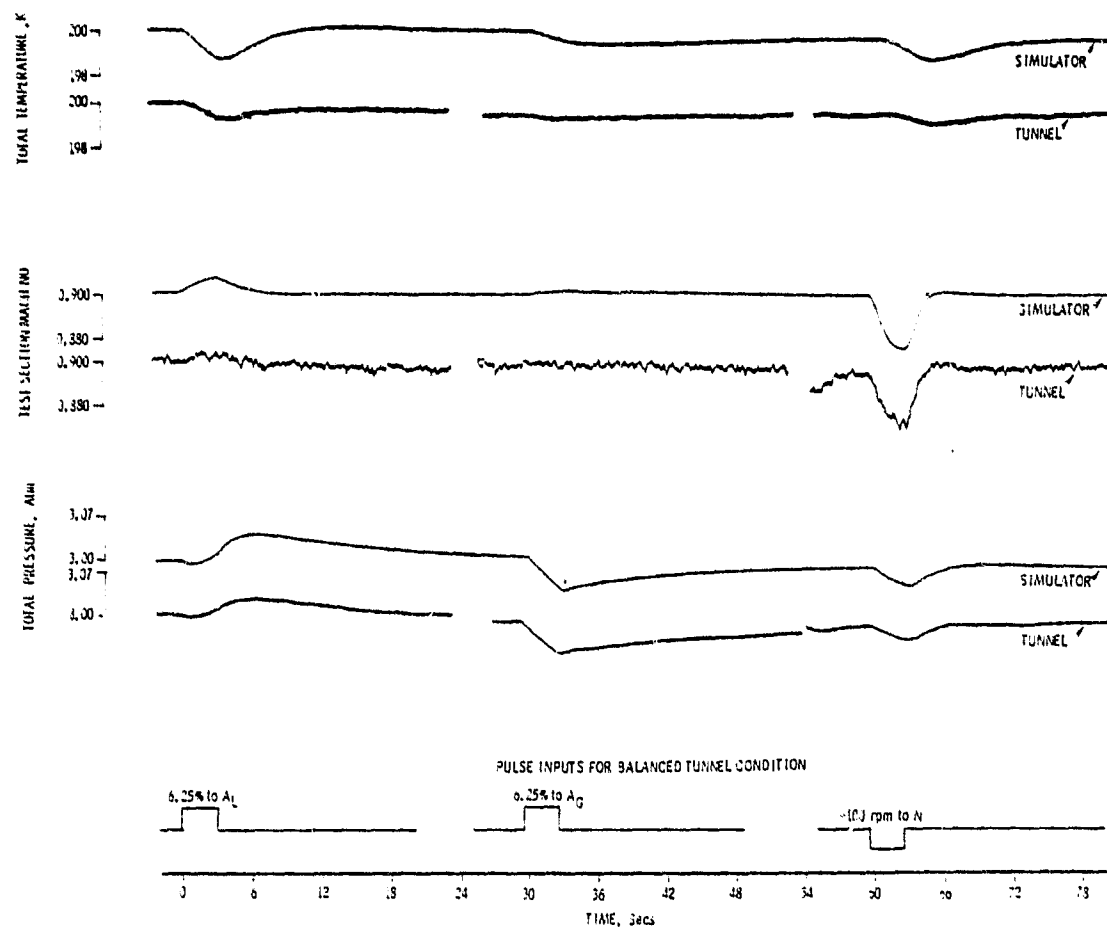


Figure 52. Tunnel and simulator responses; 0.9 M, 3 atm, 200 K.

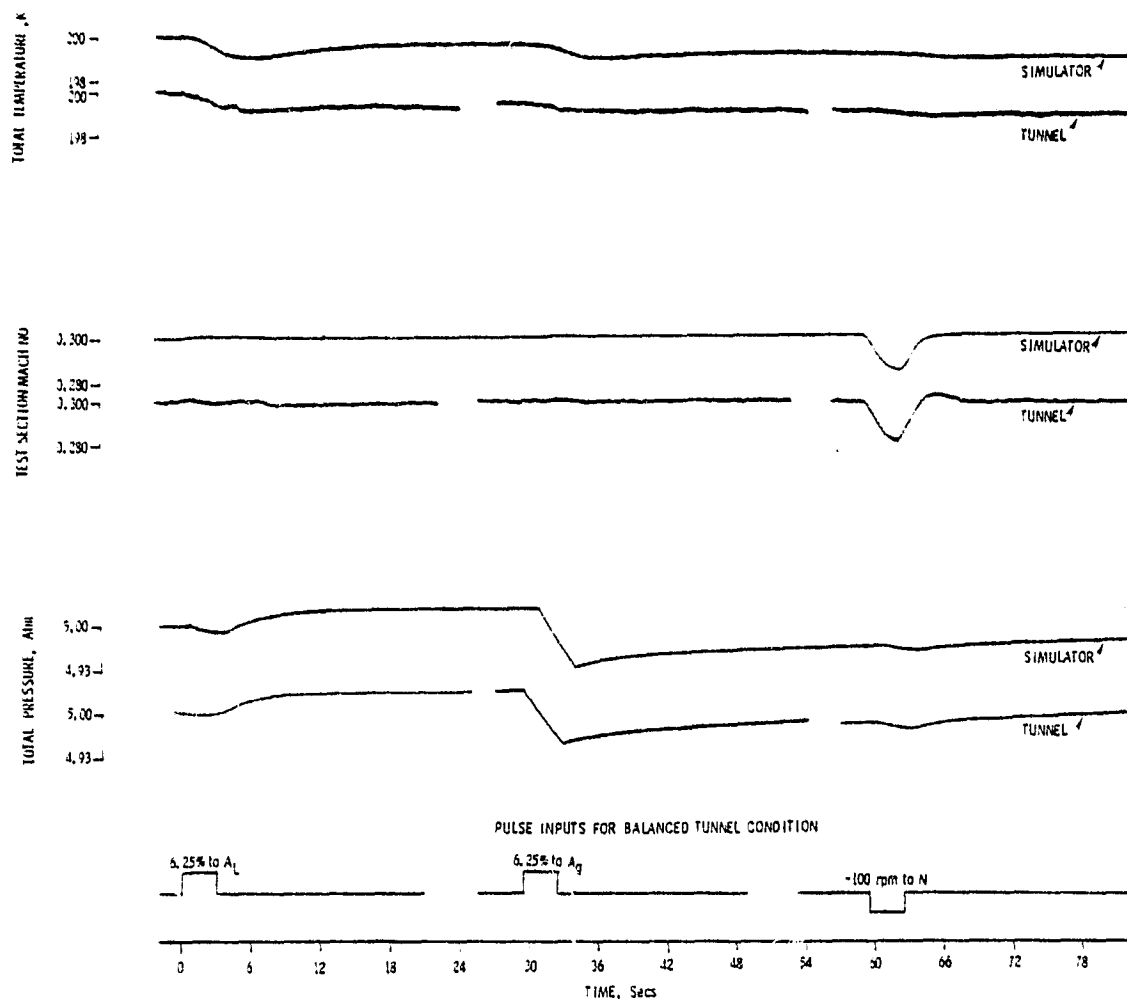


Figure 53. Tunnel and simulator responses; 0.3 M, 5 atm, 200 K.

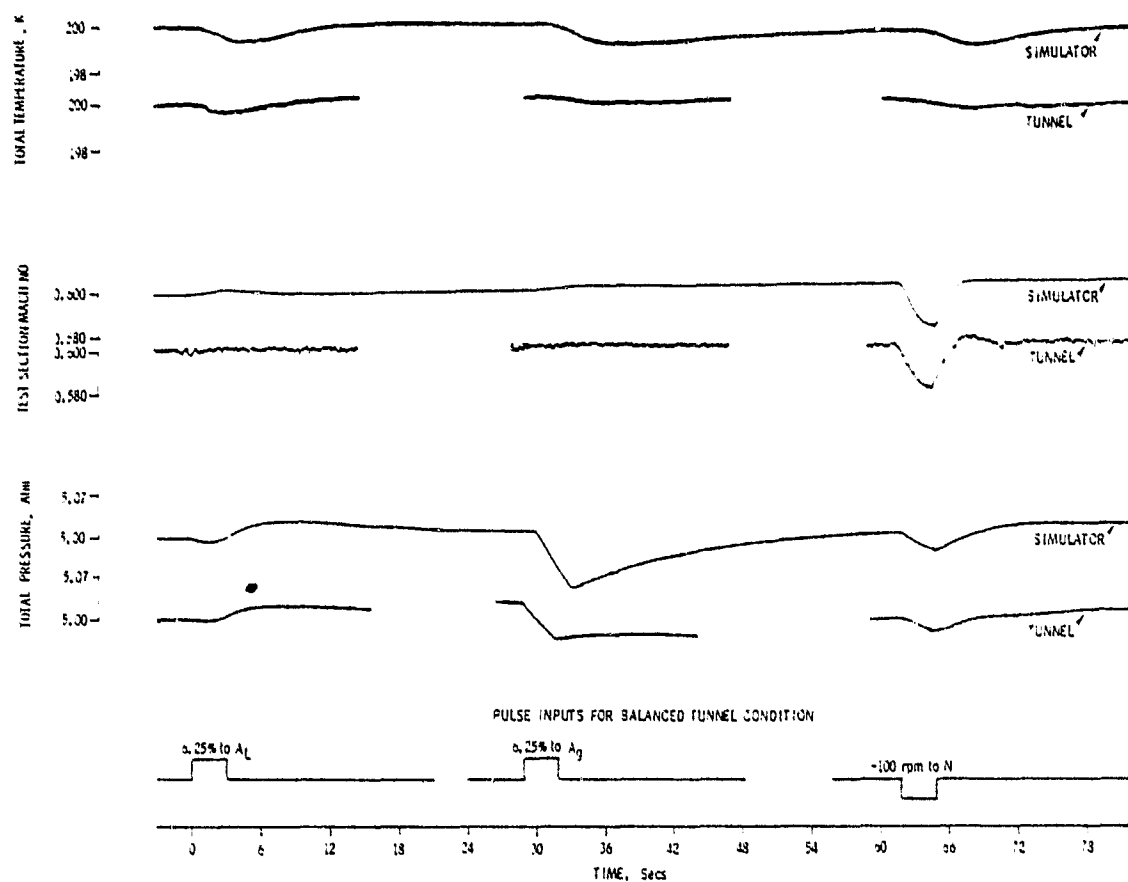


Figure 54. Tunnel and simulator responses; 0.6 M, 5 atm, 200 K.

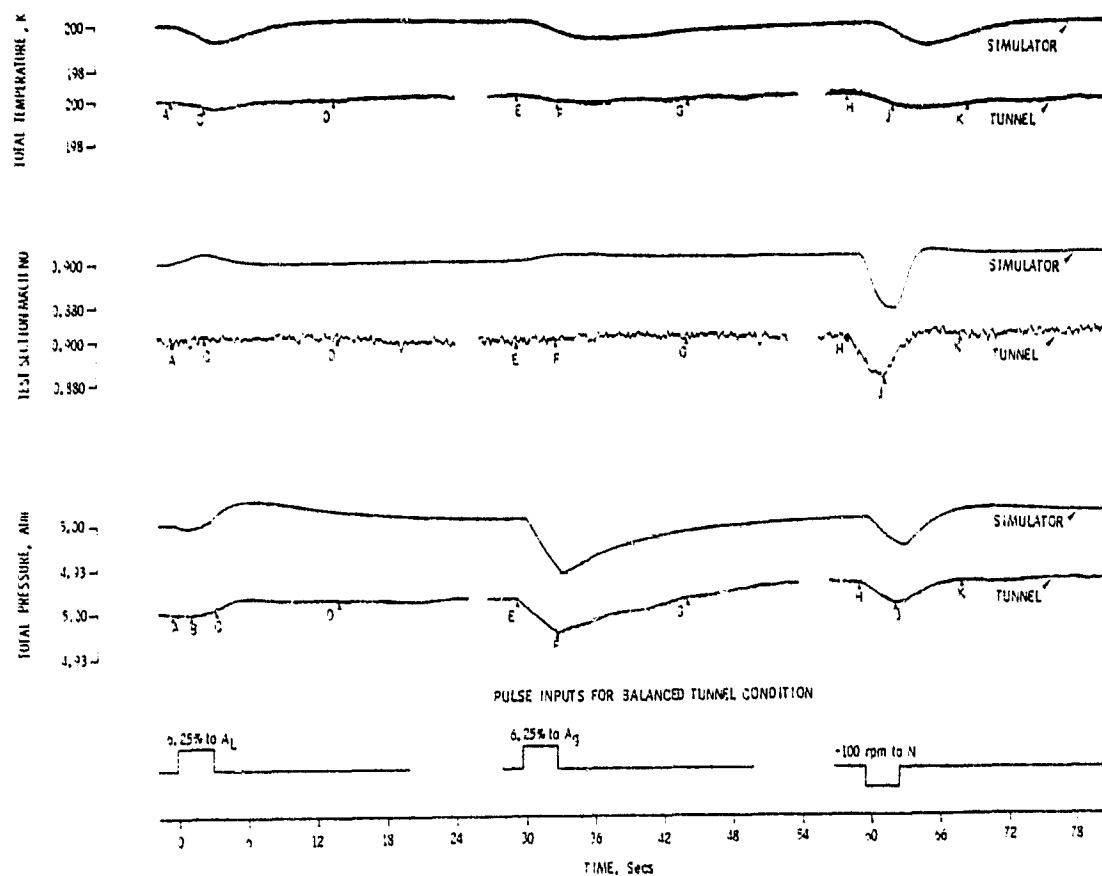


Figure 55. Tunnel and simulator responses; 0.9 M, 5 atm, 200 K.

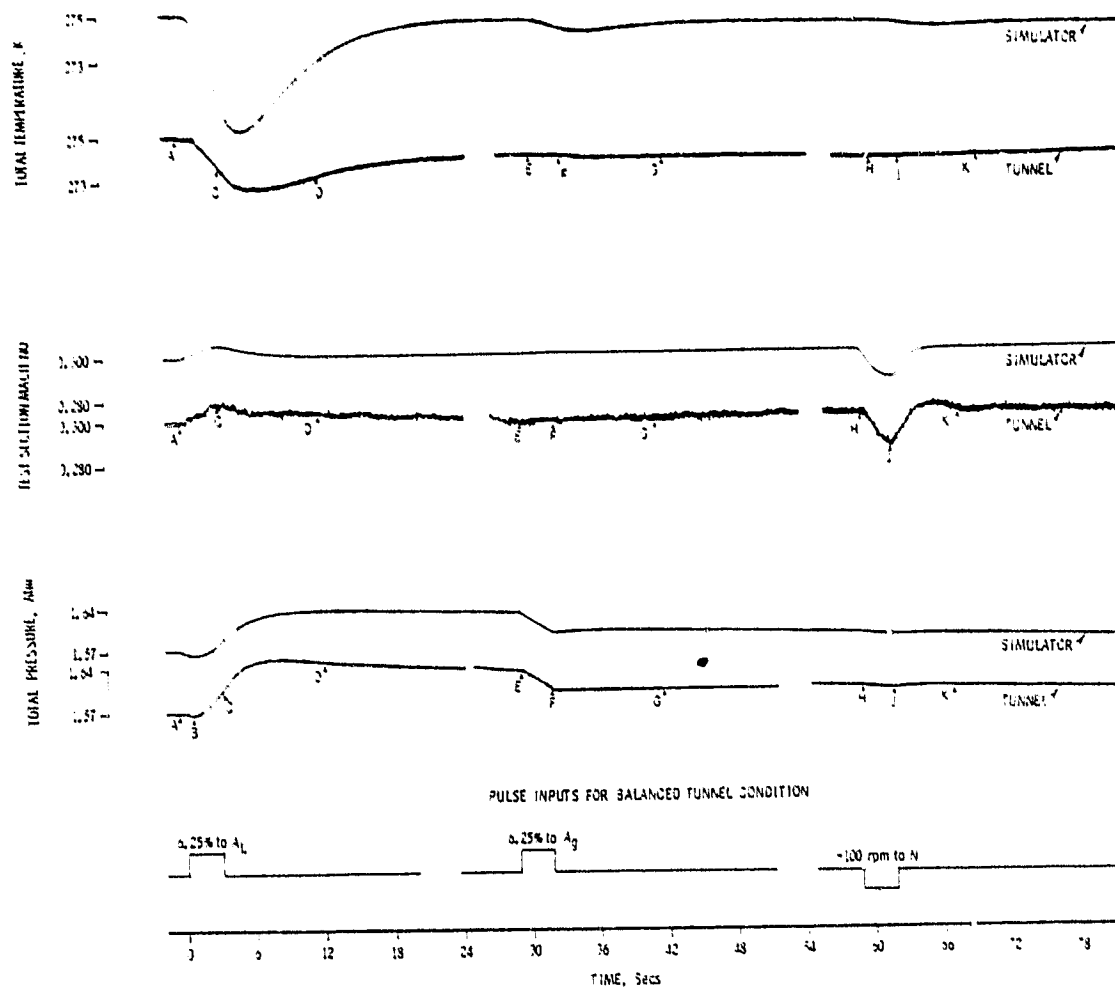


Figure 56. Tunnel and simulator responses; 0.3 M, 1.57 atm, 275 K.

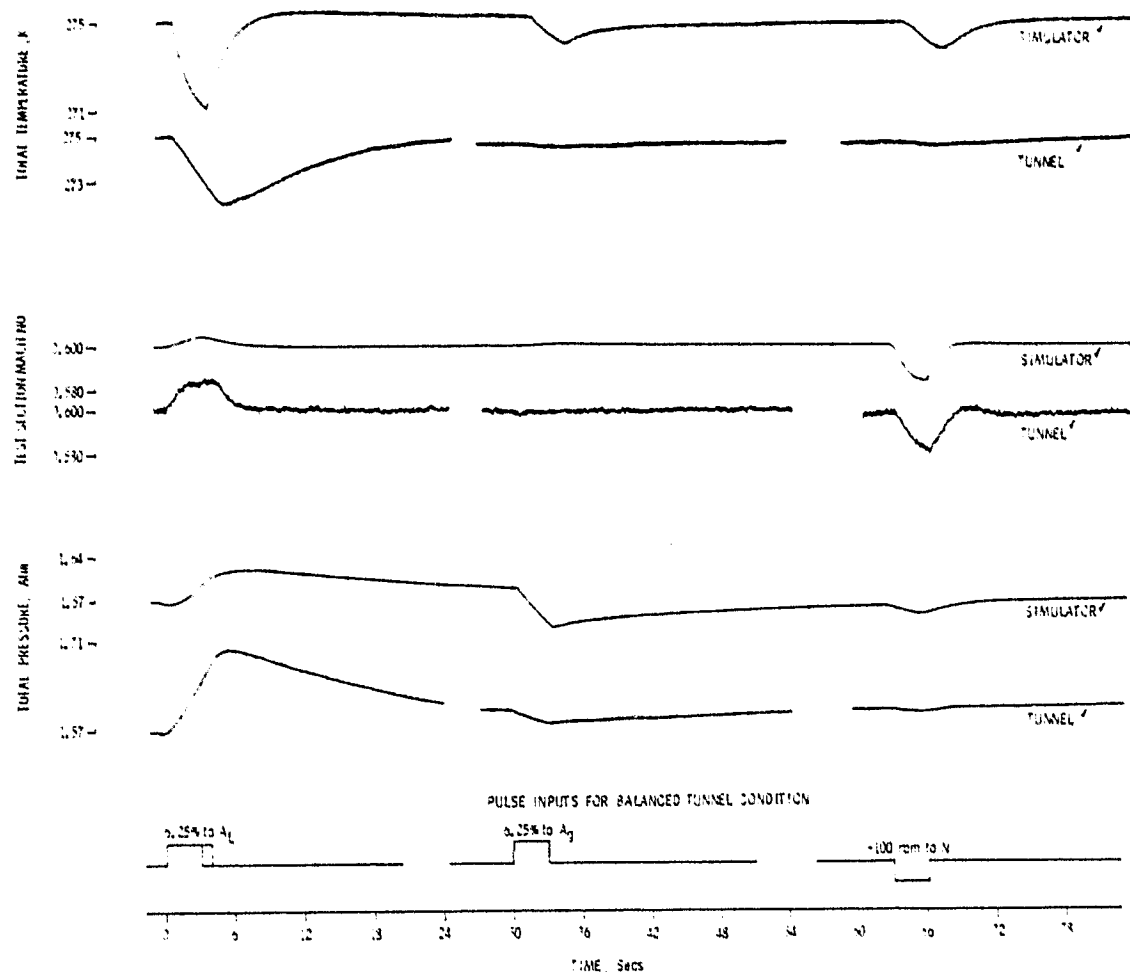


Figure 57. Tunnel and simulator responses; 0.6 M, 1.57 atm, 275 K.

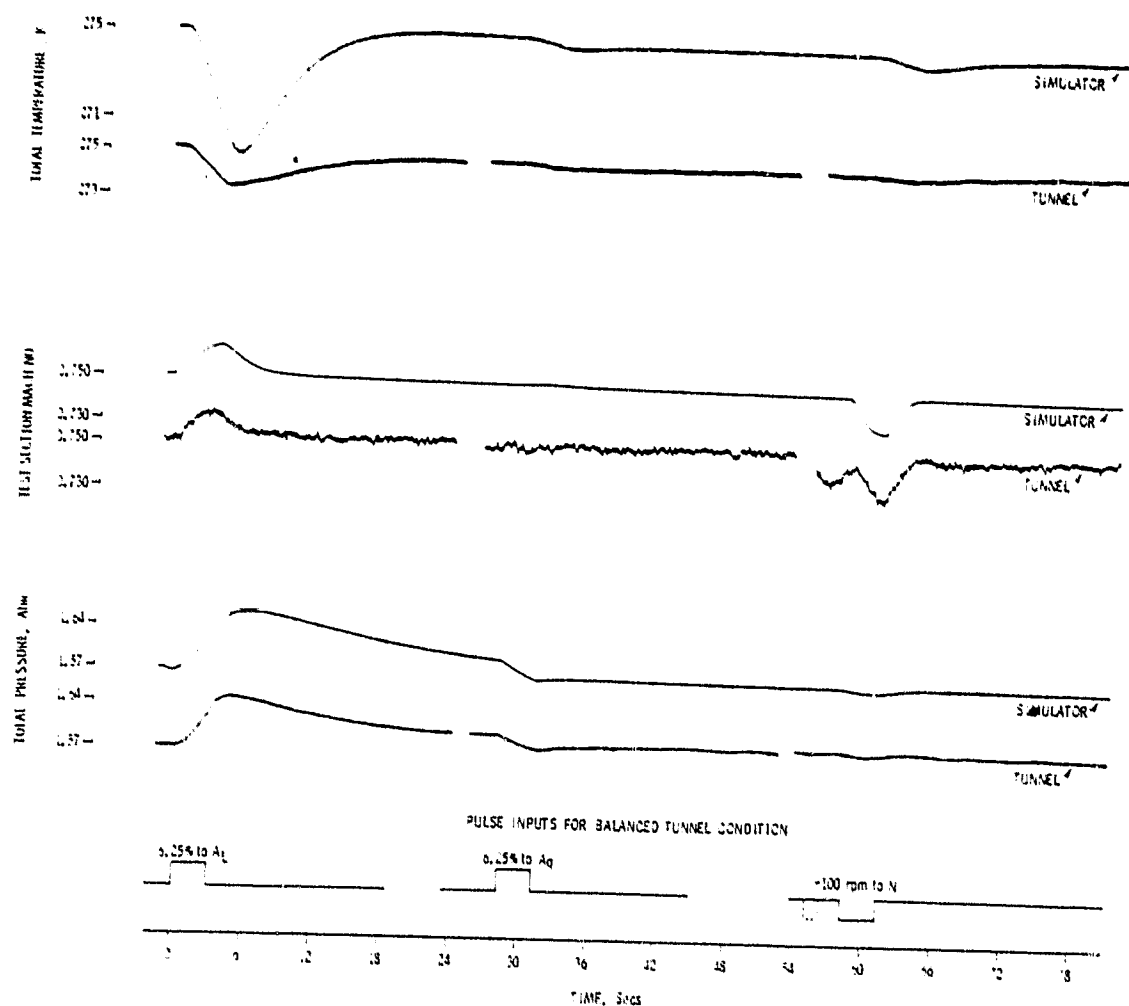


Figure 58. Tunnel and simulator responses; 0.75 M, 1.57 atm, 275 K.

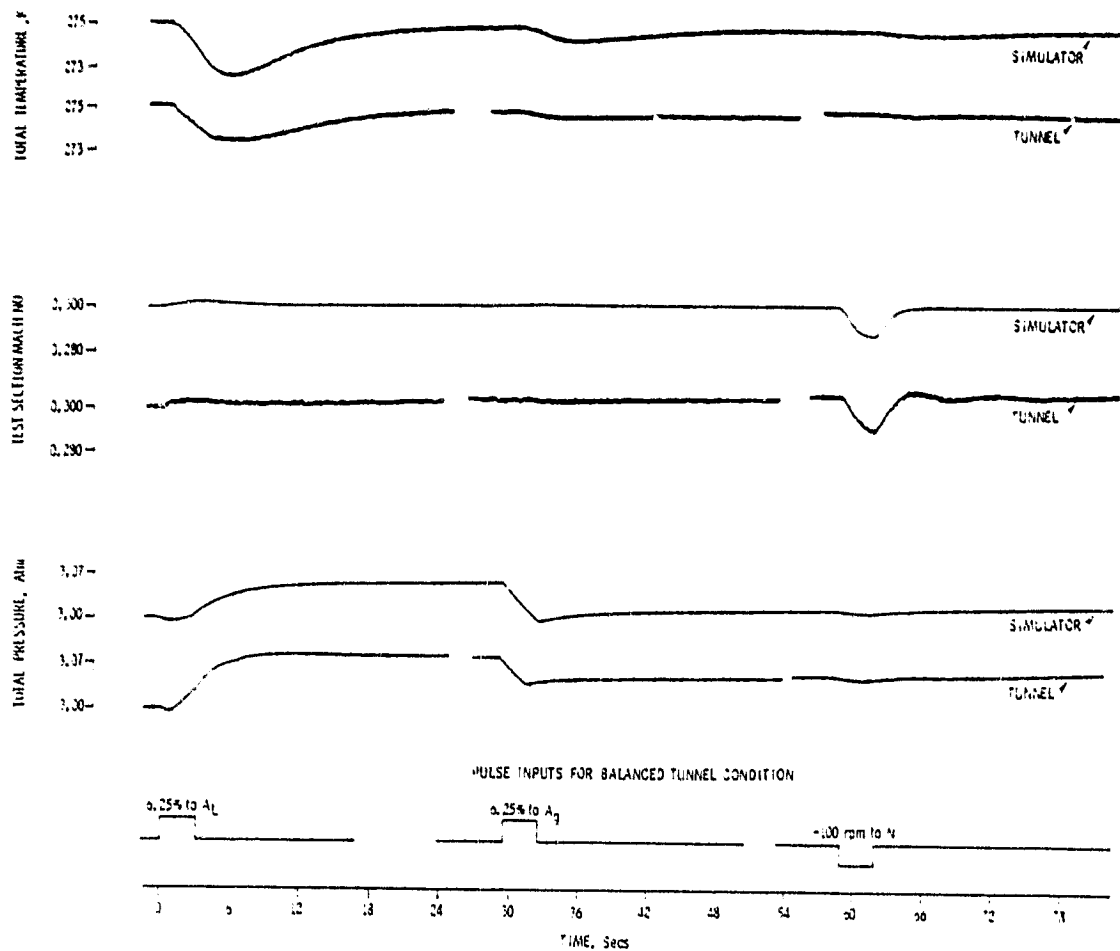


Figure 59. Tunnel and simulator responses; 0.3 M, 3 atm, 275 K.

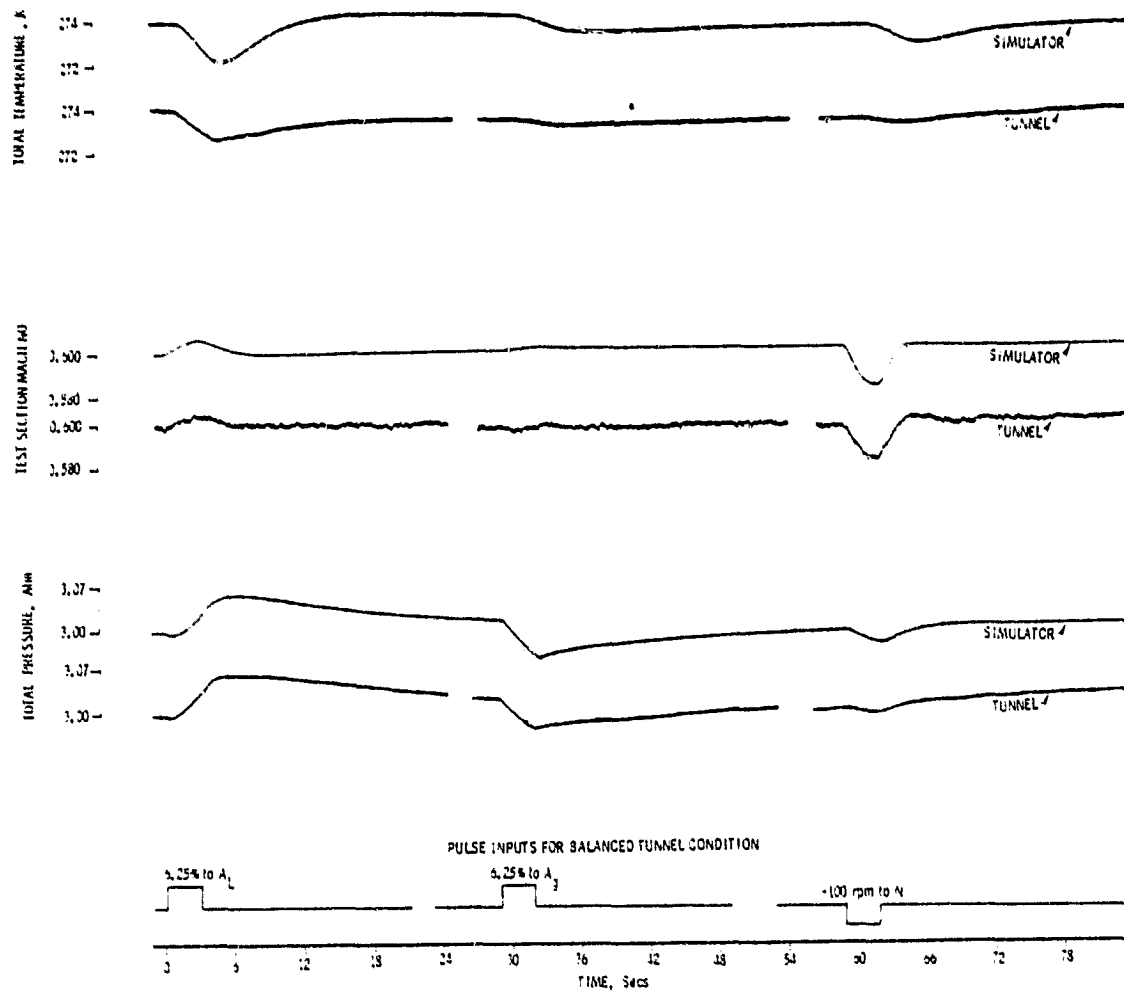


Figure 60. Tunnel and simulator responses; 0.6 M, 3 atm, 274 K.

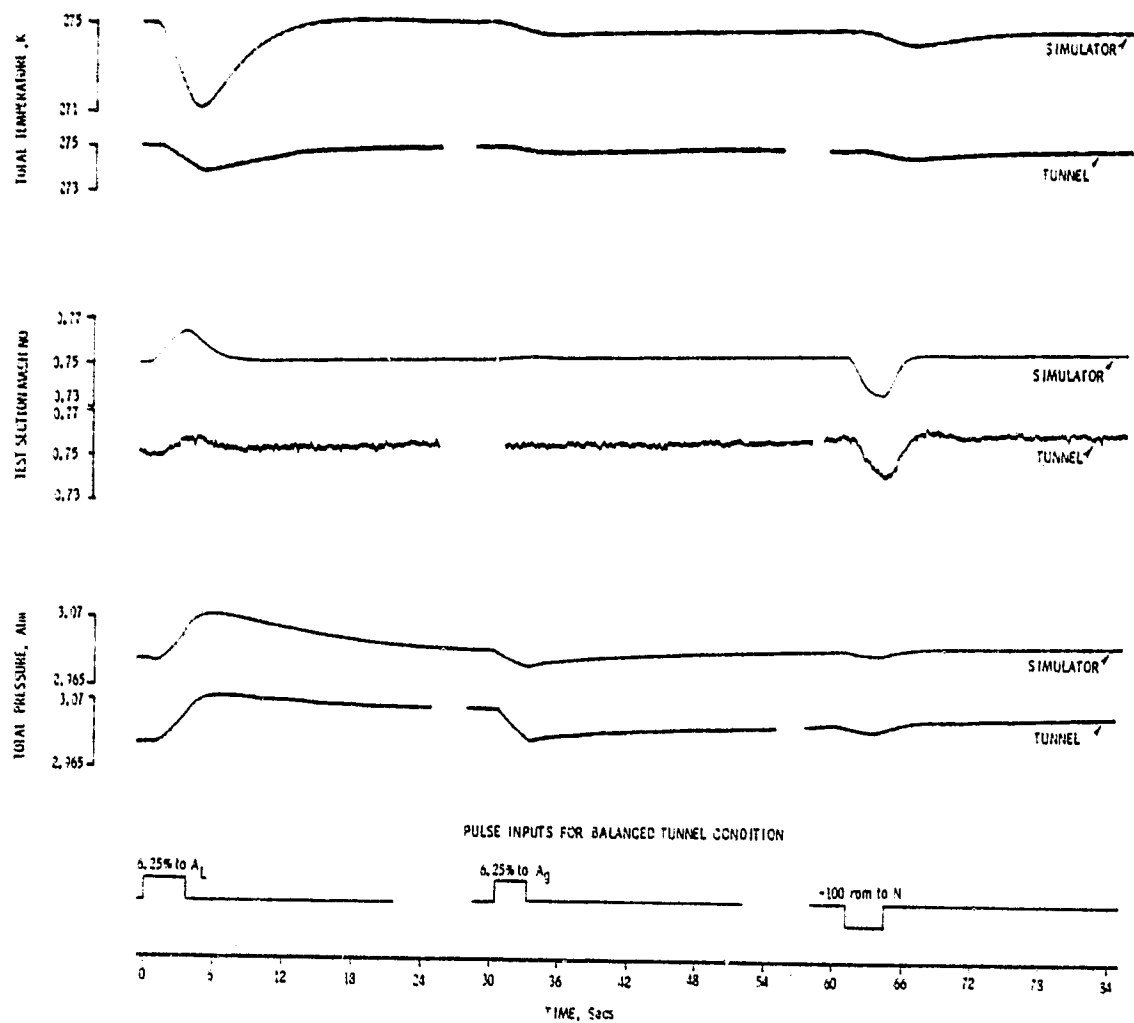


Figure 61. Tunnel and simulator responses; 0.75 M, 3 atm, 275 K.

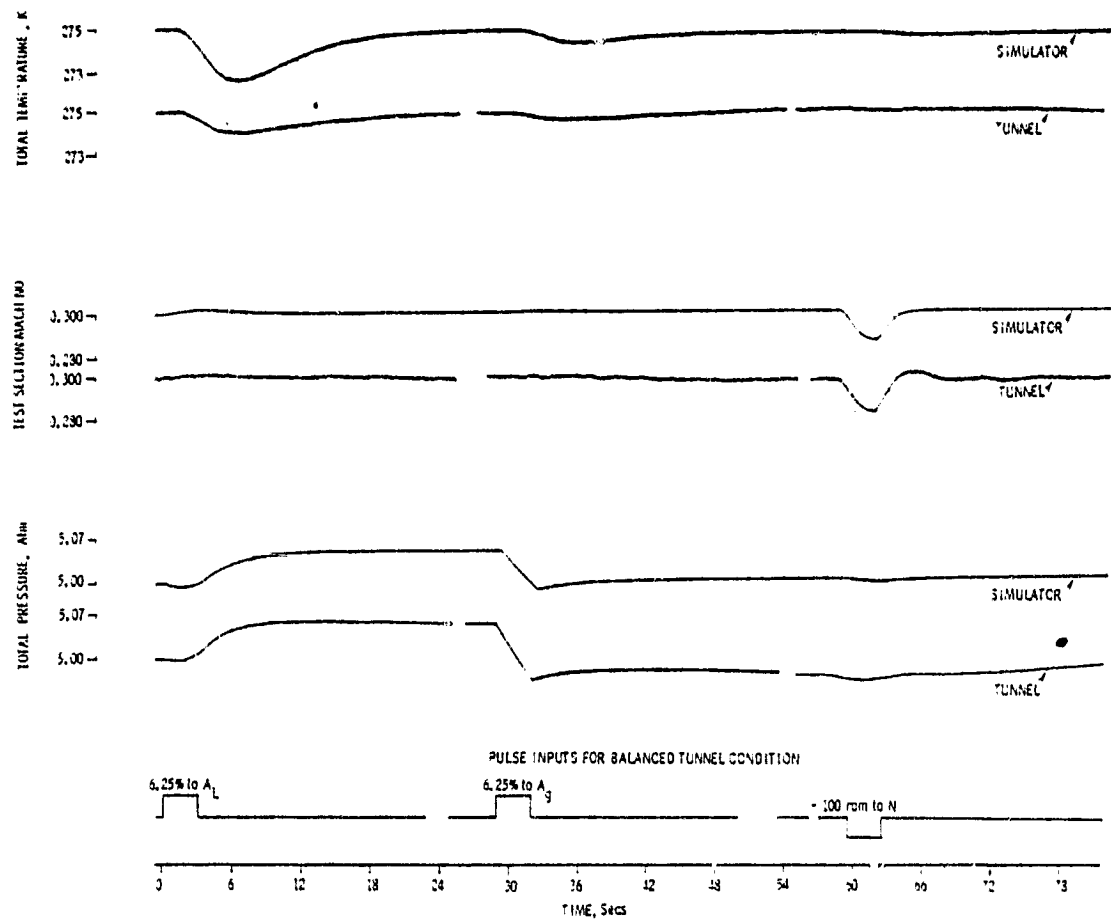


Figure 62. Tunnel and simulator responses; 0.3 M, 5 atm, 275 K.

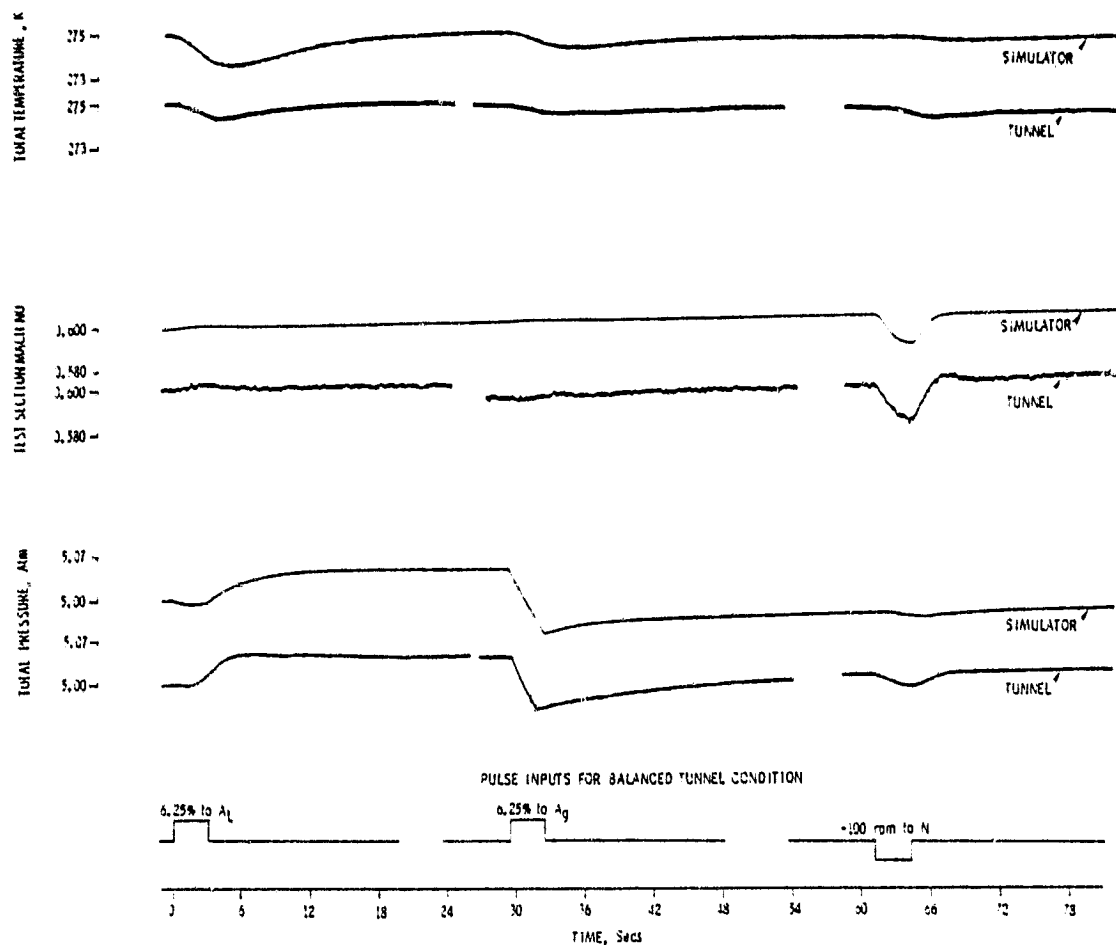


Figure 63. Tunnel and simulator responses; 0.6 M, 5 atm, 275 K.

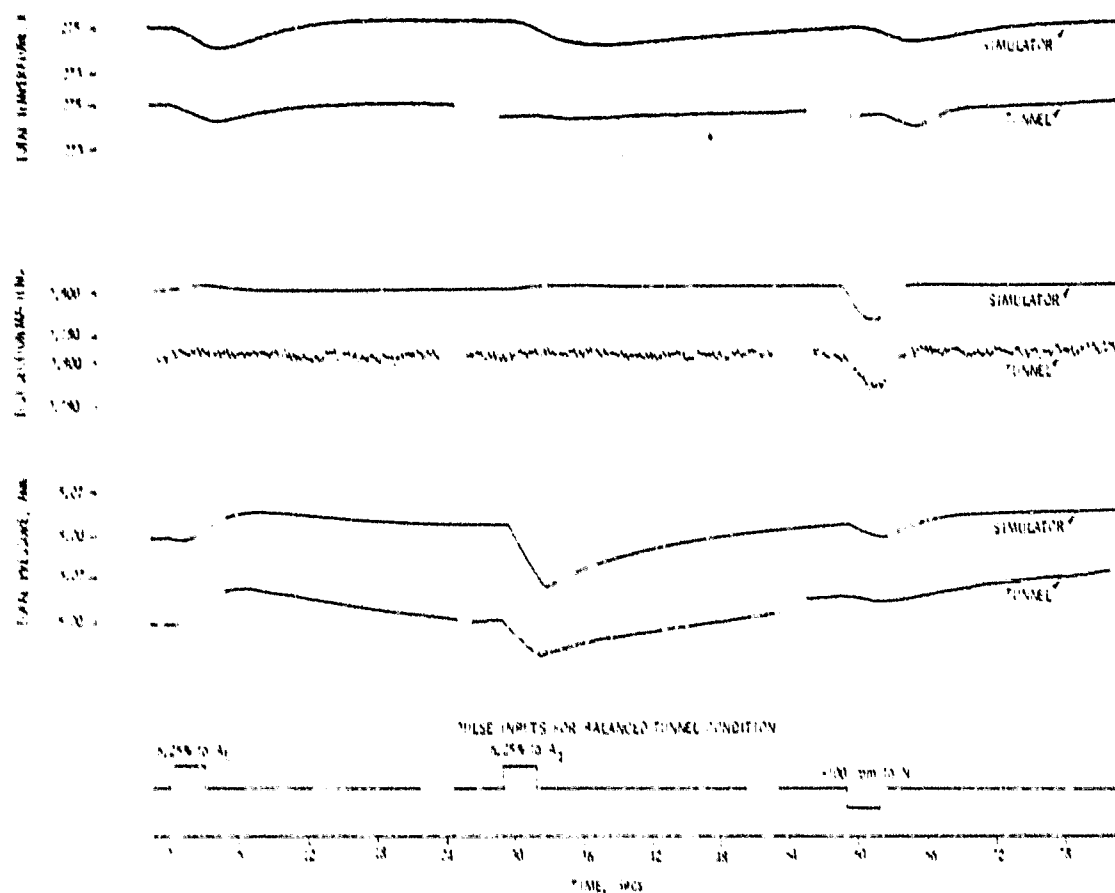


Figure 6-1. Tunnel and simulator responses; 0.8 M, 5 atm, 275 K.

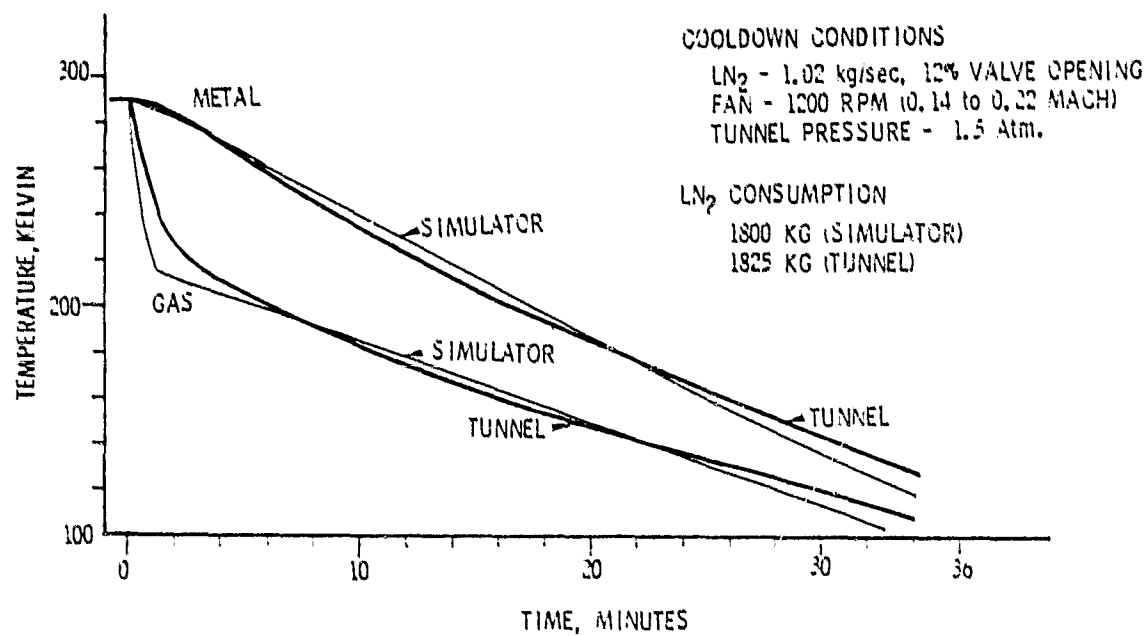


Figure 65. Cool down profile tunnel and simulator.

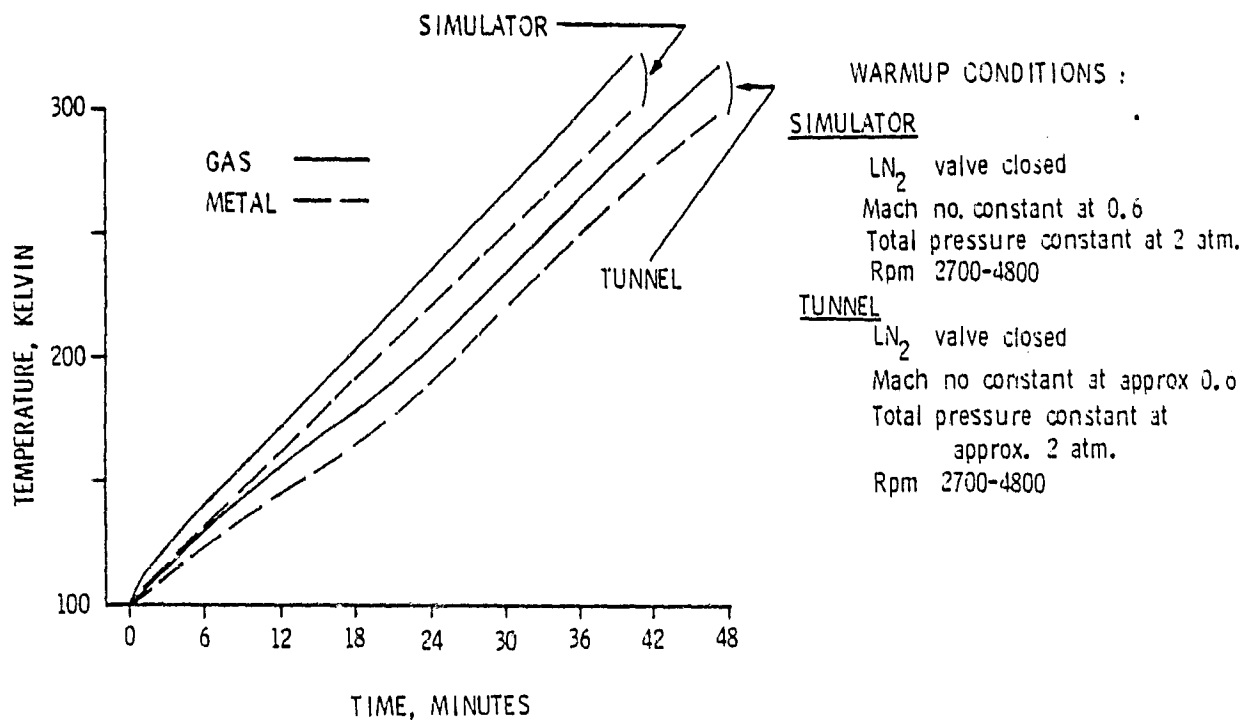


Figure 66. Warmup profile tunnel and simulator.